

Nonlinear optical microspectroscopy with few-cycle laser pulses

Von der Fakultät Mathematik und Physik der Universität Stuttgart
zur Erlangung der Würde eines Doktors der Naturwissenschaften
(Dr. rer. nat.) genehmigte Abhandlung

Vorgelegt von

M.Sc. Hui Wan

aus Nanchang

Hauptberichter: Prof. Dr. Jörg Wrachtrup

Mitberichter: Prof. Dr. Martin Dressel

Tag der mündlichen Prüfung: 14.02.2017

Durchgeführt am 3. Physikalischen Institut der Universität Stuttgart
in der Arbeitsgruppe von Dr. Andreas Volkmer

2017

Contents

1	Einleitung	1
2	Introduction	5
3	Fundamentals	9
3.1	Description of an ultrashort laser pulse	9
3.2	Linear pulse propagation	11
3.3	Second-harmonic generation	12
3.3.1	Description of the SHG signal	14
3.3.1.1	Temporal dependence	14
3.3.1.2	Spatial dependence	15
3.3.2	Simulation of the SHG spectrum	16
3.3.3	The SHG interferometric autocorrelation function	16
3.3.4	SHG polarization dependence for a dipole scatterer	18
3.4	Optical properties of gold nanoparticles	18
3.4.1	Drude-Sommerfeld theory	19
3.4.2	LSPR modes in a gold nanoparticle	19
3.4.2.1	Mie theory	20
3.4.2.2	The quasi-static approximation	21
3.4.3	The driven damped harmonic oscillator model	22
3.4.3.1	Stationary solution	23
3.4.3.2	Non-stationary solution	24
3.4.4	Plasmon dephasing mechanisms	25
3.4.5	Simulation of the plasmon resonance enhanced SHG IAC function	25
3.5	Linear optical properties of a single nanohole in a gold film	26
4	Experimental methods	30
4.1	Optical setup of the few-cycle NLO microscope system	30
4.1.1	Few-cycle laser source	30
4.1.2	Interferometric autocorrelator unit	31

4.1.3	Dispersion management unit	32
4.1.4	Beam management unit	33
4.1.5	Microscope	33
4.1.6	Dark field and transmission microspectroscopy	35
4.2	System control software	36
4.3	Data analysis	38
4.3.1	Analysis of SHG IAC trace measurements	38
4.3.2	Analysis of the excitation pulse spectrum	39
4.3.3	Analysis of SHG, TPF, and DF scattering spectra	40
4.3.4	Polar plot analysis of SHG, TPF, DF scattering, and transmission signals	41
5	Diffraction-limited focusing of few-cycle laser pulses	43
5.1	Materials and methods	43
5.1.1	NLO microscope configurations	43
5.1.2	Preparation of collagen fibril samples	43
5.1.3	AFM imaging of collagen fibrils	45
5.2	NLO characterization of the diffraction-limited focus dimensions	45
5.3	SHG characterization of in-focus pulse properties	47
5.3.1	The measured SHG spectrum in KDP	47
5.3.2	SHG interferometric autocorrelation trace measurements	48
5.3.2.1	In-focus pulse duration dependence on the N.A. of the focusing objective	48
5.3.2.2	In-focus pulse duration dependence on the back-aperture of the focusing objective	51
5.4	Application for enhancement of NLO imaging contrast	53
5.4.1	Dependence of SHG intensity on pulse duration	53
5.4.2	SHG image contrast enhancement and microspectroscopy of single collagen fibrils	54
5.4.2.1	Motivation	54
5.4.2.2	SHG image contrast enhancement	55
5.4.2.3	SHG microspectroscopy of a single collagen fibril	56
5.5	Summary and conclusions	58
6	Time-resolving ultrashort plasmon dephasing in single gold nanoparticles	61
6.1	Motivation	61
6.2	Materials and methods	62
6.2.1	Microscope configurations	62
6.2.2	The gold nanosphere and nanorod samples	62

6.2.3	The gold nanodisk and nanorectangle array samples	63
6.2.4	Extinction measurements	64
6.2.5	Scanning electron microscope imaging	64
6.2.6	Extinction and scattering spectra simulations	64
6.3	Gold nanosphere experiments	64
6.3.1	Size characterization by SEM imaging	64
6.3.2	Ensemble characterization by UV-VIS spectroscopy	65
6.3.3	Single nanosphere characterization by DF spectroscopy	66
6.3.4	Single nanosphere characterization by SHG experiments	67
6.3.4.1	The nonresonant excitation case: 80 nm sphere	68
6.3.4.2	The near-resonant excitation case: 125 nm sphere	70
6.4	Gold nanorod experiments	72
6.4.1	Ensemble characterization by UV-VIS spectroscopy	72
6.4.2	Single nanorod characterization by DF scattering spectroscopy	73
6.4.3	Single nanorod characterization by SHG experiments	74
6.5	Summary of nanosphere and nanorod experiments	80
6.6	Gold nanodisk array experiments	81
6.6.1	Ensemble measurements of extinction spectra	81
6.6.2	Single nanodisk characterization by SHG experiments	83
6.7	Gold nanorectangle array experiments	88
6.7.1	Ensemble measurements of extinction spectra	88
6.7.2	Single nanorectangle characterization by SHG experiments	89
6.8	Summary of nanodisk and nanorectangle results	95
6.9	Summary and Conclusions	96
7	Studying of the ultrafast dynamics of localized surface plasmon resonances in a single nanohole in gold films	98
7.1	Motivation	98
7.2	Materials and methods	99
7.2.1	Microscope configurations	99
7.2.2	Gold nanohole array sample	99
7.2.3	Transmission spectrum simulation	100
7.2.4	Scanning electron microscope imaging	100
7.3	Simulated transmission spectra of single rectangular nanoholes	101
7.4	Single rectangular nanohole characterization by SHG experiments	103
7.4.1	Epi-detected SHG	103
7.4.2	Forward-detected SHG	111

7.5	Summary and Conclusions	116
8	Acknowledgments	117
9	Statement of Authorship	118
10	Bibliography	119
11	List of figures	127
12	List of tables	139
	Appendices	141
A		142
A.1	Estimation of material dispersion for common microscope objectives	142
P	Curriculum vitae	144

1 Einleitung

Die nichtlineare optische (NLO) Mikroskopie stellt ein mächtiges Werkzeug für die Physik, die Chemie und die Materialwissenschaften dar, weil sie intrinsische optische Eigenschaften der Probe markierungsfrei misst [1]. Um die ultraschnellen Prozesse in nichtlinearen Materialien mit einer hohen räumlichen Auflösung untersuchen zu können, müssen sowohl ultrakurze Pulse, als auch Verfahren, um diese mit einer hohen räumlichen Auflösung fokussieren zu können, verbunden werden. Heutzutage sind kommerzielle Festkörperlaser [2] und Faserlaser [3] verfügbar, um Pulse mit einer Dauer von wenigen optischen Zyklen im nahen infraroten Wellenlängenbereich zu generieren. Obwohl die Verbindung aus ultraschnellen Laserpulsen und der Nahfeldmikroskopie [4] hohe räumliche Auflösungen liefern kann, so verhindert die Nahfeld-Wechselwirkung zwischen der Sensorspitze und der Probe die Untersuchung ihrer ungestörten Eigenschaften. Desweiteren erlaubt der Nahfeld-Ansatz keine dreidimensionale Messung. Um diese Einschränkungen zu umgehen, wurden aus wenigen optischen Zyklen bestehende Laserpulse oft mit Hilfe konventioneller Mikroskopobjektive [5] stark fokussiert. Jedoch resultiert die Ausbreitung eines ultrakurzen Pulses in optischen Materialien, insbesondere in dem Glas eines Mikroskopobjektivs mit einer hohen numerischen Apertur (N.A.), in einer räumlichen und zeitlichen Verzerrung des elektrischen Feldes des Laserpuls, was erheblich seine Qualität im Fokus beeinträchtigen kann. In dieser Doktorarbeit werden beugungsbegrenzte, aus wenigen optischen Zyklen bestehende, Pulse realisiert und für die Untersuchung der ungestörten, ultraschnellen Dephasierung von Plasmonen in metallischen Nanopartikeln angewandt. Außerdem profitieren viele biologische Anwendungen der NLO-Mikroskopie von der Verfügbarkeit der aus wenigen Zyklen bestehenden Laserimpulse im Fokus eines Objektivs mit einer hohen N.A. Abgesehen von der Erhöhung des NLO-Bildkontrasts könnte das beugungsbegrenzte Fokussieren der aus wenigen Zyklen bestehenden Pulse den Weg zu fundamentalen Studien der Struktur und Dynamik von biologischen Proben unter physiologischen Bedingungen in drei Dimensionen eröffnen.

Unter Einsatz einer rein passiven Kontrolle der Gruppenverzögerungsdispersion (GDD vom englischen group delay dispersion) und der Dispersion dritter Ordnung (TOD vom englischen third-order dispersion) werden in dieser Doktorarbeit beugungs- und bandbreitenbegren-

zte Pulse bestehend aus wenigen optischen Zyklen im Fokus von Objektiven mit hoher N.A. experimentell demonstriert. Basierend auf diesen Erfolgen wurden die Eigenschaften eines NLO-Mikroskops mit Pulsen weniger optischer Zyklen sowohl für die Bildgebung mittels der Generierung der zweiten harmonischen Ordnung (SHG vom englischen second harmonic generation) als auch für die SHG-Mikrospektroskopie in den Frequenz- und Zeitdomänen charakterisiert. Die umgekehrt proportionale Abhängigkeit der SHG-Intensität von der Pulsdauer im Fokus wurde bis herunter auf 7.1 fs zum Ersten mal demonstriert. Die Anwendung kurzer Pulse im Fokus zur Verbesserung des SHG-Bildkontrasts wurde erfolgreich für eine einzelne Kollagenfibrille (Typ-I) als ein biologisches Modellsystem für die Untersuchung von Proteinansammlungen unter physiologischen Bedingungen demonstriert. Über die Bildgebung hinaus wurde festgestellt, dass sich eine Kollagenfibrille unter den vorliegenden Anregungsbedingungen wie eine rein nicht-resonante, weiche Materie mit einer Suszeptibilität zweiter Ordnung verhält und das Verhältnis ihrer vorwärts- und rückwärtsgemessenen SHG-Intensitäten eine Abschätzung zur Dicke der Fibrille ermöglicht, welche gut mit Messungen mittels der Atomkraft-Mikroskopie (AFM vom englischen atomic force microscopy) übereinstimmt.

Die ultraschnelle Dephasierung der lokalisierten Oberflächen-Plasmonen-Resonanz (LSPR vom englischen localized surface plasmon resonance) in den metallischen Nanopartikeln, die in nur wenigen Femtosekunden geschieht, hat viel Aufmerksamkeit im Bereich der Nanoplasmonik [6] bekommen. Die lineare Streuspektroskopie ist eine Standardmethode, um die spektrale Bandbreite und die Resonanzwellenlänge der LSPR einzelner Nanopartikel und ihre Abhängigkeit von der Größe, der Form, der Komposition und der lokalen Umgebung in der Frequenzdomäne zu untersuchen, woraus die Dephasierungszeit bestimmt werden kann. Die direkte, zeitaufgelöste Bestimmung der Dephasierung der Plasmonen erfolgte mit Hilfe interferometrischer SHG-Spektroskopie an Ensembles von Nanopartikeln [7]. Um die inhomogene Größenverteilung der Nanopartikel zu vermeiden, hat Liao et al. [8] ein erstes Machbarkeitsexperiment an einzelnen Nanopartikeln mit Anregungspulsen von 23 fs beschrieben. Eine systematische SHG-Studie in der Zeitdomäne an einzelnen Metallnanopartikeln verschiedener Größen und Formen wurde jedoch bisher noch nicht veröffentlicht. Bei dieser Doktorarbeit handelt es sich um die erste systematische, experimentelle, zeitaufgelöste Demonstration ultrakurzer Dephasierungsprozesse von Plasmonen in einzelnen Goldnanopartikeln unter Einsatz unserer 7.3 fs Anregungspulse im Fokus in Kombination mit der linearen Streuspektroskopie, durchgeführt an denselben Nanopartikeln. Für Nanostäbchen, Nanoscheiben und Nanorechtecke werden intensive, durch die Plasmonenresonanz verstärkte SHG beobachtet, wobei die SHG-Intensität stark von der spektralen Überlappung zwischen der LSPR-Bande und dem Laseranregungsspektrum abhängt. Bei einzelnen Nanostäbchen und Nanorechtecken wurde festgestellt, dass die Abhängigkeit der Intensität der durch die Plasmonenresonanz verstärkten SHG vom Einfallswinkel der linear polarisierten Anregung einer Dipolstreuung zweiter Ordnung folgt, und die

Einflüsse der Größe und Form auf die Eigenschaften der LSPR wurden direkt in der Zeitdomäne beobachtet. Eine gute Übereinstimmung zwischen experimentell ermittelten und simulierten Werten für Dephasierungszeiten und Resonanzwellenlängen wurde erzielt, was bestätigt, dass das gebräuchliche Modell des getriebenen, gedämpften, harmonischen Oszillators für die LSPR der Nanopartikel sowohl die linearen Streuspektren in der Frequenzdomäne als auch die SHG-Antwort in der Zeitdomäne qualitativ erklären kann.

Resonanzbanden in linearen Transmissions- und Streuspektren wurden auch für Nanolöcher in einem Metallfilm beobachtet, deren Größen kleiner als die Wellenlänge des einfallenden Lichts sind. Diese wurden LSPR-Moden der elektrischen Feldverteilung um die Nanolöcher zugeordnet, die qualitativ vergleichbare Resonanzeigenschaften zu den Nanopartikeln aufweisen. Auch wurden die polarisationsaufgelösten nichtlinearen optischen Eigenschaften der einzelnen Nanolöcher verschiedener Formen und Symmetrien unter Einsatz der SHG- [9] [10] und der Multiphotonenemissionsmikroskopie [11] beschrieben. Systematische SHG-Studien über die Auswirkung der Größe auf die LSPR der einzelnen Nanolöcher in Metallfilmen und ihrer ultraschnellen Dephasierungsdynamiken wurden jedoch noch nicht publiziert. In dieser Doktorarbeit wird die Verstärkung sowohl der vorwärts- als auch der rückwärtsgestreuten SHG-Emissionen einzelner rechteckiger Nanolöcher beobachtet, jedoch konnte keine ultraschnelle Dephasierungsdynamik der LSPR in rechteckigen Nanolöchern mit unseren 7.3 fs Anregungslaserpulsen im Fokus zeitaufgelöst werden. Dies weist darauf hin dass der Beitrag der von der LSPR verstärkten SHG zu den gemessenen SHG-Signalen vernachlässigbar ist. Weitere Forschung muss betrieben werden, um die momentanen experimentellen Beschränkungen zu überwinden. Dem Babinetischen Prinzip zufolge [12] entspricht die spektrale Antwort eines einzelnen rechteckigen Nanolochs für ein gegebenes linear polarisiertes Anregungsfeld der ihres Komplements für eine orthogonale Polarisation. Während die Anwendbarkeit des Babinetischen Prinzips bereits experimentell für lineare optische Frequenzen von Metamaterialien und Nanoantennen [13] [14] demonstriert wurde, so bleibt die Frage offen, ob das Babinetische Prinzip auch in nichtlinearen optischen Streuexperimenten angewendet werden kann. In dieser Doktorarbeit wird gezeigt, dass die Abhängigkeit der vorwärts- und rückwärtsgestreuten SHG-Intensitäten von einzelnen rechteckigen Nanolöchern vom Winkel zwischen dem einfallenden linear polarisierten Anregungsfeld und der langen Achse der rechteckigen Nanolöcher einer Dipolstreuung zweiter Ordnung folgt. Es wurde beobachtet, dass während die SHG-Dipolstreuung an rechteckigen Nanopartikeln parallel zu deren langer Achse orientiert ist, so ist die SHG-Dipolstreuung an einem komplementären rechteckigen Nanoloch senkrecht zu dessen langer Achse orientiert. Diese Beobachtung verkörpert die erste experimentelle Demonstration des Babinetischen Prinzips in der nichtlinearer Streuung zweiter Ordnung eines einzelnen rechteckigen Nanolochs in einem Goldfilm.

Diese Doktorarbeit ist folgendermaßen gegliedert: In Kapitel 3 werden die fundamentalen

Prinzipien vorgestellt, die zur Erklärung der experimentellen Daten und der Modelle notwendig sind, und die für die Simulationen benutzt werden. Dieses Kapitel enthält die Beschreibung der ultrakurzen, optischen Pulse sowie ihrer linearen und nichtlinearen Wechselwirkungen mit Materie, insbesondere die SHG. Die interferometrische SHG-Autokorrelationsfunktion (SHG IAC vom englischen SHG interferometric autocorrelation), welche zur Pulscharakterisierung und Zeitauflösung der ultraschnellen Plasmonendephasingprozesse benutzt wird, wird ausführlich besprochen. Im Folgenden werden die linearen und nichtlinearen optischen Eigenschaften der Goldnanopartikel und Nanolöcher vorgestellt, wobei der Schwerpunkt auf die entsprechenden LSPR-Moden gesetzt wird, welche unter Einsatz der Mie-Theorie, des Modells des getriebenen, gedämpften, harmonischen Oszillators und des Babinet'schen Prinzips beschrieben werden. In Kapitel 4 wird der optische Aufbau des NLO-Mikroskopsystems mit Laserpulsen weniger optischer Zyklen und die Systemsteuerungssoftware beschrieben. Die Datenauswertungsmethoden, welche üblich für alle Experimente sind, werden hier auch zusammengefasst. In Kapitel 5 werden die räumlichen Eigenschaften der fokussierten Pulse in den Frequenz- und Zeitdomänen experimentell charakterisiert. Insbesondere wird die Verstärkung des nichtlinearen optischen Bildkontrasts und die Mikrospektroskopie in den Frequenz- und Zeitdomänen unter Einsatz der im Fokus aus wenigen Zyklen bestehenden Pulse für die SHG einzelner Kollagenfibrillen demonstriert. In Kapitel 6 wird die experimentelle Studie der LSPR-Eigenschaften der einzelnen Nanosphären, Nanostäbchen, Nanoscheiben und Nanorechtecke variierender Größe und Form unter Einsatz der linearen und der SHG-Spektroskopie in den Frequenz- und Zeitdomänen in Kombination mit polarisationsaufgelösten Experimenten präsentiert. In Kapitel 7 wird die experimentelle Untersuchung der LSPR-Eigenschaften einzelner rechteckiger Nanolöcher variierender Größe in Goldfilmen, die Simulation ihrer Transmissionsspektren, die Spektroskopie der SHG-Strahlung in den Frequenz- und Zeitdomänen, und die Bildgebung in Kombination mit polarisationsauflösenden Messungen der SHG-Strahlung in sowohl der Vorwärts- als auch der Rückwärtsdetektionsgeometrie vorgestellt. Jedes der Ergebniskapitel 5, 6 und 7 endet mit einer detaillierten Zusammenfassung und einer Schlussfolgerung.

2 Introduction

Nonlinear optical (NLO) microscopy is a powerful tool in physics, chemistry, and material science, since it probes intrinsic optical properties of the sample without the need of labeling [1]. In order to investigate the ultrafast processes in nonlinear materials with high spatial resolution, we need to combine both ultrashort pulses and techniques focusing them to the diffraction limit. Nowadays, the commercial solid state laser [2] and fiber laser [3] are available to generate the few-cycle pulses in the near-infrared wavelength range. Even though the combination of ultrafast laser pulses and near-field microscopy [4] can provide high spatial resolution, the near-field interaction between probe tip and the sample avoids studying unperturbed properties of the sample. Also there is no three-dimensional sectioning capability for the near-field approach. In order to overcome these limitations, few-cycle laser pulses have often been tightly focused using conventional microscope objectives [5]. However, the propagation of an ultrashort pulse in optical materials, particularly in the glass of a high N.A. microscope objective, results in spatial and temporal distortions of the pulse electric field, which can severely affect its quality in the focus. In this thesis, diffraction-limited few-cycle pulses are demonstrated and applied for the unperturbed study of ultrafast plasmon dephasing processes of metallic nanoparticles. Also, many biological applications of NLO microscopy benefit from the availability of few-cycle laser pulses at the focus of a high N.A. objective. Apart from enhancing the NLO image contrast, diffraction-limited focusing of few-cycle pulses might pave the way for fundamental studies of structure and dynamics of biological samples under physiological conditions with three-dimensional sectioning capability.

By purely passive group delay dispersion (GDD) and third-order dispersion (TOD) management in this thesis, we experimentally demonstrate in-focus diffraction-limited and bandwidth-limited few-cycle pulses by using high N.A. objectives. Based on these achievements, the performance of a novel few-cycle NLO microscope for both second-harmonic generation (SHG) imaging and microspectroscopy in the frequency- and time-domains was characterized. The inverse linear dependence of SHG intensity on the in-focus pulse duration was demonstrated down to 7.1 fs for the first time. The application of shorter in-focus pulses for the enhancement of SHG image contrast was successfully demonstrated on a single collagen (type-I) fibril as a

biological model system for studying protein assemblies under physiological conditions. Beyond imaging, a collagen fibril has been found to act as a purely non-resonant $\chi^{(2)}$ soft matter under the present excitation conditions, and its ratio of forward- to epi-detected SHG intensities allowed for the estimation of the fibril thickness, which corresponds well with atomic force microscopy (AFM) measurements.

The ultrafast dephasing of the localized surface plasmon resonance (LSPR) in the metallic nanoparticles, that only occurs on a time scale of a few femtoseconds, has gained a lot of attraction in the field of nanoplasmonics [6]. The linear scattering spectroscopy is a standard method to investigate the spectral bandwidth and the resonance wavelength of the LSPR in individual nanoparticles and its dependence on the nanoparticle's size, shape, composition, and local environment in the frequency-domain, from which dephasing times are retrieved. Directly time-resolving the plasmon dephasing was determined by using interferometric SHG spectroscopy of an ensemble of nanoparticles [7]. To avoid inhomogeneous size distributions of nanoparticles, Liao et al. [8] reported a proof of principle experiment on single nanoparticles with excitation pulses of 23 fs. However, a systematic time-domain SHG study of single metal nanoparticles of different sizes and shapes has not been reported yet. This thesis is the first systematic experimental demonstration of time-resolving ultrashort plasmon dephasing in single gold nanoparticles by using the time-domain and our in-focus 7.3 fs excitation pulses in combination with linear scattering spectroscopy performed on the same nanoparticle. For nanorods, nanodisks, and nanorectangles, strong plasmon resonance enhanced SHG is observed, where the SHG intensity strongly depends on the spectral overlap between the LSPR band and the excitation laser spectrum. For single nanorods and nanorectangles, the dependence of the plasmon resonance enhanced SHG intensity on the incident angle of the linearly polarized excitation was found to follow second-order dipole scattering, and the effect of size and shape on the LSPR properties was directly observed in the time-domain. Good agreement between experimental and simulated values of dephasing times and resonance wavelengths is obtained, which confirms that a common driven damped harmonic oscillator model for the LSPR in the nanoparticle can qualitatively explain both the linear scattering spectra in the frequency-domain and the SHG response in the time-domain.

Resonance bands in linear transmission and scattering spectra have also been observed for nanoholes with sizes smaller than the wavelength of the incident light in a metal film, which are assigned to LSPR modes of the electric field distribution around the nanohole with qualitatively similar resonance properties as a nanoparticle. The polarization-resolved nonlinear optical properties of the single nanoholes with different shapes and symmetries were also reported by using SHG [9] [10] and multi-photon emission [11] microscopies. However, systematic SHG studies of the size effect in the LSPR of the single nanoholes in the metal films and of their ultrafast dephasing dynamics have not been reported yet. In this thesis, enhancement of both

the forward- and epi-detected SHG emissions from single rectangular nanoholes are observed, however, no ultrafast dephasing dynamics of LSPRs in rectangular nanoholes could be time-resolved with our in-focus 7.3 fs excitation laser pulses, which indicates that contributions from LSPR enhanced SHG to the detected SHG signal are negligible. More work needs to be done in order to overcome the current experimental limitations. According to Babinet's principle [12], the spectral response of single rectangular nanoholes for a given linearly polarized excitation field corresponds to that of its complement for orthogonal polarization. While the applicability of Babinet's principle has been previously experimentally demonstrated for linear optical frequency metamaterials and nanoantennas [13] [14], the question as to whether Babinet's principle can even be applied in nonlinear optical scattering measurements remains to be answered. In this thesis, the dependence of the forward- and epi-detected SHG intensity from the single rectangular nanohole on the angle between the incident linearly polarized excitation field and the long-axis of the rectangular nanohole was found to follow that of a second-order dipole pattern. While the SHG dipole pattern observed for rectangular nanoparticles is oriented parallel to its long-axis, the SHG dipole pattern of its complementary rectangular nanohole is oriented perpendicular to its long-axis. This observation represents the first experimental demonstration of Babinet's principle in second-order nonlinear scattering of a single rectangular nanohole in a gold film.

This thesis is organized as follows: In chapter 3, the fundamental principles needed to explain the experimental data and the models used for simulations are presented. This includes the description of ultrafast optical pulses and their linear and nonlinear interactions with matter, in particular SHG. The SHG interferometric autocorrelation (SHG IAC) function, which is used for pulse characterization and time-resolving of ultrafast plasmon dephasing processes throughout this thesis is then discussed in detail. Next, the linear and nonlinear optical properties of gold nanoparticles and nanoholes are introduced, where the emphasis is put on the corresponding LSPR modes, which are described by the Mie theory, the driven damped harmonic oscillator model, and Babinet's principle. In chapter 4, the optical setup of the few-cycle NLO microscope system and the system control software are described. The data analysis methods, which are common to all the experiments are also summarized here. In chapter 5, we experimentally characterize the spatial properties of the focus and the properties of the in-focus pulses in both frequency- and time- domains. In particular, the nonlinear optical image contrast enhancement and microspectroscopy in both the frequency- and time-domains by using in-focus few-cycle pulses are demonstrated for the SHG of single collagen fibrils. In chapter 6, we present the experimental study of LSPR properties of individual nanospheres, nanorods, nanodisks, and nanorectangles of varying sizes and shapes using linear and SHG spectroscopies in the frequency- and time-domains in combination with polarization-resolved experiments. In chapter 7, we present the experimental study of LSPR properties of individual

rectangular nanoholes of varying sizes in gold films using simulated linear transmission spectra, SHG spectroscopies in both the frequency- and time-domains, and SHG imaging in combination with SHG polarization-resolved experiments in both the forward- and epi-detection geometries. Each result chapter 5, 6 and 7 ends with a detailed summary and conclusion section.

3 Fundamentals

In this chapter, the fundamental principles needed to explain the experimental data and the models used for simulations are presented. This includes the description of ultrafast optical pulses and their linear and nonlinear interactions with matter. In particular, the descriptions of second-harmonic generation (SHG) signals in the frequency- and time- domains are discussed. The SHG interferometric autocorrelation (SHG IAC) function, which is used for pulse characterization and time-resolving of ultrafast plasmon dephasing processes throughout this thesis, is then discussed in detail. Next, the linear and nonlinear optical properties of gold nanoparticles and nanoholes in gold films are introduced, where the emphasis is put on the corresponding localized surface plasmon resonance (LSPR) modes, which are described by the Mie theory, the driven damped harmonic oscillator model, and Babinet's principle.

3.1 Description of an ultrashort laser pulse

A laser pulse is described by the electric field, $\mathbf{E}(\mathbf{r}, t)$, which is a function of both space \mathbf{r} and time t . The real-valued scalar quantity describing the time-dependent electric field $E(t)$ of an ultrashort optical pulse at a fixed point in space can be written as

$$E(t) = A(t)e^{i\phi(t)} + c.c. , \quad (3.1)$$

where $A(t)$ and $\phi(t)$ are the time-dependent amplitude and phase functions, respectively. $c.c.$ is the complex conjugate term. The optical pulse duration τ_p is usually defined by the FWHM (full width at half-maximum) of the temporal intensity function $I(t)$, which can be written as

$$I(t) = 2\varepsilon_0 n c |A(t)|^2, \quad (3.2)$$

with the dielectric constant of the vacuum ε_0 , the speed of light c , and the refractive index n . The temporal and spectral characteristics of a laser pulse field are related to each other by the Fourier transformations:

$$E(t) = \frac{1}{2\pi} \int_{-\infty}^{\infty} \tilde{E}(\omega) e^{i\omega t} d\omega = \mathcal{F}[\tilde{E}(\omega)] \quad (3.3)$$

and

$$\tilde{E}(\omega) = \int_{-\infty}^{\infty} E(t)e^{-i\omega t} dt = \mathcal{F}^{-1}[E(t)]. \quad (3.4)$$

\mathcal{F} and \mathcal{F}^{-1} are the operators for the forward and inverse Fourier transforms, respectively. The complex frequency-dependent electric field $\tilde{E}(\omega)$ can then be written as

$$\tilde{E}(\omega) = A(\omega)e^{-i\varphi(\omega)} + c.c., \quad (3.5)$$

where $A(\omega)$ and $\varphi(\omega)$ are spectral field amplitude and phase functions, respectively. The spectral intensity $I(\omega)$ is then given by

$$I(\omega) = \frac{\varepsilon_0 n c |A(\omega)|^2}{\pi}. \quad (3.6)$$

The spectral bandwidth ω_p of optical pulses is defined as the FWHM of the spectral intensity $I(\omega)$. As a consequence of the uncertainty principle, the pulse duration and the bandwidth cannot independently vary to each other. The time-bandwidth product (TBP) can be written as

$$TBP = \tau_p \omega_p / 2\pi \geq c_B, \quad (3.7)$$

where c_B is a minimum constant value determined by the pulse shape. If the pulse has a flat spectral phase, it is called ‘Fourier-limited’. When the equality holds, the pulse exhibits the shortest duration at a given spectral width and pulse shape. If the pulse is not Fourier-limited ($TBP > c_B$), the pulse duration is increased.

A typical analytical description of the pulse shape is given by the hyperbolic secant (sech) function, where the electric field amplitudes for Fourier-limited pulses in the time- and frequency- domains are written as [15]

$$A(t) = \frac{A_0}{2} \operatorname{sech}\left(2 \ln(1 + \sqrt{2}) \frac{t}{\tau_p}\right) \quad (3.8)$$

and

$$A(\omega) = A_0 \tau_p \frac{\pi}{4 \ln(1 + \sqrt{2})} \operatorname{sech}\left(\frac{\pi \tau_p}{4 \ln(1 + \sqrt{2})} \omega\right), \quad (3.9)$$

respectively. A_0 is constant value. For a sech^2 laser pulse, $c_B = 0.315$ [16] in eq. 3.7. Because the spectral amplitude $A(\omega)$ is distributed around a carrier frequency ω_0 of the optical pulse, one can expand the spectral phase $\varphi(\omega)$ into a Taylor series

$$\varphi(\omega) = \varphi(\omega_0) + \left. \frac{\partial \varphi}{\partial \omega} \right|_{\omega_0} (\omega - \omega_0) + \frac{1}{2} \left. \frac{\partial^2 \varphi}{\partial \omega^2} \right|_{\omega_0} (\omega - \omega_0)^2 + \frac{1}{6} \left. \frac{\partial^3 \varphi}{\partial \omega^3} \right|_{\omega_0} (\omega - \omega_0)^3 + \dots, \quad (3.10)$$

where only the first four terms are considered. The first term $\varphi(\omega_0)$ is known as the carrier envelope phase, which corresponds to an absolute phase offset. The second term $\left. \frac{\partial \varphi}{\partial \omega} \right|_{\omega_0}$ leads to a constant group delay, which is a temporal translation of the pulse phase envelope, without an

effect on the pulse shape. The third and fourth terms in eq. 3.10 are dominated by group delay dispersion (GDD) and third-order dispersion (TOD), which are defined as

$$GDD = \left. \frac{\partial^2 \varphi}{\partial \omega^2} \right|_{\omega_0} \quad (3.11)$$

and

$$TOD = \left. \frac{\partial^3 \varphi}{\partial \omega^3} \right|_{\omega_0}, \quad (3.12)$$

respectively. In contrast to carrier envelope phase and group delay phase, the presence of both GDD and TOD changes the temporal pulse shape and increases the pulse duration. GDD and TOD distort a pulse in different manners: When $GDD > 0$ ($GDD < 0$), by convention, the pulse is linearly up- (down-) chirped, which exhibits a linear increase (decrease) of the frequency in time. For $TOD \neq 0$, the central frequency of the pulse arrives first, the frequencies on either side arrive later, which is called quadratic chirp.

3.2 Linear pulse propagation

Few-cycle laser pulses will undergo complicated phase changes when propagating through an optical system, such as, for example, lenses, air, and mirrors. By assuming that the pulse peak intensities are kept low, such that nonlinear interaction with the elements of the optical system are negligible, the linear propagation of the pulse electric field is best described in the frequency domain. The output of the electric field $E_{out}(\omega)$ after the passage of the incident field $E_{in}(\omega)$ through a linear optical element can be mathematically described as

$$E_{out}(\omega) = H(\omega)E_{in}(\omega), \quad (3.13)$$

where $H(\omega)$ is the complex optical transfer function of the optical elements:

$$H(\omega) = R(\omega)e^{-i\varphi_d(\omega)}. \quad (3.14)$$

$R(\omega)$ is the real-valued spectral amplitude response function, and $\varphi_d(\omega)$ is the spectral phase transfer function, which describes the spectral phase accumulated upon the passage through the optical elements.

Recalling eqs. 3.5, 3.13 and 3.14, the description of an output electric field $E_{out}(\omega)$ after propagation through an optical element is then written as

$$E_{out}(\omega) = A_{in}(\omega)R(\omega)e^{-i[\varphi(\omega)+\varphi_d(\omega)]}, \quad (3.15)$$

which clearly illustrates that the additional phase $\varphi_d(\omega)$ has an affect on the ultrashort pulse.

In the following discussions, we focus on the spectral phase transfer function for both the dispersion due to the propagation of an optical pulse through a transparent medium and the

dispersion due to interferences in the so-called dispersive mirrors, which are related to our experiments.

The spectral phase transfer function due to propagation of the pulse through a medium of refractive index $n(\omega)$ and a propagation length L is given by

$$\varphi_d(\omega) = \frac{n(\omega)\omega L}{c}. \quad (3.16)$$

According to eqs. 3.10, 3.11, and 3.12, the GDD and TOD values due to material dispersion at ω_0 can be calculated [15]. To give an example, the normal dispersion of common materials in the visible and near-infrared wavelength ranges results in linearly-up chirped pulses ($GDD_{medium} > 0$ and $TOD_{medium} > 0$). Typical GDD_{medium} and TOD_{medium} values at 800 nm for air [17], water [18], BK7 glass [15], and fused silica glass [15] are listed in table A.2 (see appendix A.1).

In order to achieve the pulses with smallest TBP, it is indispensable for an optical system to introduce negative dispersion for compensation of positive dispersion introduced by the propagation through a normal dispersion medium. Several optical elements have been used that exploit a spectral phase transfer function with a negative angular dispersion, such as gratings [19] and prisms pairs [20]. In this work, we introduce negative dispersion provided by interferences in multilayer-coated dispersive mirrors, which enable an extremely compact and broadband dispersion control of femtosecond pulses [21]. Fig. 3.1 shows a conceptual drawing of the origin of negative dispersion in a dispersive mirror, which consists of dielectric multilayer coatings of alternating transparent pairs of high- and low- index layers with a thickness equal to the quarter of the Bragg reflection wavelength. The period is increasing with increasing distance from the mirror surface. If the optical thickness of the layers along the mirror structure is changed, and the different spectral components of the optical pulse penetrated to different depth before being reflected, constructive interference for the longer wavelength occurs at deeper multilayers. By careful design of these layer stacks, not only negative GDD but also even negative TOD can be achieved over almost the entire pulse bandwidth. Pairs consisting of two matched dispersive mirrors are usually implemented, which are specially designed to cancel out spectral oscillations in the GDD spectrum of a single chirp mirror, achieving a considerable flattening of the GDD spectrum over an entire bandwidth of a few-cycle laser pulse. Typical values for GDD and TOD at 800 nm for a single reflection on custom-tailored dispersive mirrors and beam-splitters [22] used in this thesis are also listed in table A.2 (see appendix A.1).

3.3 Second-harmonic generation

In the presence of intense electric field amplitudes, which can modify the optical properties of an optical medium, nonlinear optics is needed for more accurate description of interaction

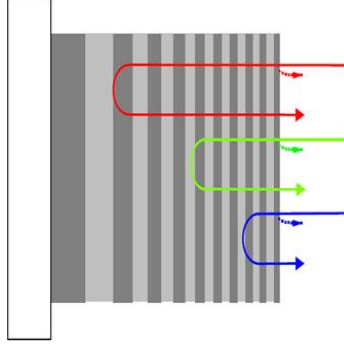


Figure 3.1: Schematic illustration of a single dispersive mirror, where negative GDD and TOD are introduced by interferences at multilayer-coatings resulting in wavelength-dependent penetration depth. The figure is taken from reference [22].

between light and matter. In nonlinear optics, the induced optical polarization $\mathbf{P}(\mathbf{r}, t)$ is generally described as a power Taylor expansion in the incident electric field $\mathbf{E}(\mathbf{r}, t)$ [23]:

$$\begin{aligned} \mathbf{P}(\mathbf{r}, t) &= \mathbf{P}^{(1)}(\mathbf{r}, t) + \mathbf{P}^{(2)}(\mathbf{r}, t) + \mathbf{P}^{(3)}(\mathbf{r}, t) \\ &= \varepsilon_0[\chi^{(1)}\mathbf{E}(\mathbf{r}, t) + \chi^{(2)}\mathbf{E}^2(\mathbf{r}, t) + \chi^{(3)}\mathbf{E}^3(\mathbf{r}, t) + \dots], \end{aligned} \quad (3.17)$$

where $\mathbf{P}^{(1)}(\mathbf{r}, t)$ describes linear optics. $\mathbf{P}^{(2)}(\mathbf{r}, t)$ and $\mathbf{P}^{(3)}(\mathbf{r}, t)$ are the first two terms describing the induced nonlinear optical polarization. $\chi^{(i)}$ ($i = 1, 2, 3$) are the i -th order susceptibility tensors of rank $i+1$. The second-order susceptibility $\chi^{(2)}$ is about twelve orders of magnitude smaller than $\chi^{(1)}$ [23].

For the purpose of this work, only the second-order polarization is of interest. Eq. 3.17 is then reduced to

$$\mathbf{P}^{(2)}(\mathbf{r}, t) = \varepsilon_0\chi^{(2)}(\mathbf{r}, t)\mathbf{E}^2(\mathbf{r}, t). \quad (3.18)$$

In the frequency domain, the corresponding expression for the second-order polarization can be written as

$$\mathbf{P}^{(2)}(\omega, \mathbf{k}) = \varepsilon_0\chi^{(2)}(\pm\omega_1 \pm \omega_2, \pm\mathbf{k}_1 \pm \mathbf{k}_2)\mathbf{E}_1(\omega_1, \mathbf{k}_1)\mathbf{E}_2(\omega_2, \mathbf{k}_2), \quad (3.19)$$

where \mathbf{k}_i and ω_i are the wave vectors and angular frequencies of the i -th monochromatic electric field $\mathbf{E}_i(\omega_i, \mathbf{k}_i)$. In this thesis, we are only interested in the contribution of $\mathbf{P}^{(2)}(\omega, \mathbf{k})$ that oscillates at the frequency $\omega = \omega_1 + \omega_2$, which for the special case of $\omega_1 = \omega_2$, is the source for second harmonic generation (SHG).

The energy diagram of an SHG process is shown in fig. 3.2. A pair of fundamental red photons with frequency ω is annihilated while a single blue photon with frequency 2ω is simultaneously created. This process is instantaneous and parametric, where energy is conserved in the entire process.

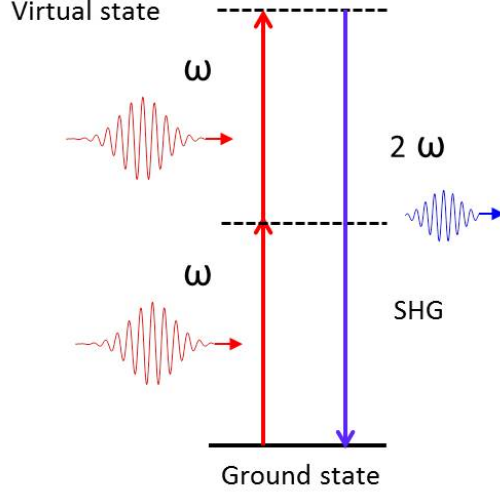


Figure 3.2: Energy diagram describing the quantum mechanic process of second-harmonic generation (SHG). See the text for details.

3.3.1 Description of the SHG signal

By adapting the theoretical description of a two-photon induced fluorescence signal by Xu et al. [24], the number of SHG photons detected per unit time can be presented as

$$S_{SHG}(t) \propto \int_V dV |\mathbf{P}^{(2)}(\mathbf{r}, t)|^4, \quad (3.20)$$

where V is the illuminated sample volume. Using eq. 3.18 and assuming a homogenous non-linear medium with $\chi^{(2)}(\mathbf{r}) = \text{constant}$, we obtain

$$S_{SHG}(t) \propto \int_V dV I_0^2(\mathbf{r}, t), \quad (3.21)$$

where $I_0(\mathbf{r}, t) \propto |\mathbf{E}_0(\mathbf{r}, t)|^2$. One can separate time and space dependence of the incident intensity, and then obtains

$$I_0(\mathbf{r}, t) \propto \text{PSF}(\mathbf{r}) I_0(t), \quad (3.22)$$

where $\text{PSF}(\mathbf{r})$ describes the normalized intensity point-spread function for a focusing lens, which describes intensity everywhere in the space near the focus. $I_0(t)$ describes the time-dependent intensity of the incident light. In practice, only the time-averaged SHG photon flux $\langle S_{SHG}(t) \rangle$ is experimentally measurable. Substituting eq. 3.22 into eq. 3.21 results in

$$\langle S_{SHG}(t) \rangle \propto \langle I_0^2(t) \rangle \int_V dV \text{PSF}^2(\mathbf{r}). \quad (3.23)$$

3.3.1.1 Temporal dependence

For pulsed excitation with a mode-locked laser producing pulses with a duration τ_p and a repetition rate f , $\langle I_0^2(t) \rangle$ in eq. 3.23 can be obtained from the second-order temporal coherence of

the excitation source,

$$g = \frac{\langle I_0^2(t) \rangle}{\langle I_0(t) \rangle^2} = \frac{g_p}{f\tau_p}, \quad (3.24)$$

where g_p is an unitless factor that depends on the temporal laser pulse shape. For a sech^2 pulse, $g_p=0.588$ [24]. Combining eq. 3.23 and eq. 3.24, we obtain the temporal dependence of the SHG signal

$$\langle S_{SHG}(t) \rangle \propto \frac{\langle I_0(t) \rangle^2 g_p}{f\tau_p} \int_V dV \text{PSF}^2(\mathbf{r}). \quad (3.25)$$

Since for a given two-photon excitation focus volume $\langle I_0(t) \rangle$ is directly proportional to the time-averaged excitation power $\langle P_0(t) \rangle$ [24], eq. 3.25 can then be expressed as a function of experimental parameters only:

$$\langle S_{SHG}(t) \rangle \propto \frac{\langle P_0(t) \rangle^2}{f\tau_p}. \quad (3.26)$$

Eq. 3.26 clearly demonstrates the quadratic dependence of the SHG signal on the average excitation power. Furthermore, when the average power and repetition rate of the excitation pulse train are kept constant, the SHG signal is inversely proportional to the pulse duration.

3.3.1.2 Spatial dependence

To describe the two-photon excitation volume for a tightly focused laser beam, we consider an uniform illumination of the back aperture of the focusing objective lens with a collimated Gaussian beam. The approximation of uniform illumination holds as long as the $1/e$ beam diameter of the Gaussian beam is no less than the back aperture diameter of the objective lens. The two-photon excitation volume is then given by $\text{PSF}^2(\mathbf{r})$, which can be calculated using the full vectorial description of the electric field within the diffraction-limited focus volume [25]. A good approximation is provided by a three-dimensional Gaussian volume [1]

$$[\text{PSF}(x, y, z)]^2 \propto e^{-\left(\frac{x^2}{w_{xy}^2} + \frac{y^2}{w_{xy}^2}\right)} e^{-\frac{z^2}{w_z^2}}, \quad (3.27)$$

where w_{xy} and w_z are the lateral and axial $1/e$ radii of $\text{PSF}^2(x, y, z)$, respectively. Expressions for relating the Gaussian parameters w_{xy} and w_z with the dimensions of the diffraction-limited focus volume obtained with an objective of numerical aperture NA have been estimated by Zipfel et al. [1]

$$w_{xy} = \begin{cases} \frac{0.320\lambda}{\sqrt{2}NA} & , NA \leq 0.7 \\ \frac{0.325\lambda}{\sqrt{2}NA^{0.91}} & , NA > 0.7 \end{cases} \quad (3.28)$$

$$w_z = \frac{0.532\lambda}{\sqrt{2}} \left[\frac{1}{n_{med} - \sqrt{n_{med}^2 - NA^2}} \right], \quad (3.29)$$

where n_{med} and λ are the refractive index of the immersion medium and the excitation laser wavelength, respectively.

In our experiments, the FWHM of the lateral and axial SHG intensity profiles will be analyzed, which are more common measures of spatial resolution in nonlinear optical microscopy. The corresponding FWHM_{xy} and FWHM_z are obtained by multiplying eqs. 3.28 and 3.29, respectively, with the factor $2\sqrt{\ln 2}$. The case where the back-aperture is not fully filled with the collimated Gaussian beam has been discussed by Helmchen et al. [26].

3.3.2 Simulation of the SHG spectrum

In contrast to the simple monochromatic waves considered in eq. 3.19, here we take the general frequency-dependence of the pulse electric field (see eq. 3.5) into account. For simplicity, we assume an instantaneous SHG response, such as that of a KDP crystal as an example, where $\chi^{(2)}$ is frequency independent [27]. The second-order polarization is then expressed as a convolution integral:

$$P^{(2)}(2\omega) \propto \int_{-\infty}^{\infty} d\omega' E(\omega') E(\omega - \omega'), \quad (3.30)$$

where all combinations of frequency components of the fundamental pulse contribute to sum-frequencies of the induced polarization. In the experiments, the SHG power spectrum is measured, which can be written as:

$$I_{SHG}(2\omega) \propto |H(2\omega)|^2 |P^{(2)}(2\omega)|^2. \quad (3.31)$$

$H(2\omega) = R(2\omega)e^{-i\varphi_d(2\omega)}$ represents the complex optical transfer function of the optical system that consists of both the SHG collection and detection elements. Consequently, $|R(2\omega)|^2$ is the spectral intensity response of the spectral filters and the detector at the SHG frequencies.

3.3.3 The SHG interferometric autocorrelation function

The SHG interferometric autocorrelation (SHG IAC) is one of the most common and robust techniques, which are used to characterize an ultrashort pulse. In a Michelson interferometer setup, the incoming pulse is split in two replicas with a beamsplitter. A path length difference is introduced between both replicas before recombined by the same beamsplitter, which is resulting in a time delay τ . The combined collinear pulses are focused into a nonresonant nonlinear optical medium with $\chi^{(2)} \neq 0$. The induced second-order polarization can then be written as [28]

$$P^{(2)}(\tau, t) \propto \int_{-\infty}^{\infty} dt' R(t') E^2(\tau, t, t'), \quad (3.32)$$

where $R(t')$ is the temporal response function of the nonresonant nonlinear medium with an instantaneous Dirac function response $\delta(t')$, such as

$$R(t') = A_{NR}\delta(t'). \quad (3.33)$$

A_{NR} is a constant value that is proportional to the strength of nonresonant response. The combined electric field is given by:

$$E(\tau, t, t') = E(t - t') + E(t - t' + \tau), \quad (3.34)$$

where the temporal dependence of the electric field can be obtained by Fourier transformation

$$E(t) = \frac{1}{2\pi} \int_{-\infty}^{\infty} \sqrt{I(\omega)} e^{-i[\varphi(\omega, GDD, TOD) - \omega t]} d\omega. \quad (3.35)$$

Here, $I(\omega)$ represents the pulse intensity spectrum, and $\varphi(\omega, GDD, TOD)$ is the spectral phase of the incident pulse for a given GDD and TOD. Considering the spectral modulation induced by the transmission of optical filters $T_F(2\omega)$ and the spectral sensitivity of the SHG collection system $T_{Det}(2\omega)$, we introduce the optical transfer function $|H(2\omega)| = \sqrt{T_F(2\omega)T_{Det}(2\omega)}$ in the frequency-domain. The detected SHG IAC intensity as a function of the time delay τ between two pulses can then be written as

$$I_{SHGIAC}(\tau) \propto \int_{-\infty}^{\infty} |\mathcal{F}[\mathcal{F}^{-1}[P^{(2)}(\tau, t)]H(2\omega)]|^2 dt. \quad (3.36)$$

In an actual SHG IAC trace experiment, one commonly analyzes the SHG IAC intensity when normalized to its value at $\tau = \infty$, such that

$$I_{SHGIAC}^{exp}(\tau) = \frac{I_{SHGIAC}(\tau)}{I_{SHGIAC}(\tau = \infty)}. \quad (3.37)$$

From this equation, one can show that for a pure second-order nonlinear process, the ratio between maximum intensity at $\tau = 0$ and constant intensity at $\tau = \infty$ has to be $\frac{I_{SHGIAC}(\tau=0)}{I_{SHGIAC}(\tau=\infty)}=8$ [28]. From the above derivation of eqs. 3.36 and 3.37 follows that an SHG IAC trace measured in nonresonant nonlinear optical medium not only depends on the intensity spectrum $I(\omega)$ and on the chirp parameters, GDD and TOD, of the incident pulses at the sample, but also depends on the spectral transfer function of the SHG collection and detection optical systems.

The SHG intensity autocorrelation (AC) function is also commonly used to harvest quantitative information about the temporal structure of an ultrashort pulse, which is defined as:

$$I_{SHGAC}(\tau) \propto \int_{-\infty}^{\infty} I(t)I(t - \tau)dt, \quad (3.38)$$

where $I(t) \propto |E(t)|^2$. The SHG AC function can be extracted from an SHG IAC experiment by Fourier filtering:

$$I_{SHGAC}^{exp}(\tau) = \frac{1}{2} \left\{ \mathcal{F} \left\{ \mathcal{F}^{-1} [I_{SHGIA}^{exp}(\tau)] \cdot f(\omega) \right\} - 1 \right\}, \quad (3.39)$$

where the filter function is defined as

$$f(\omega) = \begin{cases} 1 & , |\omega| \leq \frac{\omega_0}{2} \\ 0 & , |\omega| > \frac{\omega_0}{2} \end{cases} \quad (3.40)$$

In eq. 3.39, all frequency components at around $\pm\omega_0$ and $\pm 2\omega_0$ (ω_0 is the carrier frequency of the incident optical pulses) in the interferometric autocorrelation function $I_{SHGIAC}^{exp}(\tau)$ are rejected. If an analytical pulse shape for a Fourier-limited *sech*² pulse (see eq. 3.8) is assumed, the corresponding analytical expression for the intensity autocorrelation trace can be written as [28]:

$$I_{SHGIAC}(\tau) = \frac{3 \cdot \left\{ \frac{1.763\tau}{\tau_p} \cosh\left(\frac{1.763\tau}{\tau_p}\right) - \sinh\left(\frac{1.763\tau}{\tau_p}\right) \right\}}{\sinh^3\left(\frac{1.763\tau}{\tau_p}\right)}. \quad (3.41)$$

3.3.4 SHG polarization dependence for a dipole scatterer

For a single dipole scatterer, for example a gold nanorod, the highest probability of linear optical scattering occurs when the transition moment is oriented parallel to the linear polarization of the incident electric field. The linear scattered light intensity exhibits the following dependence on the angle α between the incident linear polarization of the excitation field and the orientation of the dipole moment α_0 [29]

$$I_{linear}(\alpha) \propto \cos^2(\alpha - \alpha_0). \quad (3.42)$$

For second-order nonlinear dipole scattering, the corresponding dependence of the SHG intensity measured without the use of any analyzer is then given by [30]

$$I_{SHG}(\alpha) \propto \cos^4(\alpha - \alpha_0). \quad (3.43)$$

Consequently, the measured SHG intensity polarization distribution is narrower than the linear scattering polarization distribution. This characteristic allows more sensitive measurements of the dipole scatterer orientation when SHG experiments are performed.

3.4 Optical properties of gold nanoparticles

Metallic nanoparticles (MNPs) have fascinated people for many centuries because of their special optical properties. The milestone of modern nanotechnology is a lecture given by Faraday to the Royal Society in London in 1857 [31], where he first awarded that there are small MNPs in gold solutions. In 1908, Mie did the first theoretical studies on the optical behavior of MNPs [32]. Nowadays, the interaction of light with MNPs is a subject of extensive experimental and theoretical research, which is due to the optical resonance phenomenon of the so called localized surface plasmon resonance (LSPR) [33] [34] [6].

In this section, first, the Drude-Sommerfeld theory of bulk gold is introduced. Second, the descriptions of LSPR modes in a gold nanoparticle by using Mie theory and the quasi-static approximation are demonstrated. In order to describe the SHG response of LSPR modes, the

driven damped harmonic oscillator model is introduced, and the plasmon resonance enhanced SHG IAC function is simulated.

3.4.1 Drude-Sommerfield theory

A description of the dielectric function $\varepsilon(\omega)$ of bulk gold is given by the Drude-Sommerfield theory, which assumes independent and quasi-free electrons with a common relaxation time. The dielectric function can be written as [35] [36] [37]:

$$\varepsilon(\omega) = \varepsilon'(\omega) + i\varepsilon''(\omega) = \varepsilon_\infty - \frac{\omega_p^2}{\omega(\omega + i\gamma_0)}, \quad (3.44)$$

where γ_0 and ε_∞ are the electron relaxation rate and the dielectric offset that accounts for the accumulated contributions of the interband transition to the dielectric function not considered in the present model [37]. The plasma frequency is represented by $\omega_p = \sqrt{n_e e^2 / \varepsilon_0 m_e^*}$, with e , n_e , and m_e^* being electron charge, electron density, and effective mass of the electron, respectively. Figs. 3.3 (a) and (b) show the real $\varepsilon'(\omega)$ and imaginary $\varepsilon''(\omega)$ parts of the dielectric function of bulk gold, respectively, which were obtained by reflection and transmission measurements on vacuum-evaporated thin gold films by Johnson and Christy in 1972 [38]. The best fit of the experimental data within the photon energy range from 1.4 to 1.75 eV to the Drude-Sommerfield theory (eq. 3.44) results in $\hbar\omega_p = 9.0$ eV, $\gamma_0^{-1} = 10$ fs, and $\varepsilon_\infty = 9.8$ [37]. While for photon energies below 1.8 eV, the fit matches well to the experimental data when interband contributions below 1.8 eV are taken into account by ε_∞ , the quasi free electron model breaks down for higher photon energies. The imaginary part strongly deviates from the quasi-free electron model above 1.8 eV, which originates from interband transition from the d-band into the conduction band and from an increasing anharmonicity of the conduction band at higher photon energies.

The simple picture provided by the Drude-Sommerfield model shows that the relaxation time of quasi-free electrons in bulk gold due to collisions with other electrons, ions, defects, and phonons occurs on the time scale of about 10 fs. In addition, the direct excitation of interband transitions are negligible in the near-infrared region in bulk gold.

3.4.2 LSPR modes in a gold nanoparticle

It is common to express the optical properties of a single metallic nanoparticle in terms of scattering σ_{sca} and absorption σ_{abs} cross sections, which are related to the intensity losses $\Delta I_{sca}(z)$ and $\Delta I_{abs}(z)$, respectively, of a parallel beam of incident light propagating along z-axis according to the Beer-Lambert law [39]:

$$\Delta I_{sca}(z) = I_0(1 - e^{-\# \sigma_{sca} z}) \quad (3.45)$$

$$\Delta I_{abs}(z) = I_0(1 - e^{-\# \sigma_{abs} z}). \quad (3.46)$$

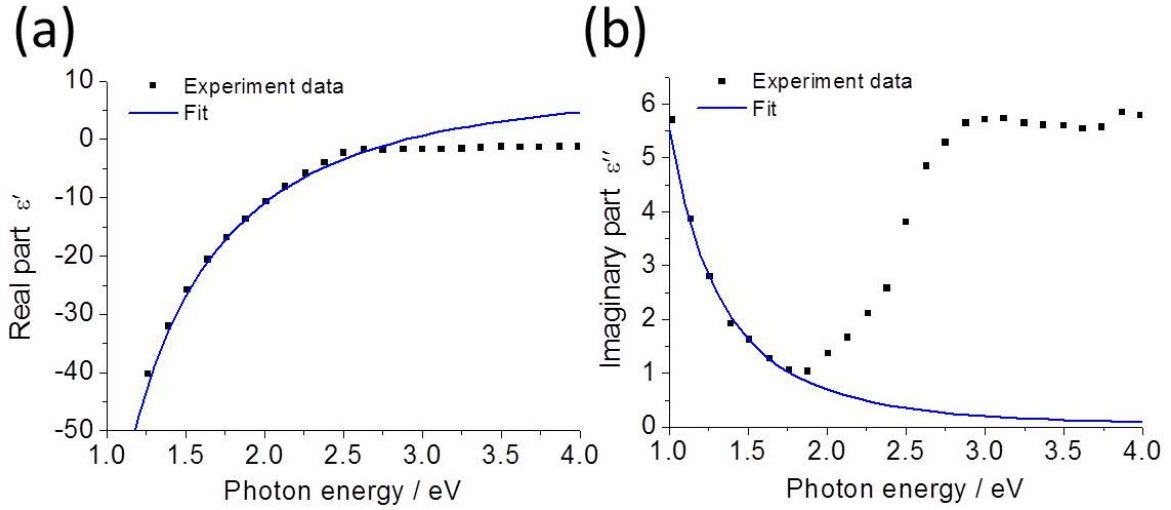


Figure 3.3: The real part (a) and imaginary part (b) of the dielectric function of bulk gold plotted as function of photon energy. The black dots and blue curves represent the experimental data reported by Johnson and Christy [38] and their best fit to eq. 3.44 within the interval [1.4, 1.75] eV [37], respectively.

Here, $\#$ is the number density, and I_0 is the incident light intensity. Both absorption and scattering contribute to the extinction cross section given by [39]

$$\sigma_{ext} = \sigma_{sca} + \sigma_{abs}. \quad (3.47)$$

For a gold nanoparticle with dimensions comparable or smaller than the incident electric field penetration depth of about 30 nm in the visible wavelength range [39], the absorption contribution dominates the extinction cross section. With increasing size of the nanoparticle, the scattering contribution increases [29].

3.4.2.1 Mie theory

The resonance frequency of the LSPR not only depends on the dielectric functions of the metal and the surrounding medium, but also is largely affected by the size and shape of the nanoparticle. The Mie theory provides a full description for the interaction of electromagnetic radiation with an uncharged spherical MNP in a homogeneous medium by solving Maxwell's equations [32]. Analytical expressions for the scattering and extinction cross sections are then represented as [40]

$$\sigma_{sca} = \frac{2\pi}{k^2} \sum_{l=1}^{\infty} (2l+1)(|a_l|^2 + |b_l|^2) \quad (3.48)$$

and

$$\sigma_{ext} = \frac{2\pi}{k^2} \sum_{l=1}^{\infty} (2l+1)Re(a_l + b_l), \quad (3.49)$$

respectively. a_l and b_l are the Mie coefficients, (see ref. [40] for analytical expressions), which are functions of (1) the ratio between the refractive index of the MNP and the refractive index of the surrounding medium, (2) the wave vector $k = \frac{2\pi}{\lambda}$, and (3) the radius of the nanoparticle (see eq. 3.67). The number l represents the order of the multipole extension of the fields. For $l = 1$, this represents a dipole mode. Fig. 6.4 shows an example of LSPR in the scattering cross section spectrum for a single 50-nm gold nanosphere embedded in a homogeneous medium with refractive index $n=1.518$ that has been calculated using Mie theory.

3.4.2.2 The quasi-static approximation

When a nanoparticle is much smaller than the excitation wavelength, the electromagnetic field imposing on MNP can be viewed as both spatially and temporally constant, and only the dipole mode ($l = 1$ in eqs. 3.49 and 3.48) needs to be considered. In this quasi-static (Rayleigh) approximation, phase retardation effects are neglected. Considering an ellipsoidal shape of nanoparticle with three principal semi-axes (a, b, c), this simple picture leads to an electric polarizability $\alpha_i(\omega)$ of such an ellipsoid along the principal axis i ($i = a, b, c$), which is given by [39]

$$\alpha_i(\omega) = \varepsilon_0 V \frac{\varepsilon(\omega) - \varepsilon_m}{\varepsilon_m + L_i \{\varepsilon(\omega) - \varepsilon_m\}}, \quad (3.50)$$

where L_i is the geometrical factor related to the shape of the nanoparticle. It may take any value from 0 to 1 [40]. For a nanosphere ($a=b=c$), $L_a = L_b = L_c = \frac{1}{3}$. The ellipsoid volume is $V = \frac{4}{3}\pi(abc)$. The scattering and absorption cross sections of an ellipsoidal nanoparticle in an electric field parallel to a principal axis i are given by

$$\sigma_{sca,i}(\omega) = \frac{k^4}{6\pi\varepsilon_0^2} |\alpha_i(\omega)|^2 \quad (3.51)$$

and

$$\sigma_{abs,i}(\omega) = \frac{k}{\varepsilon_0} \text{Im}[\alpha_i(\omega)], \quad (3.52)$$

respectively. Consequently, the cross sections have a resonance at the frequency where the real part of the denominator in eq. 3.50 is zero.

$$\text{Re}[\varepsilon(\omega)] = -\varepsilon_m \frac{1 - L_i}{L_i}. \quad (3.53)$$

For spherical nanoparticles, the resonance condition is given by $\text{Re}[\varepsilon(\omega)] = -2\varepsilon_m$. Considering the special case for a prolate nanoparticle ($a > b = c$), which represents a good approximation for a gold nanorod, the geometry factor along the a -axis L_a decreases with increasing aspect ratio a/b of the nanorod. Consequently, the resonance condition in eq. 3.53 is satisfied at more negative values than $-2\varepsilon_m$ at frequencies that are red shifting with increasing aspect ratio of that nanorod (see fig. 3.3 (a)).

In the case of spherical nanoparticle ($a=b=c$) in the quasi-static approximation, phase retardation and effects of higher multipoles are neglected, and the Mie eqs. 3.48 and 3.49 are drastically simplified [40]:

$$\sigma_{sca}(\omega) = \frac{k^4}{6\pi\epsilon_0^2} |\alpha|^2 = \frac{3}{2\pi} \left(\frac{\omega}{c}\right)^4 V^2 \frac{(\epsilon'(\omega) - \epsilon_m)^2 + (\epsilon''(\omega))^2}{(\epsilon'(\omega) + 2\epsilon_m)^2 + (\epsilon''(\omega))^2} \quad (3.54)$$

$$\sigma_{abs}(\omega) = k\epsilon_0 \text{Im}[\alpha] = 9 \frac{\omega}{c} \epsilon_m^{3/2} V \frac{\epsilon''(\omega)}{[\epsilon'(\omega) + 2\epsilon_m]^2 + [\epsilon''(\omega)]^2}. \quad (3.55)$$

Besides the dependence of the LSPR frequency of a MNP on its size, shape, and dielectric constant of the surrounding medium (see eq. 3.53), the resonance peak intensity of the scattering and the absorption cross sections are proportional to V^2 and V , respectively (see eqs. 3.54 and 3.55), which indicates its strong dependence on the particle size.

There are also limits of the quasi-static approximation [37]: First, it is not clear whether the values for the bulk material properties used for the calculations are indeed valid for particles with nanometer dimensions. Second, it is not clear whether the assumptions in the theoretical models, for example sharp boundaries, no many-body effects, etc. are reasonable. It is worthy to note that Mie theory only provides an analytical solution for spherical particles in a homogeneous medium [32]. For calculating the optical response of nanoparticles with more complicated shapes, numerical treatments are needed [41] [42] [43].

3.4.3 The driven damped harmonic oscillator model

We consider a gold nanoparticle with the a size comparable to the penetration depth of excitation field (about 30 nm in the visible wavelength range [39]). When the particle is irradiated by the electric field, a collective displacement of conduction electrons with respect to the fixed positive charges of lattice ions results in a built-up of surface charges on the nanoparticle. Due to attraction of opposite charges on opposite sides, the restoring force leads to density oscillations of the conduction electrons that are driven by the external force $F_{ext}(t) = qE_{ext}(t)$. The oscillating surface charges can be considered as a dipole oscillating with the damped resonance eigenfrequency Ω , which is the source of the radiation field. To describe the LSPR of the nanoparticle, we consider a plasmon particle with charge q and mass m , where the periodic displacement $x(t)$ is described by the equation of motion for a driven damped harmonic oscillator [44]

$$\ddot{x}(t) + 2\gamma\dot{x}(t) + \Omega^2 x(t) = \frac{q}{m} E_{ext}(t) = \frac{F_{ext}(t)}{m}, \quad (3.56)$$

where the damped eigenfrequency is defined as $\Omega = \sqrt{\omega_{res}^2 - \gamma^2}$. γ and ω_{res} ($\lambda_{res} = \frac{2\pi c}{\omega_{res}}$) are the total damping rate and eigenfrequency (eigenwavelength) of the harmonic oscillator for $F_{ext} = 0$, respectively.

3.4.3.1 Stationary solution

For a periodic external driving force $F_{ext}(t) = F_0 e^{i\omega t}$, where $F_0 = \text{constant}$, the solution of eq. 3.56 is given by [44]

$$x_0(\omega) = \frac{F_0}{m} \frac{1}{[(\Omega^2 - \omega^2) + i2\gamma\omega]} = |x_0(\omega)| e^{i\psi(\omega)}, \quad (3.57)$$

where the oscillation amplitude is

$$|x_0(\omega)| = \frac{F_0}{m} \frac{1}{\sqrt{(\Omega^2 - \omega^2)^2 + 4\gamma^2\omega^2}}. \quad (3.58)$$

From eq. 3.57 follows that the phase between the driving force and the oscillation amplitude is given by

$$\psi(\omega) = \tan^{-1} \left(\frac{-2\gamma\omega}{\Omega^2 - \omega^2} \right). \quad (3.59)$$

The frequency dependent amplitude of the electric field radiated by a LSPR dipole is then given by

$$|\tilde{E}(\omega)| \propto |\tilde{x}(\omega)| = \left| \frac{C_\omega}{m[(\Omega^2 - \omega^2) + i2\gamma\omega]} \right|, \quad (3.60)$$

where $C_\omega = \mathcal{F}^{-1}[F_{ext}(t)]$. The plasmon intensity spectrum $|\tilde{E}(\omega)|^2$ results in a well-known Lorentzian line shape. When $\omega = \Omega$, the intensity has a maximum value. For low damping ($\gamma \ll \omega_{res}$), the FWHM of the Lorentzian curve is given by

$$\Delta\omega = 2\gamma. \quad (3.61)$$

By Fourier transforming $\tilde{x}(\omega)$, the corresponding expression for the real part of the plasmon field in the time-domain can be written as

$$\text{Re}[E(t)] \propto \cos(\Omega t) e^{-\gamma t}. \quad (3.62)$$

The dephasing time T_2 denotes the 1/e decrease of the oscillation amplitude, whereas the decay time T_1 denotes the 1/e decrease of the oscillation energy. These two time constants are related to each other by

$$T_2 = 2T_1 = \frac{1}{\gamma}. \quad (3.63)$$

For illustration of the relationship between eq. 3.60 and eq. 3.62, a simulated example for a single Lorentzian resonance with $\hbar\omega_{res} = 1550$ meV and $T_2 = 10$ fs is plotted in figs. 3.4 (a) and (b), respectively.

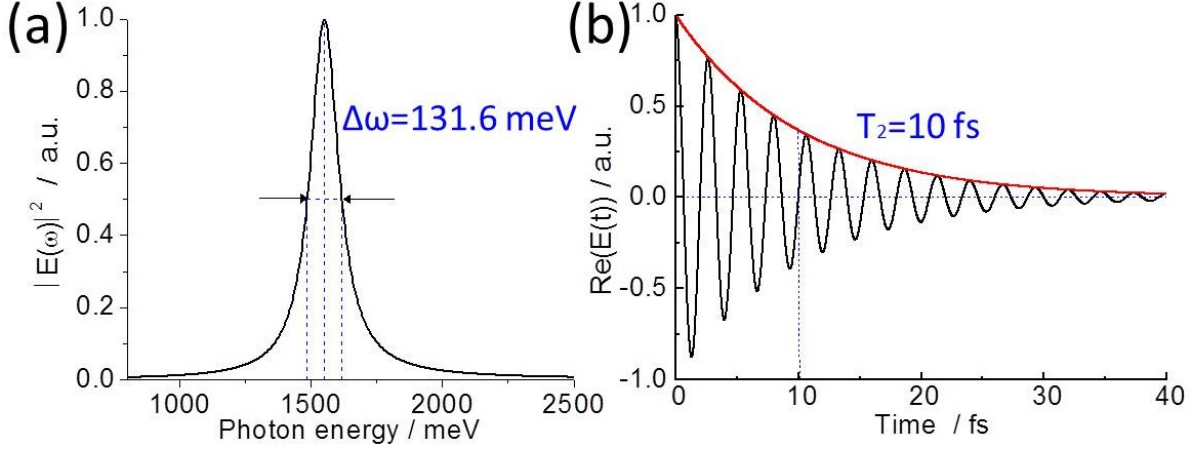


Figure 3.4: (a) A Lorentzian line shape describing LSPR plasmon electric field with $\hbar\omega_{res}=1550$ meV and $T_2=10$ fs in the frequency-domain. (b) The corresponding real part of the plasmon induced electric field with $T_2 = 10$ fs in the time-domain.

Beyond the single nanoparticle picture discussed above, inhomogeneous broadening of many different oscillating dipoles needs to be taken into account when an ensemble of different nanoparticles is present. Here, the destructive interference of the oscillating dipoles results in a faster decay when compared to the dephasing time T_2 of an individual dipole. Consequently, the ensemble dephasing time T' can be written as

$$\frac{1}{T'} = \frac{1}{T_2} + \frac{1}{T^*}, \quad (3.64)$$

where T^* is the dephasing time introduced by the inhomogeneous broadening effect.

3.4.3.2 Non-stationary solution

Because the plasmon dephasing times of the particle are comparable to the pulse duration of our few-cycle laser pulses, the stationary solution of eq. 3.56 is not a suitable model to simulate a driven damped particle plasmon oscillation in our time-resolved experiments. One has to find a non-stationary solution of the equation of motion. By assuming an external driving force for a single Dirac $\delta(t-t^*)$ function 'stroke' acting at $t = t^*$, $F_{ext} = z\delta(t-t^*)$ and $\delta(t-t^*) = 0$ for $t \neq t^*$ and $\int_{-\infty}^{\infty} \delta(t-t^*)dt = 1$, the non-stationary solution of eq. 3.56 driven by this 'stroke force' can be written as [44]

$$x(t) = \frac{Z}{m\Omega} e^{-\gamma(t-t^*)} \sin\Omega(t-t^*) \quad \text{for } t > 0. \quad (3.65)$$

An arbitrary time-dependent driving force $F_{ext}(t)$ can be considered as a time sequence of infinitesimal small 'stroke forces' with an area $F_{ext}(t^*)dt^*$. The general non-stationary solution of eq. 3.56 can then be written as the integral over all the solutions for the individual 'stroke forces' [44]

$$x(t) = \frac{1}{m\Omega} \int_{-\infty}^t dt^* F_{ext}(t^*) e^{-\gamma(t-t^*)} \sin\Omega(t-t^*). \quad (3.66)$$

Eq. 3.66 describes the coherent motion of electrons in a metal nanoparticle under the influence of an ultrashort pulse, which will be used to theoretically describe the plasmon resonance enhanced SHG response in the time-domain (see section 3.4.5).

3.4.4 Plasmon dephasing mechanisms

As reviewed by Sönnichsen et al. [29], the main mechanisms involved in plasmon dephasing processes in metallic nanoparticles are summarized as follows:

(1) Radiative damping

The radiative damping occurs via emission of photons, which can be observed in the dark field as scattered light. According to the Abraham-Lorentz equations of motion, which are extensions of the Drude-Sommerfeld theory, the radiative decay rate γ_{rad} in a nanoparticle scales with its volume V [45] [29],

$$\gamma_{rad} \propto V. \quad (3.67)$$

(2) Nonradiative interband damping

For the interband excitation, the electrons are excited from the energetically deeper d-band into the conduction band, which require a threshold energy of about 1.8 eV in gold (see fig. 3.3 (b)). For the photon energies below 1.8 eV, the interband damping rate γ_{inter} for plasmon decay can be neglected.

(3) Nonradiative intraband damping

For the intraband excitation, the electrons are excited within the conduction band. From the Drude-Sommerfeld theory for metals, one can deduce that the intraband damping rate γ_{intra} is constant over the near-infrared wavelength range with $\gamma_{intra}^{-1} \approx 18$ fs [29].

The total damping rate γ_{total} , which can be written as the sum of these three mechanisms

$$\gamma_{total} = \gamma_{rad} + \gamma_{inter} + \gamma_{intra}, \quad (3.68)$$

exhibits a lower boundary given by γ_{intra} , and the contribution of the radiation damping increases with the increasing of size of the nanoparticle.

3.4.5 Simulation of the plasmon resonance enhanced SHG IAC function

By modeling the LSPR of a metallic nanoparticle as a driven damped harmonic oscillator, we can express the induced second-order polarization as a function of time delay τ between the two pulses in a typical SHG IAC trace measurement as [46]

$$P^{(2)}(\tau, t) \propto [x^{(1)}(\tau, t)]^2, \quad (3.69)$$

where $x^{(1)}(\tau, t)$ is the first-order displacement of the driven damped harmonic oscillator. By using the non-stationary solution presented in eq. 3.66, we obtain

$$x^{(1)}(\tau, t) \propto \int_{-\infty}^t E(\tau, t')R(t-t')dt' \quad (3.70)$$

with the temporal response function for a nonlinear medium with a single Lorentzian resonance given by

$$R(t-t') = \frac{1}{\Omega} e^{-(t-t')/T_2} \sin[\Omega(t-t')] \quad (3.71)$$

and with the combined electric field given by

$$E(\tau, t') = E(t') + E(t' - \tau). \quad (3.72)$$

By Fourier transformation, the time-dependent electric field $E(t')$ can be obtained from the intensity pulse spectrum for given GDD and TOD values (see eq. 3.35). The simulation of the experimental SHG IAC intensity is performed in accordance with eqs. 3.36 and 3.37, where the optical transfer function for the SHG collection and detection optical systems $|H(2\omega)|$ is taken into account.

In addition to the optical pulse properties at the sample (pulse spectrum, GDD, and TOD) and to the spectral SHG optical transfer function $|H(2\omega)|$, the plasmon resonance enhanced SHG IAC function also depends on resonance properties of the nonlinear scatterer. Consequently, for a $\chi^{(2)}$ -active medium characterized by a single Lorentzian resonance, one can retrieve its dephasing time T_2 and resonance wavelength λ_{res} by fitting a measured SHG IAC trace with a simulated SHG IAC trace when the optical properties of incident pulses and spectral transfer function for the experimental setup are known.

3.5 Linear optical properties of a single nanohole in a gold film

Besides the discovery of the extraordinary light transmission [47], the linear optical properties of a nanohole in a metal film have been experimentally and theoretically demonstrated to show a strong size- and shape-dependence. Distinguished LSPR dipole characteristics were observed for an isolated nanohole, which exhibits a size dependent resonance shift of the transmission and a pronounced polarization effect, similar to those observed for an isolated nanoparticle [48–51].

The similar optical properties of the nanohole and the nanoparticle are qualitatively related to each other via Babinet's principle, which relates the fields scattered by two complementary plane structures made of infinitely thin and perfectly conducting sheets of arbitrary shape, provided that both structures are illuminated by complementary electromagnetic fields [12]. For illustration, in fig. 3.5 (a) we consider a single rectangular gold nanoparticle, as will be studied

in chapter 6. The complementary structure shown in fig. 3.5 (b) then represents a rectangular nanocavity of the same dimensions in a gold film, as will be discussed in chapter 7. For an incident electromagnetic field, \mathbf{E}_0 and \mathbf{B}_0 , that is scattered by the nanoparticle, the complementary electromagnetic field, \mathbf{E}_0^c and \mathbf{B}_0^c , that is scattered by the complementary nanocavity is then defined as

$$\begin{aligned}\mathbf{E}_0^c &= -c\mathbf{B}_0 \\ \mathbf{B}_0^c &= \frac{1}{c}\mathbf{E}_0,\end{aligned}\quad (3.73)$$

which corresponds to a 90° rotation along the propagation axis (see fig. 3.5).

For the electric field \mathbf{E}_0 incident on the rectangular nanoparticle, which propagates perpendicular to the x-y sample plane and is linearly polarized parallel to the long axis of the nanoparticle, an induced surface charge distribution with electric field $\mathbf{E}_{ind}(\omega) = -\alpha(\omega)\mathbf{E}_0(\omega)$ (see fig. 3.5 (a)) creates an electric dipole parallel to the x-axis. This dipole describes the long axis plasmon resonance in a rectangular metallic nanoparticle. For the complementary structure, the incident electric field and magnetic field interchange according to eq. 3.73, and the surface charge in the rectangular nanoparticle (see fig. 3.5 (a)), can be transferred to the magnetic flux in the complementary nanocavity, which is parallel to the x-axis. Consequently, an electric dipole parallel to the short axis of the rectangular nanocavity is induced with $\mathbf{E}_{ind}^c(\omega) = -\alpha^c(\omega)\mathbf{E}_0^c(\omega)$ (see fig. 3.5 (b)). In summary, Babinet's principle implies that the spectral response of the structure for a given incident electric field polarization corresponds to that of its complement for the orthogonal electric field polarization. Despite the deviations from the assumptions of infinitely thin and perfectly conducting sheets, the conformity of Babinet's principle was qualitatively verified for plasmonic nanostructures and metamaterials with intrinsic resonances in the THz [13] [52] [53] and mid-infrared [14] [54] [55] frequency ranges.

The LSPR characteristics of elongated nanoholes in thin metal films with a resonance wavelength in the visible and near-infrared range have also been demonstrated to follow the opposite polarization and shape dependence of the optical response when compared to those of a complementary elongated metallic nanoparticle [50], which is in qualitative agreement with Babinet's principle. By using the quasi-static approximation for describing the optical properties of an ellipsoidal nanocavity embedded in a metal film, the corresponding polarizability along the i-th semi-axis of the ellipsoid is given by [40]

$$\alpha_i^c(\omega) = \varepsilon_0 V \frac{\varepsilon_m - \varepsilon(\omega)}{\varepsilon(\omega) + L_i\{\varepsilon_m - \varepsilon(\omega)\}} \quad (i = a, b, c). \quad (3.74)$$

This expression is equivalent to eq. 3.50 describing the polarizability of an ellipsoidal nanoparticle when ε_m and $\varepsilon(\omega)$ are interchanged. For the complementary elongated ellipsoidal nanocavity, the resonance condition is defined when the real part of the denominator in eq. 3.74 is zero,

such as

$$Re[\varepsilon(\omega)] = -\varepsilon_m \frac{L_i}{1 - L_i}. \quad (3.75)$$

For a spherical nanocavity, the resonance is given by $Re[\varepsilon(\omega)] = -\frac{\varepsilon_m}{2}$. Unlike the elongated nanoparticle, the resonance of an elongated ellipsoidal nanocavity is induced in the direction of its short axis when $Re[\varepsilon(\omega)] < -\frac{\varepsilon_m}{2}$, and consequently this LSPR is also red-shifting with increasing aspect ratio of the elongated nanohole [50].

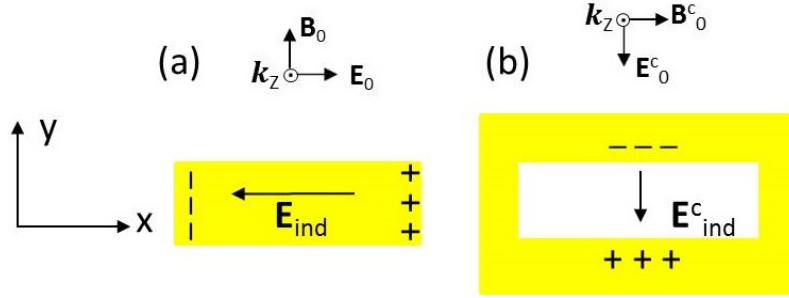


Figure 3.5: (a) Rectangular metallic nanoparticle with the distribution of surface charge when excited with linearly polarized electromagnetic field, \mathbf{E}_0 and \mathbf{B}_0 , propagating along \mathbf{k}_z . When the electric field \mathbf{E}_0 is parallel to the x-axis, the LSPR induced electric dipole field \mathbf{E}_{ind} is also oriented along the x-axis. (b) The complementary structure of (a), which is a rectangular nanohole in metal film, with the distribution of the surface charge excited with a complementary electromagnetic field, \mathbf{E}_0^c and \mathbf{B}_0^c . Here, the magnetic field \mathbf{B}_0^c is parallel to the x-axis, and the induced electric dipole field \mathbf{E}_{ind}^c is oriented along the y-axis. A frequency below resonance frequency is assumed.

Although the above pictures of both Babinet's principle and the quasi-static approximation for an elongated ellipsoidal nanocavity in a metal film qualitatively describe the main linear optical properties of plasmon resonances in nanoholes, there exist important differences when compared to those of the complementary nanoparticles [50]: First, the dipolar localized surface plasmon excitation in the nanocavity can decay non-radiatively to surface plasmon polaritons (SPPs) in the surrounding metal film. This additional contribution to the LSPR damping rate thus results in a spectral bandwidth and center wavelength of the resonance that are broader and more red-shifted, respectively, with respect to those of the complementary nanoparticle. In addition, since the nanocavity cannot be polarized in the direction perpendicular to the metal film, the resonance condition (eq. 3.75) is already fulfilled for $Re[\varepsilon(\omega)] < -\varepsilon_m \frac{L_i}{1 - L_i}$, which accounts for the strong red-shift of the LSPR peak for an elongated nanocavity.

In analogy to the LSPR enhanced second-order polarization for a single nanoparticle, where the resonance was modeled as driven damped harmonic oscillator (see section 3.4.3), the hypothesis of this thesis is to observe a similar LSPR enhancement of SHG from a single nanocavity. Provided that the additional damping caused by the coupling of the LSPR of the nanocavity

to the SPP of the surrounding metal is not beyond the temporal resolution of our SHG IAC experiment, we expect to directly observe the size- and shape-dependence of the plasmon dephasing time in the nanocavity. Furthermore, the polarization dependence of the plasmon resonance enhanced SHG is expected to be rotated by 90° when compared to that of its complementary nanoparticle, according to Babinet's principle.

4 Experimental methods

In this chapter, the optical setup of the few-cycle NLO microscope system and the system control software are described. The data analysis methods, which are common to all the experiments are also summarized here. Details of specific sample preparation procedures, experimental conditions, and simulation tools are listed in the methods section at the beginning of each result chapter.

4.1 Optical setup of the few-cycle NLO microscope system

The experimental setup that allows NLO imaging and spectroscopy in both time and frequency domains, linear dark field scattering imaging and spectroscopy, linear transmission spectroscopy of one and the same sub-micron object is shown in fig. 4.1. The overall system consists of six individual units, which are considered separately: 1. few-cycle laser source (**Laser**), 2. interferometric autocorrelator (**IA**), 3. dispersion management unit (**DMU**), 4. beam management unit (**BMU**), 5. microscope (**microscope**), 6. dark-field (**DF**) and transmission microspectroscopy .

4.1.1 Few-cycle laser source

As a laser source, a commercial few-cycle pulsed Ti:Sapphire oscillator (Femtolasers Rainbow UHP) operating at 76 MHz repetition rate, which is pumped by a 4.4 W cw laser operating at 532 nm (Coherent Verdi G7) is used. The average power of the oscillator output is 500 mW. The output pulse has a duration of 6.4 fs ($sech^2$) and spectral bandwidths of FWHM = 173 nm and FWTM = 307 nm, centered at 820 nm, as shown in fig. 4.2. The procedure to extract the pulse duration is described in section 4.3.1. The residual dispersion values $GDD = 0 fs^2$ and $TOD = 120 fs^3$ are obtained by fitting the experimental SHG IAC trace with the simulated SHG IAC trace based on eqs. 3.36 and 3.37. Here, the $E(t)$ used in the simulations is obtained by the Fourier transform of the square root of the measured pulse spectrum where the polynomial phase is introduced (see eqs. 3.10 and 3.35). The effect of higher order dispersion can be neglected. The pulse has a time-bandwidth product (TBP) of 0.49, which is close to

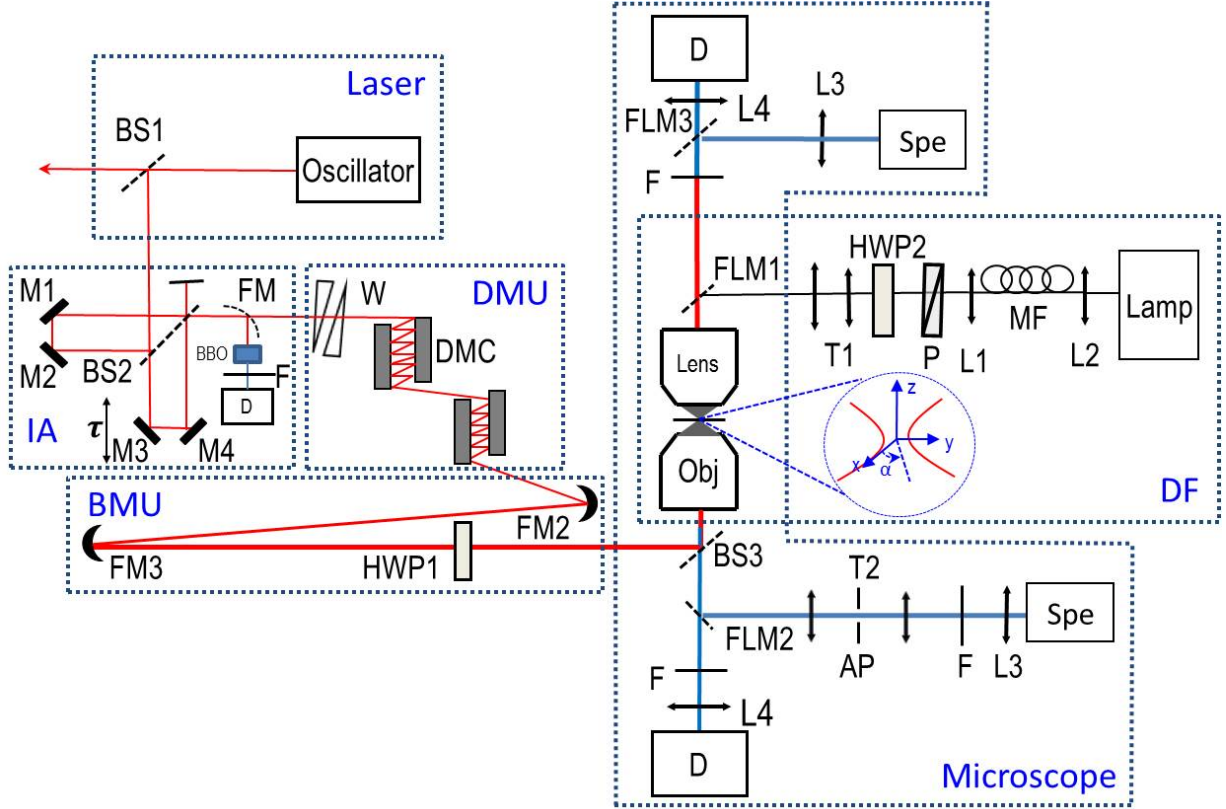


Figure 4.1: Layout of the optical setup of the home-built NLO microscope system, consisting of a few-cycle laser source, an interferometric autocorrelator, a dispersion management unit, a beam management unit, a microscope, and a dark-field and transmission microspectroscopy. See text for details about each component.

the Fourier-limited value for a sech^2 pulse of $c_B = 0.315$ [16]. The linearly polarized pulse is parallel to the optical table plane.

4.1.2 Interferometric autocorrelator unit

A dispersion-balanced interferometric autocorrelator (IA) based on a typical Michelson interferometer was built to characterize the few-cycle laser pulses. The incoming laser pulse, which is a 10% fraction of the oscillator output pulse reflected by the beam splitter (**BS1**, Femtolasers OA078) is split into two replica pulses, using a beamsplitter (**BS2**, Femtolasers FO002), which has a constant splitting ratio over a large spectral bandwidth. One of the replica pulses experiences a variable delay with respect to the other pulse by moving a pair of mirrors mounted on a piezoelectric actuator (Physik Instrumente P-601.4SL), which has a traveling range of up to 400 μm with a position accuracy of 0.4 nm. All mirrors used are broadband low-GDD mirrors (**M1**, **M2**, **M3**, **M4**, Femtolasers FO009). After recombination at the beamsplitter (**BS2**), both pulses propagate collinearly. In order to characterize the oscillator output pulse, a flippable off-axis parabolic focusing mirror (**FM1**, Femtolasers OA027, $f = 50$ mm) is implemented to focus the

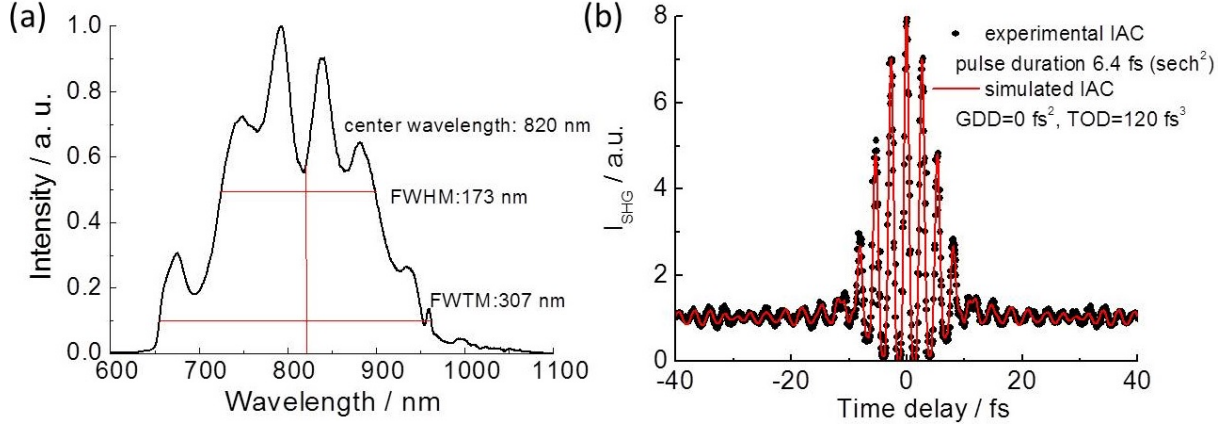


Figure 4.2: The characterization of the oscillator output pulse. (a) Measured oscillator pulse spectrum exhibiting FWHM = 173 nm, FWTM = 307 nm, and centered at 820 nm. (b) The measured (black dot) and the simulated (red line) SHG IAC traces of the pulse, which is best fit to a duration of 6.4 fs ($sech^2$) and residual values of GDD = 0 fs^2 and TOD = 120 fs^3 .

combined pulses into a 20 μm thick beta barium borate crystal (**BBO**, Newlight BTC 2512-2 Type I). The SHG emission is then collimated and spectrally isolated from fundamental light with a filter (**F**, Semrock KFFO1-405/150) and detected with a photomultiplier module (PMT) (**D**, Hamamatsu H7732). For delivery into the microscope, the collinear pair of pulses are next sent into the dispersion management unit.

4.1.3 Dispersion management unit

The dispersion management unit (**DMU**) is implemented for accurate and continuous dispersion management mainly for the dispersion induced by the high N.A. objective and the dichroic beamsplitter in the microscope. The DMU consists of only passive optical components, such as pairs of matched dispersive mirror compressors (**DMC**, Femtolasers GSM209) for coarse adjustment and a pair of thin fused silica wedges (**W**, Femtolasers OA924) for fine adjustment. The DMC simultaneously pre-compensates GDD and TOD within the wavelength range from 630 nm to 1000 nm. For each reflection bounce (-45 ± 10) fs^2 of GDD and $-25 fs^3$ of TOD at 800 nm are introduced [22]. The reflection loss per bounce amounts to 0.4%. Merely the number of reflection bounces off the dispersive mirrors needs to be adjusted for an optimal dispersion pre-compensation. In order to provide negative dispersion up to $-6000 fs^2$, two DMCs have been implemented in series. Fine tuning of GDD within the range from 15 fs^2 to 120 fs^2 is achieved by adjusting the amount of wedge material insertion into the optical path.

4.1.4 Beam management unit

The beam management unit (**BMU**) enables both beam size expansion and polarization control. To minimize the dispersion, an all-reflective beam expander consisting of two focusing mirrors (**FM2 and FM3**, Femtolasers OA056 $f = 150$ mm and OA823 $f = 300$ mm, respectively) are implemented. The beams are expanded and collimated, in order to fill the back aperture of the microscope objective. An ultra-broadband achromatic half waveplate (**HWPI1**, Femtolasers OA232), which is optimized for minimum additional GDD over the entire pulse spectral width, is used to control the orientation of the linear polarized pulse at the position of the sample.

4.1.5 Microscope

The collinear and collimated beams are steered into the microscope unit, which uses a frame of a standard inverted microscope (Olympus IX71). The pulses are reflected by a custom-made dichroic beamsplitter (**BS3**, Femtolasers OA073), which was designed and manufactured to exhibit high reflectance and low GDD in the wavelength range from 600 to 1000 nm and high transmittance in the wavelength range from 300 nm to 580 nm, as shown in fig. 4.3. The pulses are focused into the sample using a microscope objective (**Obj**). Various high N.A. objectives have been used throughout this Ph.D. project, which will be described in detail in the relevant result chapters. If not specified otherwise, an Olympus UPLSAPO IR 60 \times 1.2W objective is used.

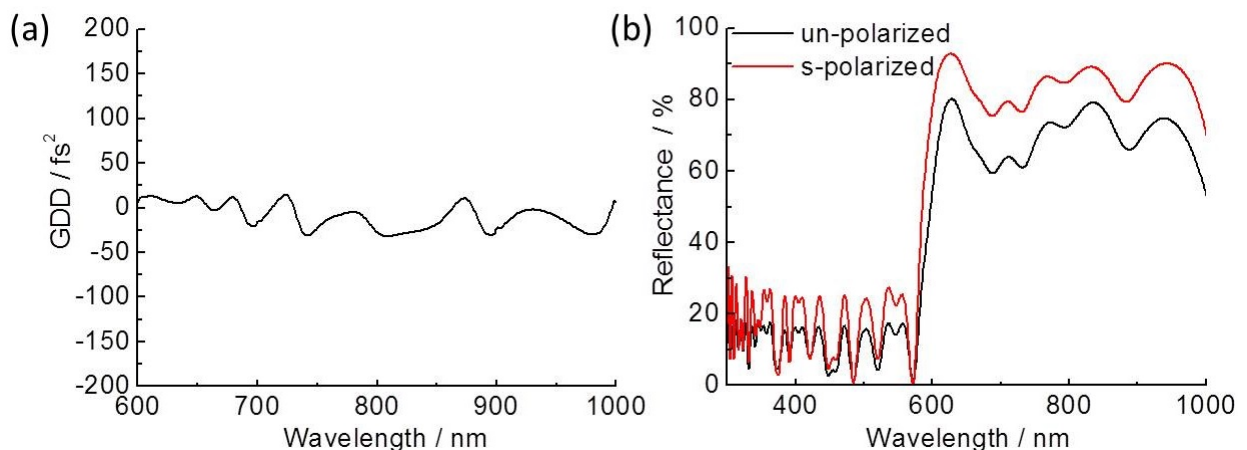


Figure 4.3: Simulated spectral properties of the custom-made dichroic beamsplitter (**BS3**) for NLO microscopy. (a) The GDD spectrum exhibits low values over the entire pulse spectral bandwidth range from 600 to 1000 nm. (b) The reflectance spectrum simulated under 45° incidence for un-polarized and s-polarized light. Simulations were provided by Dr. G. Tempea from Femtolasers Produktion GmbH.

The scattered light that is generated at the focus in the sample is collected either in the forward- or the epi-direction using a lens (**Lens**) or the identical objective used for excitation (**Obj**), respectively. In the forward collection geometry, the scattered light is spectrally isolated from the fundamental laser pulses by the filter (**F**), and then focused by the lens (**L4**) into the detector (**D**) for spectrally integrated detection, or focused by the lens (**L3**) into the spectrometer for spectrally resolved measurements. In the epi-collection geometry, the scattered light is transmitted through the dichroic beam splitter (**BS3**), and either focused by the tube lens (**L4**) into the detector (**D**) for spectrally integrated detection, or going through the telescope (**T2**) and then focused by lens (**L3**) into the entrance slit of the spectrometer (**Spe**) for spectrally resolved measurements. The aperture (**AP**, 0.1 mm diameter) placed inside the telescope (**T2**) is used for suppression of unwanted scattered light from neighboring objects in DF spectroscopy measurements.

For the spectrally resolved detection, the collected light is focused by a plano-convex lens (**L3**, Newport KPX082 $f = 50.2$ mm) into the entrance slit of a Czerny-Turner spectrometer (**Spe**, Acton Research SpectraPro-150) equipped with a back illuminated and liquid nitrogen cooled CCD camera (Princeton Instruments SPEC-10 system). For the spectrally integrated detection, the collected light is focused onto the active area of either a PMT or an avalanche photodiode (**APD**, PerkinElmer SPCM-AQR-15). The current signal from the PMT (Hamamatsu H7732) is pre-amplified by an amplifier (Stanford Research SR570) and consequently acquired by a data acquisition card (National Instruments PCI-6110). For APD detection, single photon detection events are counted either by using a National Instruments NI-6001 or PCI-6110 card.

Sample positioning and imaging are achieved by raster scanning the sample mounted on a closed-loop xyz-piezo-driven scanner (Physik Instrumente P-517.3CL), which has an operating displacement of $100\ \mu\text{m}$ in the x- and y-directions, and $20\ \mu\text{m}$ in the z-direction. Here, the x- and y-axis are defined by the sample plane, which is perpendicular to the optical axis (z-axis). The orientation angle α is defined between the x-axis and the linearly polarized electric field vector of the excitation pulses, see the insert of fig. 4.1.

In order to characterize the laser pulses at different positions along the optical path, the pulse spectrum and average power are monitored. When measuring the laser pulse spectrum, a small part of the laser pulse is collected by a cosine corrector (Thorlabs CCSA2) coupled to a multi-mode fiber (**MMF**, Edmund optics core diameter = $100\ \mu\text{m}$, N.A.= 0.12), which connects to a CCD spectrometer (ASEQ instrument). For measuring the power, two different power meter sensors are used: a thermal power sensor (Thorlabs, S302) and a silicon photodiode (Thorlabs, S120C). The average power measured with the silicon photodiode sensor set to a wavelength of 785 nm was calibrated with the wavelength independent thermal power sensor by simply dividing the former values by 4.8.

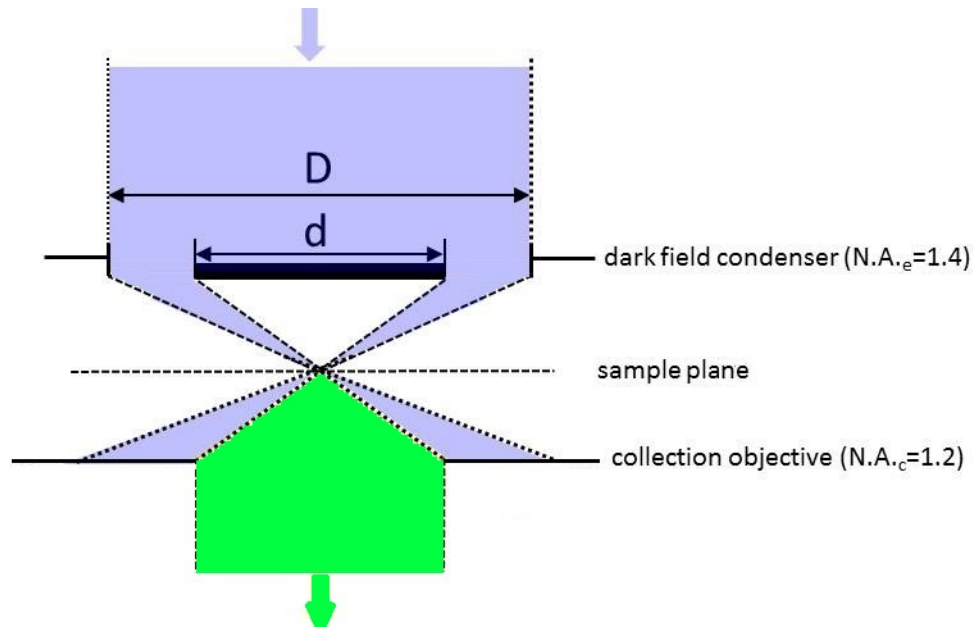


Figure 4.4: Schematic illustration of the dark field (DF) illumination (blue) and the collection microscope objective optical pathways (green) in the home built DF condenser and microscope objective, respectively.

4.1.6 Dark field and transmission microspectroscopy

In order to allow the linear characterization of one and the same metallic nanoparticle that was studied by NLO spectroscopy, dark field (DF) scattering and transmission microspectroscopy are implemented in the same microscope setup. For white light illumination, the output of a 5.4 W halogen lamp (**Lamp**) was coupled into a multi-mode fibre (**MMF**, Thorlabs N.A. = 0.36, core diameter = 400 μm) by using a condenser lens (**L2**, $f = 40$ mm). An achromatic lens (**L1**, Edmund optics $f = 17.5$ mm) was used to couple out and collimate the white light from the fiber. A Glan-Taylor polarizer (**P**, CASIX PGL5010) and a broadband achromatic half-wave plate (**HWP**, Foctech 1312) were used to linearly polarize the white light and control its orientation, respectively. Afterwards, the white light beam size is expanded five times, by using a telescope (**T1**), which consists of two achromatic lenses (Thorlabs $f = 30$ mm and Linos $f = 150$ mm) in order to match the back aperture of the DF condenser. A flippable mirror (**FLM1**, Linos G340523) is used to steer the collimated white light beam along the optical axis of the microscope from the above into the home-built DF condenser (**Lens**), which is replacing the forward-collection objective.

The home-built DF condenser consists of a commercial high N.A. condenser (Leica N.A. = 1.4 oil) that has been modified with a circular field stop of diameter d , blocking the central part of the collimated white light beam. As shown in fig. 4.4, only the residual ring of white light that has not been blocked is focused onto the scattering object. The same objective (**Obj**), which is used for focusing the laser beam, is also used here for collecting the scattered light

from nanoparticles. In order to achieve a high DF scattering image contrast, the size of the incoming white light beam, the size of the field stop, and the N.A. of the collection objective have to be taken into account. For a given clear aperture D , numerical aperture of the excitation condenser $N.A._e$, the numerical aperture of the collection objective $N.A._c$, and the size of field stop d is deduced from eq. 4.1

$$d = D \frac{\sqrt{n^2 - N.A._e^2}}{\sqrt{n^2 - N.A._c^2}}, \quad (4.1)$$

where $N.A._e = n \sin \alpha_e$ and $N.A._c = n \sin \alpha_c$ are the numerical aperture of the condenser and the collection objective, respectively. $n = 1.518$ is the refractive index of the used immersion oil. As defined in fig. 4.4, α_e is the half-angle of the maximum cone of light that excites the object. α_c is the half-angle of the maximum cone of light that enters the collection objective. For the incoming beam size of $D = 28$ mm and $N.A._e = 1.4$ for the oil condenser used, from eq. 4.1 follows that the diameter of the optimized field stop to block the center part of excitation light when using a $N.A._c = 1.2$ collection objective (Olympus UPLSAPO IR 60 \times 1.2 W) is $d = 17$ mm.

After collection by the objective, the DF scattered light is imaged into the entrance slit of the spectrometer as described above in section 4.1.5. For the DF scattering spectrum measurement, the spectral filters (**F**) have been removed and the aperture (**AP**) was placed at the common focus of the telescope (**T2**) in order to reject the DF scattering light from nanoparticles that are not located on the optical axis z . For spectrally integrated DF scattering measurements, using a PMT detector, different spectral regions have been spectrally isolated by using different filters before the detector (**D**).

For transmission microspectroscopy, the DF condenser was replaced by an objective (Zeiss, AchroPlan 40 \times N.A. 0.8 W). No immersion medium was used.

4.2 System control software

There are three software programs needed for control and data acquisition of the different experiments:

1. The commercial software program named WinSpec32 (Roper Scientific) [56], which controls the spectrometer and acquisition parameters of the LN_2 cooled CCD camera, is used to acquire the SHG spectra, fluorescence spectra, DF scattering and transmission spectra. The software provides two data acquisition modes: the imaging mode where the diffraction grating is moved to zero-order diffraction, and the spectroscopy mode where the grating is set to the desired center wavelength.

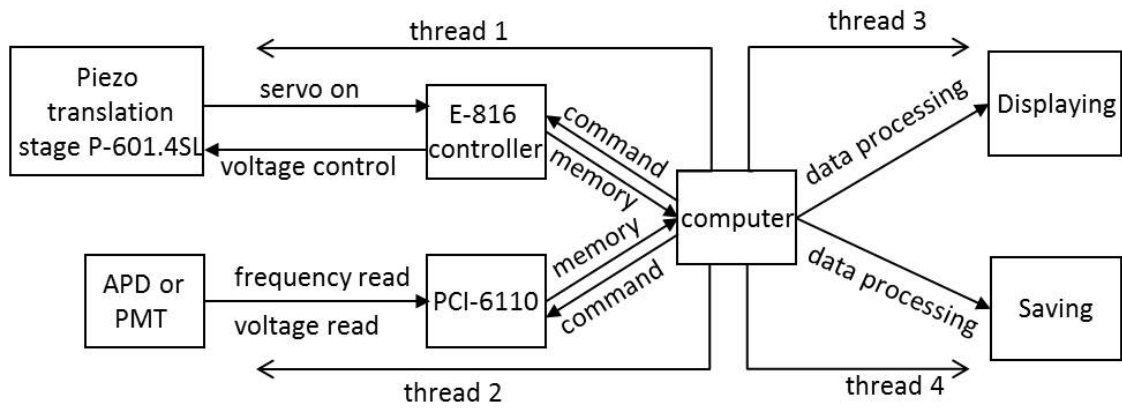


Figure 4.5: Flowchart of control and data acquisition software for the SHG IAC trace measurements.

2. For the image acquisition, which requires the control of the sample position by the xyz piezo scanner and the synchronized readout of the PMT, the APD, and the CCD camera, a home-written software program named ‘Monitor’ in C/C++ by a former group member, Dr. Alexander Kovalev, was used.
3. A new software program for recording SHG IAC trace measurements was written within the course of this Ph.D. project. The core part of this software controls the positioning and scanning of the piezo translation stage delay line of the IA and synchronizes it with the data acquisition using the PMT or APD detectors. The flow chart of this software program is shown in fig. 4.5.

In the following, the home-written software program for recording SHG IAC traces is described in more detail: Based on the Visual studio 2008 development environment, this software program has mainly four functions: piezo translation of the delay line control, data acquisition, data displaying, and saving. The MFC library provided by Microsoft is served as the framework for the software. An advantage of the used C/C++ language is that it can be easily implemented to call compiled controlling interface functions in a third-party dynamic link library (dll). The *nidaq32.dll* for PCI-6110 and *E816_Dll.dll* for the E-816 controller are called in order to define new functions. As shown in fig. 4.5, the multi-thread mechanism is employed to control four different threads, responsible for managing various tasks simultaneously. According to experimental requirements, three different modes are programmed:

1. Start alignment scan

Threads 2 and 3 are used for continuous data acquisition without piezo movement. This mode is used for alignment of the signal collection and detection systems.

2. Start online scan

All four threads are used. The piezo translation stage is continuously moving in thread 1 without reading the actual piezo position. In the meantime, the data acquisition card continuously acquires data from the detector in thread 2. There is no synchronization between these two threads. Thread 3 is responsible for online displaying the recorded SHG IAC trace, which can be saved in thread 4. This ‘Start online scan’ mode is used for the quick evaluation of SHG IAC traces.

3. Start calibrated scan

Here, threads 1 and 2 are synchronized. When data acquisition starts, the piezo translation stage moves one step with a user-specified step size. After the piezo arrives at the set position, this position is read out by the in-built positioning sensor. Then the PCI-6110 card acquires the recorded detector signal amplitude at this piezo position. The data pair of signal amplitude and piezo position is stored into the memory of the computer. After this acquisition, the piezo translation stage starts moving another step, and a new cycle starts. This procedure will stop until the piezo arrives at the user-defined end position of the piezo translation stage. In the meantime, threads 3 and 4 are working for displaying and saving data. The acquisition time for a SHG IAC trace scan with typically 1000 delay steps and an exposure time of 20 ms per step, amounts to approximately 30 s.

The software user interface allows the input of the start position, the end position, the step size for piezo control, the choice of PMT or APD readout, and the exposure time. This software also provides the ASCII format file export. The ASCII file includes three columns for each SHG IAC trace: number of data points, the piezo position in μm , the detector signal in counts and volts for APD and PMT detection, respectively. A configuration file (.ini), which is a simple text file that lists selected control and acquisition parameters, is also saved for each SHG IAC trace measurement. The additional comments and information for the scan can also be recorded in this file. This file can be read by the software function ‘load setting files’, and software configurations are automatically set.

4.3 Data analysis

This section describes the experimental data analysis procedures. Unless otherwise indicated, data analysis are implemented in MATLAB R2012 (MathWorks).

4.3.1 Analysis of SHG IAC trace measurements

1. Raw data processing and normalization

First, the recorded data pairs of piezo position and signal in the SHG IAC trace are sorted according to increasing piezo position and made equidistant. Second, the SHG IAC trace

is subtracted with the dark counts, which was measured independently by blocking the excitation beam. Third, the trace is normalized by the SHG signal, which was recorded when the two pulses are no longer overlapping in time according to eq. 3.37.

2. **Fourier transformation into the frequency domain**

After the piezo position values are converted into time delay values, the SHG IAC trace is Fourier transformed into the frequency domain, and three different frequency components that correspond to the different contributions to the SHG IAC trace at $\pm 2\omega$, $\pm\omega$, and the DC component are numerically separated.

3. **Extraction of the intensity autocorrelation function**

By applying a digital bandpass filter for the DC component (eq. 3.40) and performing an inverse Fourier transformation, the intensity autocorrelation function in the time-domain is extracted according to eq. 3.39.

4. **Extraction of the pulse duration**

The pulse duration is extracted by fitting the experimental intensity autocorrelation function to the corresponding analytical model for a *sech*² (see eq. 3.41). The fitting procedure is implemented by the in-built *lsqcurvefit* MATLAB function.

5. **Extraction of the residual pulse chirp parameters**

The residual GDD and TOD values are extracted by comparing the simulated SHG IAC traces, eqs. 3.36 and 3.37, with the experimental SHG IAC trace.

4.3.2 **Analysis of the excitation pulse spectrum**

1. **Correction for dark counts**

Even when the the CCD chip is not illuminated, the thermal noise, which is frequency independent leads to a an offset signal. This offset has to be subtracted since it does not contain any information concerning the measured pulse spectrum.

2. **Cosmic ray removal**

Some spikes, which are caused by cosmic rays, might show up in the recorded spectra at random spectral positions and times. The median of the neighboring values in the spectrum is used to replace the values detected as cosmic rays.

3. **Correction for the system's spectral sensitivity response**

The processed excitation pulse spectrum needs to be calibrated for the total spectral response of the cosine adapter, the multi-mode fiber, and the CCD spectrometer. The total spectral response is obtained by measuring the transmission spectrum of the combined components by using a calibrated light source (Ocean Optics HL-200-CAL). The corrected excitation pulse spectrum is then obtained by normalizing the measured pulse spectrum with the total transmission spectrum of the system.

4.3.3 Analysis of SHG, TPF, and DF scattering spectra

1. Correction for dark counts

See step 1 in section 4.3.2.

2. Cosmic ray removal

See step 2 in section 4.3.2.

3. Extraction of the DF scattering spectrum

The DF scattering spectrum from an individual metallic nanoparticle is obtained by subtracting the background contribution and then normalizing it by the lamp spectrum. The background contribution originates from residual white light excitation. Here, the background spectrum is independently measured with the identical pixels on the CCD detector from a nearby sample area without nanoparticles present. The lamp spectrum is measured without the field stop in the condenser in an area without nanoparticles present. In order to retrieve the plasmon resonance information of the metallic nanoparticle, the wavelength axis of the DF scattering spectrum $S(\lambda)$ needs to be changed into frequency using the transform function $S(\omega) = S(\lambda)\lambda^2/2\pi c$. Then, the spectrum is fitted to a Lorentzian function, which is the square of the scattering electric field amplitude $|\tilde{E}(\omega)|$ in eq. 3.60 to determine the FWHM linewidth $\Delta\omega$ and the resonance frequency Ω .

4. Extraction of SHG and TPF spectrum

The SHG and the two-photon induced fluorescence (TPF) spectra from an individual nanoparticle are obtained by first subtracting a background contribution, which originates from weak SHG at the interface between the coverslip glass and the immersion oil or from autofluorescence of the sample. Here the background spectrum is independently measured with the identical pixels on the CCD detector from a nearby sample area without nanoparticles present. For separating the SHG and TPF spectral contributions, which are simultaneously generated in a nanoparticle and spectrally overlapped, the pure TPF reference spectrum is independently obtained from a specific nanoparticle that does not

exhibit SHG, but only TPF. This pure TPF spectrum is then used for weighted subtraction from the background corrected spectrum of the nanoparticle, where TPF intensity is scaled to the intensity at the frequencies where only TPF components exist. For the extracted SHG spectrum, the center wavelength is determined by its center of mass. Finally, the extracted SHG spectrum is normalized with the total spectral sensitivity response of the detection system, which mainly includes the spectral response of filters, the grating, and the camera CCD chip used, which are obtained from the manufacturer's specification.

4.3.4 Polar plot analysis of SHG, TPF, DF scattering, and transmission signals

1. Correction for dark counts

For polarization resolved SHG, TPF, DF scattering, and transmission measurements, the dark counts of the APD and the PMT detectors, which are recorded independently by blocking the excitation beam, are subtracted.

2. Correction for background contributions

For the DF scattering and SHG measurements, here the corresponding background contributions are measured and subtracted for each polarization excitation, as introduced in step 3 and step 4 in section 4.3.3, respectively.

3. Correction for system's polarization response

For polarization-resolved SHG and TPF experiments, corrections for the depolarization of the linearly polarized excitation pulses by the different optical elements in the optical pathway, such as the dichroic beamsplitter (BS3) and the high N.A. microscope objective (Obj), are measured for each input polarization angle of the linearly polarized excitation beam. Here, the intensity of the isotropic TPF from an aqueous solution of Rhodamin 6G was measured. The corrected SHG polar plot is then obtained by normalizing the background corrected SHG intensity with the TPF intensity of Rhodamin 6G for each polarization angle.

For the DF scattering experiment, the polarization dependence of the optical components inside the white light beam and detection pathway was measured in a sample area without nanoparticles present and when the field stop was removed. The DF scattering polar plot is then obtained by normalizing the background corrected DF scattering intensity with the white light intensity for each polarization angle.

For the transmission experiment, the polarization dependence of the optical components inside the white light beam and detection pathway was measured in a blank coverslip sample. The transmission polar plot is then obtained by normalizing the recorded transmitted

white light intensity through the sample with that transmitted through a blank coverslip sample for each polarization angle.

4. **Calibrating the polar angle to the sample coordinate system**

Two curves are needed to calibrate the angle in the recorded polar plots to the sample coordinate system.

For the calibration of the DF scattering and transmission polar plots, an analyzer oriented parallel to the x-axis was placed in the sample plane. The white light beam intensity transmitted through the analyzer as a function of the polarization angle, which was adjusted by a half waveplate (HWP2), was measured by a power meter (Thorlabs, S120C). The polarization angle, which corresponds to maximum intensity, is defined as the 0° in the x-y sample coordinate system.

For the calibration of the SHG polar plots, the same analyzer oriented parallel to the x-axis was placed in the sample plane. Here, the laser beam intensity transmitted through the analyzer as a function of the polarization angle, which was adjusted by a half waveplate (HWP1) was measured by the same power meter. The polarization angle, which corresponds to maximum intensity, is defined as the 0° in the x-y sample coordinate system.

5 Diffraction-limited focusing of few-cycle laser pulses

Many applications of NLO microscopy benefit from the availability of few-cycle laser pulses at the focus of a high N.A. objective. Apart from enhancing the signal generation efficiency in NLO microscopy, diffraction-limited focusing of few-cycle pulses might pave the way for fundamental studies of ultrafast phenomena with a sub-micron spatial resolution. As theoretically described in chapter 3, the propagation of an ultrashort pulse in optical materials, particularly in the glass of a high N.A. microscope objective, results in spatial and temporal distortions of the pulse electric field, which can severely affect its quality in the focus. In this chapter, we demonstrate the experimental achievement of in-focus diffraction-limited few-cycle pulses by using high N.A. objectives and purely passive GDD and TOD dispersion management. We also experimentally characterize the spatial properties of the focus and the properties of in-focus pulses in both frequency and time domains. In particular, the dependence of SHG intensity on the in-focus pulse duration of the few-cycle pulse and the back-aperture of the focusing high N.A. microscope objectives are investigated. Finally, nonlinear optical image contrast enhancement and microspectroscopy in both the frequency- and time-domains by using in-focus few-cycle pulses are demonstrated for the SHG of single collagen fibrils.

5.1 Materials and methods

5.1.1 NLO microscope configurations

Because different experiments are discussed in this chapter, their different configurations of the NLO microscope used for the detection geometry, filters, and detectors are listed in table 5.1.

5.1.2 Preparation of collagen fibril samples

The steps to prepare a sample of self-assembled collagen fibrils on a glass coverslip are listed below:

Table 5.1: The NLO microscope configurations for the detection geometry, filters, and detectors used for the different experiments discussed in this chapter.

section	experiment	detection geometry	filters	detector
5.2	SHG imaging of a gold nanoparticle	Epi	band-pass filter (Semrock, KFF01 405 nm / 150 nm) and short-pass filter (Omega 450 nm)	APD
5.2	TPF z-profile measurement	Epi	band-pass filter (Chroma, HQ 585 nm / 80 nm)	Spectrometer
5.3.1	SHG spectrum of KDP crystal	Epi	band-pass filter (Semrock, KFF01 405 nm / 150 nm) and short-pass filter (Omega 450 nm)	Spectrometer
5.3.1	SHG intensity power dependence of KDP crystal	Epi	band-pass filter (Semrock, KFF01 405 nm / 150 nm) and short-pass filter (Omega 450 nm) and BG3 (Thorlabs, FGB25)	PMT
5.3.2 5.4.1	SHG IAC trace measurements	Forward	band-pass filter (Semrock, KFF01 405 nm / 150 nm) and short-pass filter (Omega 450 nm) and BG3 (Thorlabs, FGB25)	PMT
5.4.2.2	SHG imaging of collagen fibrils	Forward	band-pass filter (Semrock, KFF01 405 nm / 150 nm) and short-pass filter (Omega 450 nm)	APD
5.4.2.3	SHG spectra of collagen fibrils	Forward, Epi	band-pass filter (Semrock, KFF01 405 nm / 150 nm)	Spectrometer
5.4.2.3	SHG IAC trace measurements on collagen fibrils	Forward, Epi	band-pass filter (Semrock, KFF01 405 nm / 150 nm) and short-pass filter (Omega 450 nm)	APD

1. Dilute 667 μl collagen stock solution (Invitrogen, A1048301, 3 mg/ml, type I collagen, rat tail) in 1 ml millipore H_2O and 220 μl Tris / HCl 100 mM buffer.
2. Adjust the pH value of the diluted solution to neutral pH = 7 by using NaOH and HCl.
3. Let the collagen fibrils grow in the solution at room temperature for 24 hours.
4. Drop 10 μl solution on a coverslip (Carl Roth GmbH, $24 \times 32 \text{ mm}^2$, #1) and leave it on the coverslip for 10 minutes.
5. Rinse the glass coverslip with PBS buffer (PBS: 16.1 mM $Na_2H_2PO_4$, 3.9 mM NaH_2PO_4 , and 1.25 mM NaCl) three times and then with millipore water three times in order to clean its surface from salt crystals.
6. Let the sample dry at room temperature for 1 h.
7. Drop 150 μl millipore water on the sample area and make a sandwich of the sample coverslip with another glass coverslip by using a spacer (double-sided tesa film mask, thickness 80 μm), so that the collagen fibrils can be measured in aqueous environment between two optical windows.

5.1.3 AFM imaging of collagen fibrils

Before the NLO microscopy measurements, the type I collagen fibrils are characterized by atomic force microscopy (AFM). Measurements are carried out using the AC mode on a AFM microscope (WITec alpha300 RA). For the experiments, the sample resulting from step 6 in section 5.1.2 is used. For the size detection, the topography and phase images of collagen fibrils with an integration time of 0.625 ms / pixel are recorded.

5.2 NLO characterization of the diffraction-limited focus dimensions

In order to achieve a diffraction-limited focus, the collimated laser beam has to fill the back aperture of the high N.A. microscope objective. The diameter of the clear apertures of the used Olympus UPLSAPO 60× N.A. 1.2W IR and Zeiss AchroPlan 40× 0.8W microscope objectives are 8.2 mm and 10.4 mm, respectively.

The beam diameter before entering into these objectives is determined to be (11.0 ± 0.3) mm by using the knife-edge technique, as defined by the full width at $1/e$ of the maximum of the laser beam intensity profile.

The SHG signal of a single spherical gold nanoparticle with a diameter of 125 nm (Nanopartz A11-125) placed in immersion oil (Olympus, Type-F, $n = 1.518$) on the coverslip (Carl Roth GmbH, 24 mm × 32 mm, #1) is used to characterize the in-focus lateral dimensions. Fig. 5.1 shows an SHG image of this nanoparticle in the x - y plane when the Olympus UPLSAPO 60× N.A. 1.2W IR microscope objective is used. The lateral SHG intensity profile across the nanoparticle has a FWHM = (310 ± 10) nm. This corresponds to a two-photon excitation volume with a lateral $1/e$ radius of w_{xy} (186 ± 6) nm, which is larger than the theoretical value of 160 nm predicated by eq. 3.28 for an NA = 1.2 and $\lambda = 820$ nm. This indicates that a diffraction-limited focus of a few-cycle laser pulse was achieved for an effective NA slightly smaller than 1.2, which is the consequence of the fact that the back-aperture of the objective is not homogeneously filled by the collimated Gaussian beam [26].

For the characterization of the experimentally achieved spatial resolution along the z -axis, the two-photon induced fluorescence (TPF) intensity of an aqueous solution of Rhodamine 6G (Lambdachrome, 5900) on a glass coverslip (Carl Roth GmbH, 24 mm × 32 mm, #1) is measured when the few-cycle pulses are focused along the z -axis direction through the glass-solution interface ($z = 0$) with an Olympus UPLSAPO 60× N.A. 1.2W IR microscope objective. The corresponding z -profile is shown in fig. 5.2 (a). The derivative of this intensity profile, shown in fig. 5.2 (b), has a FWHM = (1.3 ± 0.1) μm . This corresponds to a two-photon excitation volume with a longitudinal $1/e$ radius of w_z (0.78 ± 0.06) μm , which is larger than

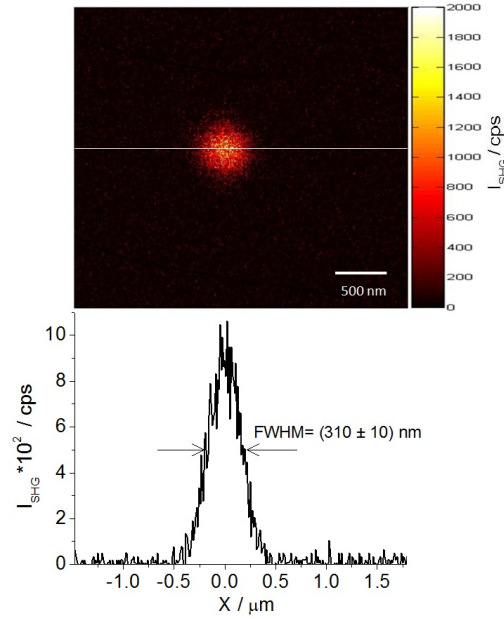


Figure 5.1: An SHG image in the x-y plane of a single 125 nm spherical gold nanoparticle with a measured lateral SHG intensity profile of $\text{FWHM} = (310 \pm 10) \text{ nm}$, which indicates the diffraction-limited focusing of the few-cycle pulses with an Olympus UPLSAPO 60 \times N.A. 1.2W IR microscope objective.

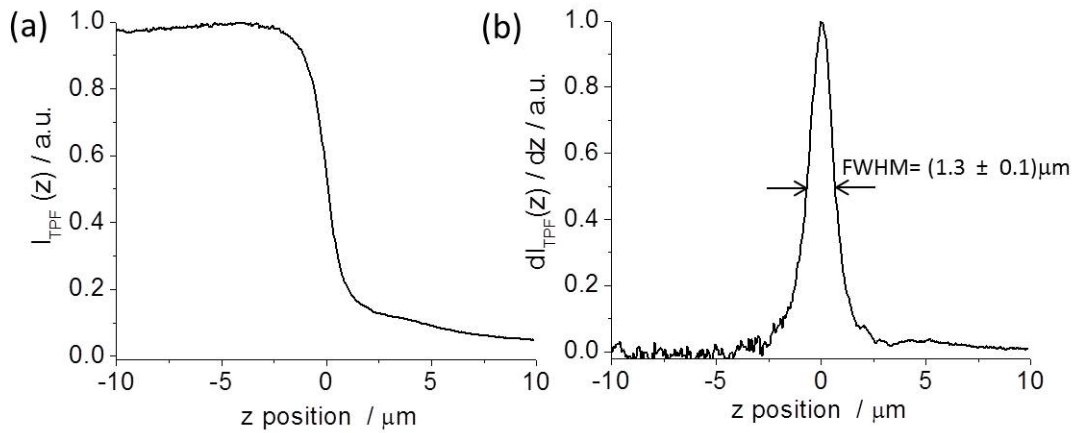


Figure 5.2: (a) z-profile of the measured TPF intensity when focusing the few-cycle pulses through the glass-dye solution interface ($z = 0$) with the Olympus UPLSAPO 60 \times N.A. 1.2W IR microscope objective. (b) Derivative of the profile shown in (a) with a measured $\text{FWHM} = (1.3 \pm 0.1) \mu\text{m}$.

the theoretical value of $0.52 \mu\text{m}$ predicated by eq. 3.29 for an $\text{NA} = 1.2$ and $\lambda = 820 \text{ nm}$. This is also the consequence of the fact that the back-aperture of the objective is not homogeneously filled by the collimated Gaussian beam [26].

5.3 SHG characterization of in-focus pulse properties

5.3.1 The measured SHG spectrum in KDP

First, the SHG intensity generated in a thick KDP crystal (type-I) was measured as a function of average excitation laser power at the sample. Here, the Olympus UPLSAPO 60× N.A. 1.2W IR microscope objective and the best dispersion compensation was used. As shown in the log-log plot in fig. 5.3 (a), the slope of the linear fit (red curve) to this experimental data (black squares) amounts to (1.93 ± 0.08) mV / mW, which confirms that the SHG intensity has a quadratic dependence on the average excitation laser power in accordance with eq. 3.26. Next, the SHG spectrum, black curve shown in fig. 5.3 (b), was obtained when focused into the KDP crystal with an average excitation laser power of $900 \mu\text{W}$ at the sample and a pulse duration of 7.3 fs. For comparison, the simulated SHG spectrum (blue curve), which is obtained from eq. 3.31 using the in-focus laser pulse spectrum and the residual dispersion values of $\text{GDD} = 0 \text{ fs}^2$ and $\text{TOD} = 170 \text{ fs}^3$ (see fig. 5.5 (b) in section 5.3.2.1), is also shown. This is in good agreement with the experimental SHG spectrum. The mismatch between the experimental spectrum and the corresponding simulation of an SHG spectrum for excitation with a Fourier-transform limited pulse (red curve: $\text{GDD} = 0 \text{ fs}^2$ and $\text{TOD} = 0 \text{ fs}^3$) reveals that the residual third-order dispersion in our experiment has a significant narrowing effect on the in-focus SHG spectrum.

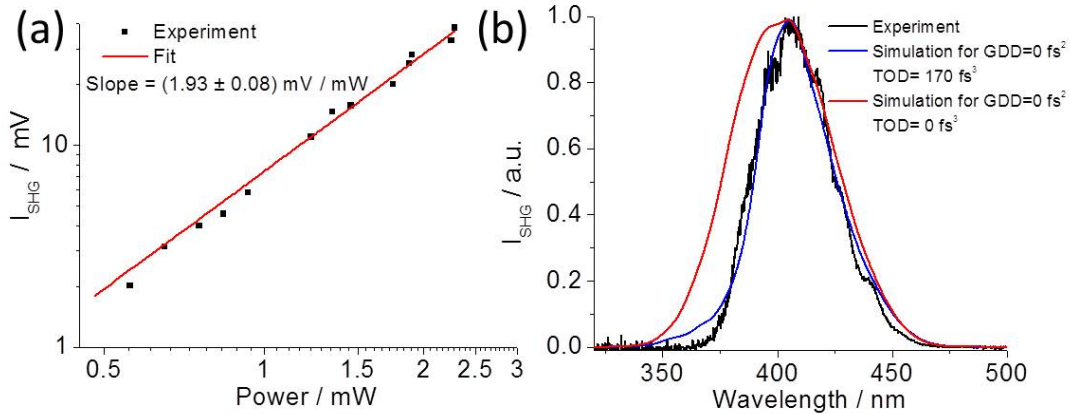


Figure 5.3: (a) Log-log plot of SHG intensity versus the average excitation laser power when 7.3 fs pulses are focused into a thick KDP crystal with an Olympus UPLSAPO 60× N.A. 1.2W IR microscope objective and the best dispersion compensation. The linear fit to the experimental data (squares) has a slope of (1.93 ± 0.08) mV / mW. (b) Corresponding SHG spectrum (black curve) recorded with an average excitation power of $900 \mu\text{W}$. Simulated spectra for residual dispersion values of $\text{GDD} = 0 \text{ fs}^2$ and $\text{TOD} = 170 \text{ fs}^3$ (blue curve) and for $\text{GDD} = 0 \text{ fs}^2$ and $\text{TOD} = 0 \text{ fs}^3$ (red curve) according to eq. 3.31.

5.3.2 SHG interferometric autocorrelation trace measurements

5.3.2.1 In-focus pulse duration dependence on the N.A. of the focusing objective

A conventional high N.A. microscope objective is an assembly of glass lenses with a total thickness of several centimeters. Therefore, it introduces a large amount of material dispersion, which easily distorts a few-cycle pulse in its focus. Hence, the pre-compensation of the dispersion introduced by the high N.A. objective is critical to obtain tightly focused Fourier-limited few-cycle pulses.

In this section, we will experimentally demonstrate pre-compensation by using purely passive GDD and TOD dispersion management. SHG interferometric autocorrelation (SHG IAC) traces are recorded to characterize the few-cycle pulses when focused into frequency-doubling KDP or BBO crystals. Fig. 5.4 shows an example for an experimental SHG IAC trace (black dots) when the few-cycle pulses are focused with an Olympus UPLSAPO 60× N.A. 1.2W IR microscope objective with incomplete pre-compensation. One observes that the central peak portion of the SHG IAC trace is seated on a hung bump baseline, which indicates that the pulse energy is distributed over a much broader temporal range than the original pulse. The SHG IAC trace simulated according to eqs. 3.36 and 3.37 (red curve) using the in-focus pulse spectrum and residual dispersion values of $GDD = 90 \text{ fs}^2$ and $TOD = 185 \text{ fs}^3$, also shown in fig. 5.4, fits the experimental SHG IAC trace nicely. This amount of GDD dispersion corresponds to the maximum of experimentally induced dispersion that can be pre-compensated by the full insertion of the pair of glass wedges (**W**) into the optical beam path (see fig. 4.1). Hence, fine-tuning of GDD up to a limit of 90 fs^2 is achieved by the wedges, whereas for more dispersion pre-compensation, the number of bounces on the DMC needs to be changed. Using eqs. 3.39 to 3.41, the pulse duration is determined to be 36.8 fs ($sech^2$), which is approximately five times longer than the oscillator output laser pulse.

It is also worthy noticing that the spectral modulation and dispersion introduced by any optical component in the optical path to the microscope objective, such as dichroic filters, mirrors, beamsplitters, and the half-waveplate, are also critical to achieve in-focus few-cycle pulses near their Fourier limit. Special care was taken to use low-GDD optics that support the entire spectral bandwidth of the oscillator output pulse. Especially, a customized dichroic beam splitter (BS3) was implemented that exhibits low-GDD values from 600 to 1000 nm (see fig. 4.3 (a)). The few-cycle NLO microscope system equipped with customized optics, as described in chapter 4, enables the delivery of near-bandwidth limited 7-fs pulses at the foci of common microscope objectives with the N.A. ranging from 0.5 to 1.2. Routinely, SHG IAC traces with clean temporal profiles are obtained by adjusting the appropriate number of bounces of the pulses on the DMCs and by fine-tuning the insertion of the thin wedges into the laser beam. This is shown in fig. 5.5 (a) and (b) where SHG IAC traces (black dots) measured with the lowest N.A. objec-

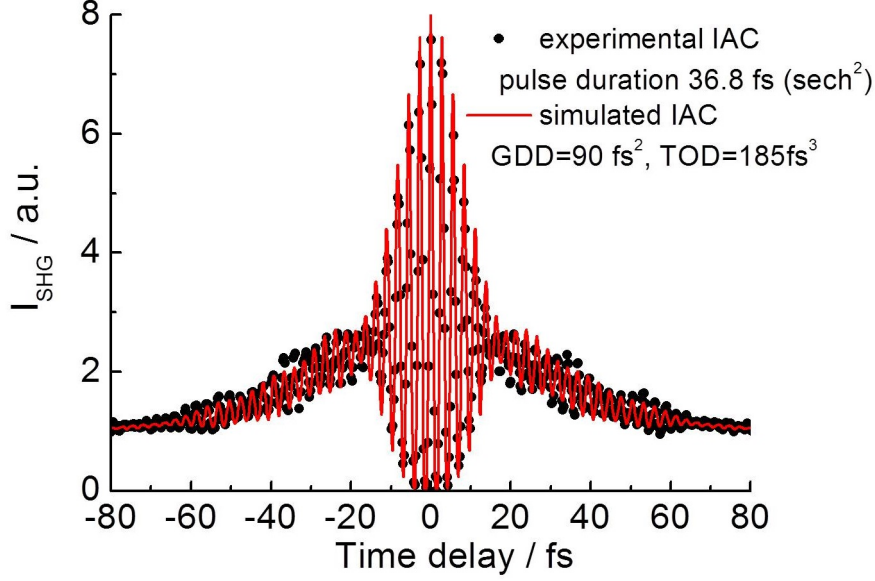


Figure 5.4: Example of measured (black dots) and simulated (red line) SHG IAC traces of in-focus pulses with a duration of 36.8 fs ($sech^2$) that result from incomplete dispersion pre-compensation. Best agreement with the experiment is obtained for the simulation that uses the in-focus pulse spectrum and residual values of $GDD = 90 fs^2$ and $TOD = 185 fs^3$.

tive (Olympus UMPLFL 20× N.A. 0.5W) and the highest N.A. objective (UPLSAPO 60× N.A. 1.2W IR), respectively, are displayed. The simulated SHG IAC traces (red curves) using eqs. 3.36 and 3.37 and the measured in-focus pulse spectrum (see fig. 5.10 (a)) with residual dispersion values of $GDD = 0 fs^2$ and $TOD = 110 fs^3$ and of $GDD = 0 fs^2$ and $TOD = 170 fs^3$ are shown in 5.5 (a) and (b), respectively. They describe the experimental data, even reproducing the small oscillation structures at the time delays of about ± 10 fs. From fits to eqs. 3.39 to 3.41 the in-focus pulse duration for focusing with the Olympus UMPLFL 20× N.A. 0.5W and the UPLSAPO 60× N.A. 1.2W IR objectives were determined to be $(6.6 \pm 0.3) fs (sech^2)$ and $(7.3 \pm 0.3) fs (sech^2)$, respectively, which are slightly longer than the original oscillator output pulse of $(6.4 \pm 0.3) fs (sech^2)$ (see fig. 4.2 (b)).

The total values of compensated GDD, TOD, and in-focus pulse durations, obtained under conditions of best dispersion management are listed in table 5.2 for different N.A.s of commonly used objectives. Here, the specific GDD and TOD values that have to be compensated for each microscope objective have been estimated according to the number of the reflection bounces on the DMCs, the amount of wedge glass inserted, and the optical path lengths in air, immersion water, and the glass coverslip. There is an accumulated uncertainty for GDD values, which accounts for the errors specified for the optical components by the manufacturer and for the uncertainties of the dispersion values and the optical path length measurements in air, glass wedges, immersion water, and the glass coverslip. Details for the estimation of the microscope objective dispersion values can be found in appendix A.1. From the error analysis presented

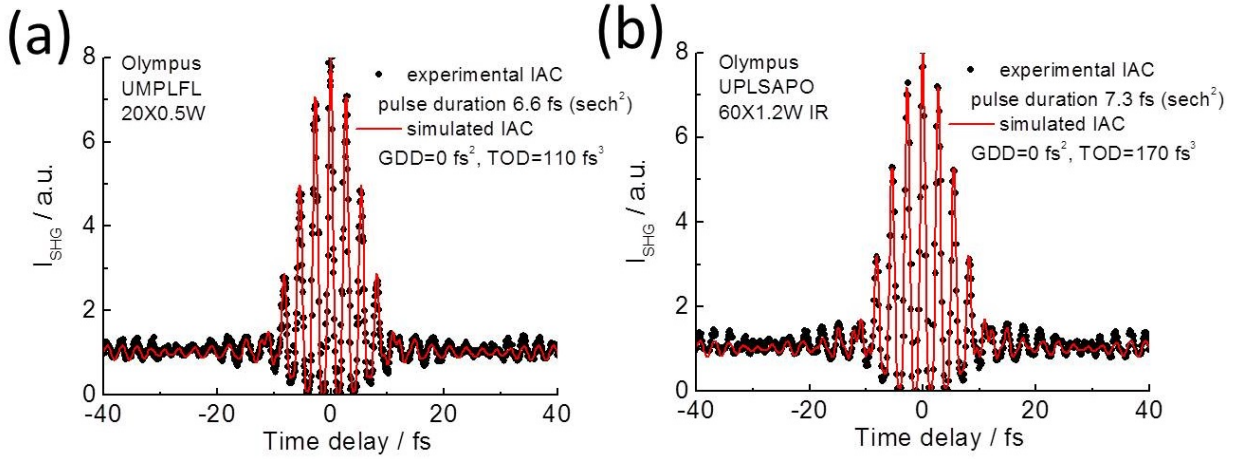


Figure 5.5: The experimental (black dots) and simulated (red lines) SHG IAC traces of in-focus pulses with durations of (6.6 ± 0.3) fs ($sech^2$) and (7.3 ± 0.3) fs ($sech^2$) and residual dispersion of $GDD = 0$ fs^2 and $TOD = 110$ fs^3 and of $GDD = 0$ fs^2 and $TOD = 170$ fs^3 for (a) an Olympus UMPLFL 20× N.A. 0.5W objective and (b) an Olympus UPLSAPO 60 × N.A. 1.2W IR objective, respectively.

in appendix A.1, we conclude that the GDD error introduced by the DMCs accounts almost completely for the relative error of approximately 20% of the total compensated GDD listed in table 5.2. Since the manufacturer does not specify any errors for TOD values of the used optical components, and the uncertainties of TOD in air, water, and glass coverslip due to the errors made in increasing the respective optical path length are negligible, no uncertainties for complete TOD values are estimated. Not more than approximately 1% of the total TOD is attributed to the glass wedges. However, the unknown error of TOD for the DMCs is expected to be much larger.

Table 5.2: Retrieved in-focus pulse durations with pre-compensated GDD and TOD values for a series of microscope objectives with increasing N.A. and residual GDD and TOD values extracted from simulations.

Microscope Objective	N.A.	Compensated dispersion for objective		In-focus pulse duration / fs ($sech^2$)	Residual dispersion	
		GDD / fs^2	TOD / fs^3		GDD / fs^2	TOD / fs^3
Olympus UMPlanFL N 20X NA 0.5W	0.5	1810 ± 400	710	6.6 ± 0.3	0	110
Zeiss ACHROPLAN 40X NA 0.8W	0.8	1810 ± 400	710	6.8 ± 0.3	0	110
Olympus LUMPlanFI 60X NA 0.9 W IR	0.9	2280 ± 500	960	7.0 ± 0.3	0	120
Olympus UPlanSApo 60X NA 1.2W IR	1.2	2350 ± 480	1040	7.3 ± 0.3	0	170

The input pulse durations, residual GDD and TOD values have been extracted from those SHG IAC trace simulations (see eqs. 3.36 and 3.37) that used a measured in-focus pulse spectrum and best fit the experimental SHG IAC traces. The error given for the pulse duration accounts for the standard deviation of at least five independent SHG IAC trace measurements. Besides providing estimates for GDD and TOD values of common microscope objectives, the following conclusions can be drawn from table 5.2.

1. For high-N.A. objectives with $N.A. \geq 0.9$, the amounts of GDD and TOD that need to be pre-compensated inside the microscope objective in order to achieve in-focus near Fourier-limited pulses is higher than for objectives with lower N.A.s. This observation simply reflects the expected increase in the number of optical components and the optical path length through the dispersive glass inside a high-N.A. microscope objective.
2. The observed increase in the in-focus pulse duration from (6.6 ± 0.3) fs ($sech^2$) at $N.A. = 0.5$ to (7.3 ± 0.3) fs ($sech^2$) at $N.A. = 1.2$ (see fig. 5.5) is attributed to the increased residual TOD and higher-order dispersions, which could not be pre-compensated in our setup. In contrast, the residual GDD was found to be negligible, which indicates complete GDD pre-compensation for all objectives studied.

5.3.2.2 In-focus pulse duration dependence on the back-aperture of the focusing objective

When few-cycle pulses pass through a focusing objective, their temporal distortion in the diffraction-limited focus can be caused by three different effects [57]: (1) material dispersion (GDD, TOD, and higher-order dispersion), (2) chromatic aberrations, and (3) spherical aberrations.

The effect of material dispersion and its pre-compensation have been discussed in the previous section. In this section, we will discuss the chromatic and spherical aberrations in high-N.A. microscope objectives, which can deteriorate both the focal volume and the pulse duration [58]. For the assumption that the spherical aberration is small, such that all rays are in focus in the paraxial focal region of the objective, the temporal pulse distortion is expressed by the radially varying group delay [59]

$$GD(r) = -Ar^2 + Br^4 + Cr^2, \quad (5.1)$$

where $r \in [0, 1]$ is the radius normalized to that of the entrance pupil of the microscope objective. The first term represents the effect of chromatic aberration, which is equivalent to the radius-dependent arrival time between the pulse front and its phase front (propagation time delay–PTD effect). Here, A is given by [57]

$$A = \frac{\lambda_o}{2c} \left(\frac{NA^2}{1 - NA^2} \right) \frac{df}{d\lambda}, \quad (5.2)$$

where λ_o is the center wavelength of the laser pulse, c is the velocity of light, NA is the numerical aperture of the objective, and $\frac{df}{d\lambda}$ is its chromatic aberration at λ_o . For a commonly used, high-quality, aberration-corrected microscope objective with a high N.A. such as for example an UPLSAPO 100× Oil objective, the chromatic aberration at $\lambda_o = 820$ nm is specified by the manufacturer to $\frac{df}{d\lambda} \approx 1$ [60]. According to eq. 5.2, this results in $A = 4.1 \times 10^{-17}$. Consequently, the maximum group delay due to chromatic aberration can be neglected. For the Olympus UPLSAPO 60× N.A. 1.2W IR microscope objective with similar good correction for aberrations, which is used in our experiments, the impact of chromatic aberrations is also assumed to be negligible.

The second term originates from spherical aberration. Because the spatial focus dimensions have been observed to be close to the diffraction-limited focus size expected by theory (see eq. 3.28 and the experimental result shown in fig. 5.1), the impact of spherical aberration on the temporal pulse distortion is also expected to be negligible ($B \approx 0$).

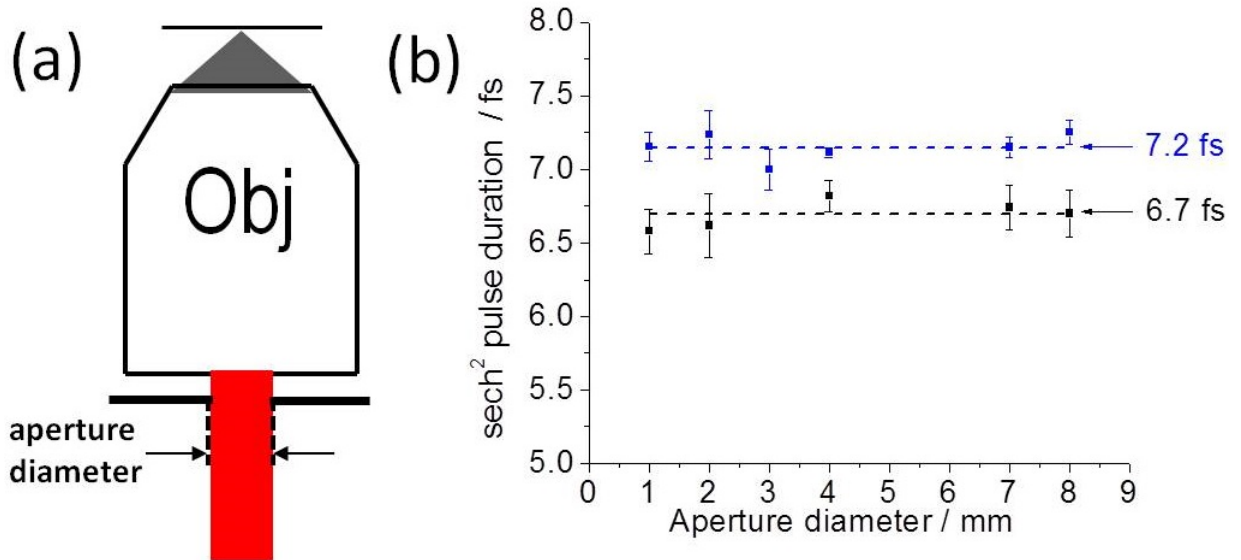


Figure 5.6: Experiments for testing the radially varying GD effect of the in-focus few-cycle pulses. (a) Schematic illustration of the microscope objective (Obj) with an additional iris for adjusting the diameter of its back-aperture. (b) Retrieved pulse duration dependence on the aperture diameter for the Zeiss ACHROPLAN 40× N.A. 0.8W (black squares) and the Olympus UPlanSApo 60× N.A. 1.2W IR (blue squares).

The third term is due to a delay relative to the paraxial focus plane [59]. Within the accuracy of measuring the longitudinal dimension of our focus (see fig. 5.2), there is no experimental evidence for an aberration that causes focusing outside the paraxial focal plane. Therefore, we assume that the third term in eq. 5.1 also vanishes.

The effect of $GD(r)$ on the in-focus pulse duration has been tested by experiments, where SHG IAC traces were measured as a function of the back-aperture diameter for two focusing

objectives (Zeiss ACHROPLAN 40× N.A. 0.8W and Olympus UPlanSApo 60× N.A. 1.2W IR), see fig. 5.6. For the Zeiss objective, the pulse duration extracted by using eqs. 3.36 to 3.41, was observed to be independent of the back-aperture diameter at a constant value of (6.7 ± 0.3) fs (*sech*²). Similarly, the extracted pulse duration was observed to be constant at (7.2 ± 0.3) fs (*sech*²) when varying the back-aperture diameter of the Olympus objective. Ideally, in order to directly measure the GD effect of a high-N.A. objective, interferometry experiments need to be implemented [61–63]. However, in practice, where diffraction-limited focusing with a high-N.A. objective and a beam fully filling its back aperture are used, our experimental results shown in fig. 5.6 (b) provided no evidence for significant temporal distortion when compared to paraxial focusing.

In summary, by using high-quality microscope objectives that are both chromatically and spherically aberration-corrected in the near-infrared wavelength range, as used throughout our experiments, additional in-focus pulse distortions other than caused by material dispersion are not theoretically expected and also experimentally confirmed to be negligible.

5.4 Application for enhancement of NLO imaging contrast

5.4.1 Dependence of SHG intensity on pulse duration

According to eq. 3.26, the SHG intensity is expected to be inversely proportional to the pulse duration when the average power and repetition rate of the excitation laser pulse train are kept constant. For a clear experimental test of this relationship, the SHG intensity is measured as a function of GDD when the few-cycle pulses are focused about 1 μm into a thick KDP crystal (type-I) with an Olympus UPLSAPO 60× N.A. 1.2W IR microscope objective. Here, the GDD is adjusted by tuning the optical path length of the thin wedges (W). The SHG IAC trace is measured for each GDD value, and the pulse duration is extracted from the corresponding intensity autocorrelation function according to eqs. 3.39 to 3.41. As shown in fig. 5.7 (a), with increasing GDD from 0 to 87 fs^2 , the extracted pulse duration is increased from 7.1 fs to 36.8 fs, and the SHG intensity decreases by approximately one order of magnitude. In the log-log plot shown in fig. 5.7 (b), the same data are used to plot the measured SHG intensity versus the extracted pulse duration (black dots). The linear fit (red curve) to the data results in a slope of $-(1.05 \pm 0.03) \text{fs}^{-1}$, which agrees well with the inverse proportionality predicted by theory (see eq. 3.26). To our best knowledge, this result is the first demonstration of the inverse linear dependence of SHG intensity on pulse duration down to 7.1 fs. A previous literature report experimentally confirmed this relationship down to 20 fs only [64].

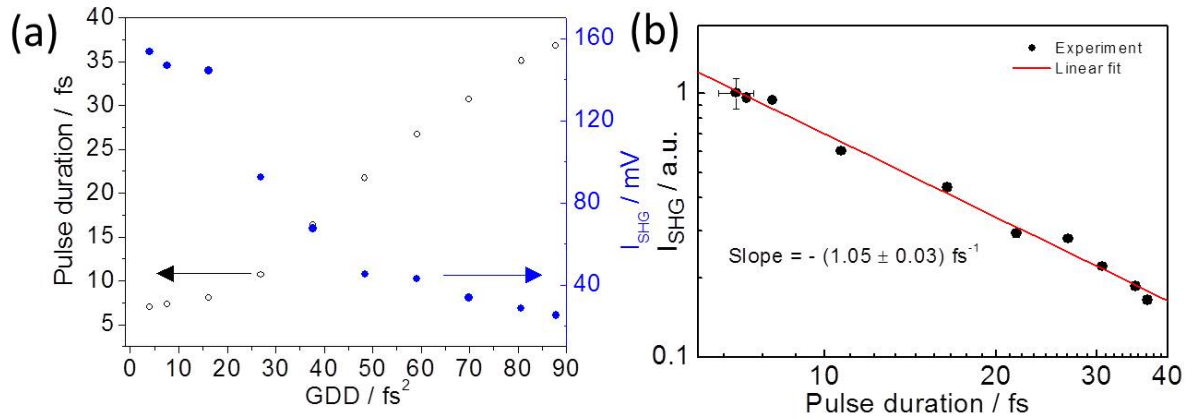


Figure 5.7: Experimental confirmation of the inverse linear dependence of SHG intensity on pulse duration down to 7.1 fs. (a) Measured SHG intensity (blue dots) when focused into a KDP crystal with an Olympus UPLSAPO 60× N.A. 1.2W IR microscope objective and in-focus pulse duration (black empty circles) extracted from SHG IAC traces versus GDD values controlled by the insertion of the thin wedges. (b) Log-log plot of the SHG intensity as a function of pulse duration (black dots). The linear fit (red curve) has a slope of $-(1.05 \pm 0.03) \text{ fs}^{-1}$.

5.4.2 SHG image contrast enhancement and microspectroscopy of single collagen fibrils

5.4.2.1 Motivation

NLO microscopy offers a powerful tool for label-free tissue imaging at the sub-cellular level, as it can provide morphological and functional information without the need for exogenous markers. Collagen is the most abundant protein in the extracellular matrix (ECM) [65]. It helps to maintain the integrity of many tissues via its interactions with cell surfaces and other ECM molecules. Type-I collagen forms fibrils with diameters of hundreds of nanometers, which have a natural noncentrosymmetric, highly crystalline triple helix structure [66] [67]. Hence, the structure of collagen fibrils allows their intrinsic SHG. We demonstrate the SHG imaging contrast enhancement and microspectroscopy based on individual collagen fibrils in both the time- and the frequency-domains.

Before performing the NLO microscopy measurements, AFM imaging was performed in order to confirm that individual collagen fibrils have been self-assembled into their native structure and not denatured at the surface of the glass coverslip. Fig. 5.8 (a) shows an AFM phase image of typical self-assembled collagen (type-I) fibrils, which was measured by a former group member, Johanna Konrad [68].

Fig. 5.8 (b) shows the topographical height profile along the red line across the single fibril

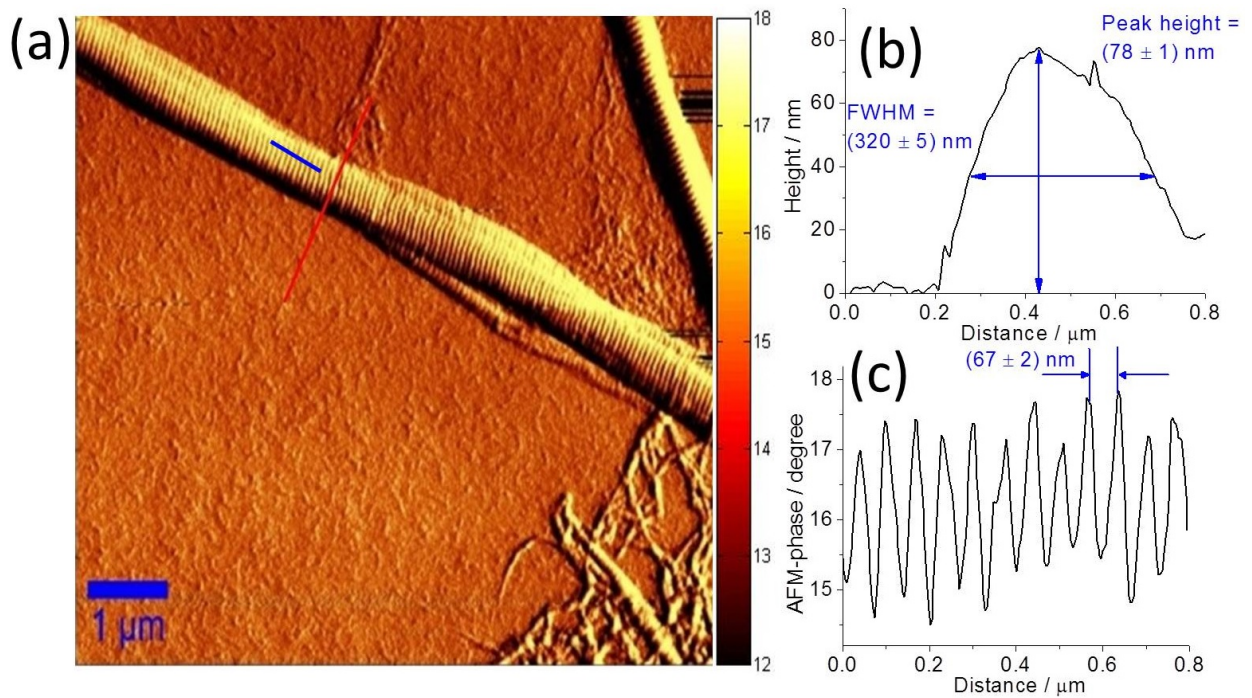


Figure 5.8: (a) AFM phase image of self-assembled collagen (type-I) fibrils on a glass coverslip. (b) The topographical height profile across the fibril (along the red line shown in (a)) with a measured FWHM = (320 ± 5) nm and a peak height of (78 ± 1) nm. (c) The phase profile parallel to the long axis of the fibril (along the blue line shown in (a)) reveals the characteristic D-striation of collagen (type-I) with a period length of (67 ± 2) nm.

displayed in fig. 5.8 (a). The FWHM and peak height of this profile are determined to be (320 ± 5) nm and (78 ± 1) nm, respectively, which are close to and below the diffraction-limited lateral and longitudinal dimensions of the focus used in the subsequent optical experiments with the Olympus UPLSAPO 60 \times N.A. 1.2W IR microscope objective. The phase profile parallel to the fibril long axis (blue line shown in fig. 5.8 (a)) is shown in fig. 5.8 (c). The observed modulation with a period length of (67 ± 2) nm is attributed to the characteristic D-striation of collagen (type-I) [69], which confirms that the sample consists of fibrils that have not denatured on the glass surface. Under the present NLO excitation conditions, strong SHG is expected in these collagen fibrils.

5.4.2.2 SHG image contrast enhancement

In order to demonstrate SHG image contrast enhancement by shortening the excitation laser pulse duration, SHG images of individual collagen fibrils excited with pulse durations of 18.2 fs ($sech^2$) and 7.3 fs ($sech^2$) and constant average power of 900 μ W at the sample are recorded, as shown in fig. 5.9 (a) and (b), respectively. The two SHG images show the identical region of interest. Clearly, a higher SHG image contrast is observed with the 7.3-fs pulses when

compared to excitation with 18.2-fs pulses. To quantify the contrast enhancement, the SHG intensity profiles along the lines indicated by the arrows are used. As shown in fig. 5.9 (c), for the collagen fibril located at $y = 9.3 \mu\text{m}$, an enhancement factor of 2.5 is observed when decreasing the pulse length from 18.2 fs to 7.3 fs, which is in very good agreement with the theoretical prediction of $18.2 / 7.3 = 2.49$ (see eq. 3.26). The FWHM of the SHG intensity profile of this fibril is $(320 \pm 10) \text{ nm}$, which indicates that diffraction-limited SHG imaging is achieved. Next, the SHG intensities at a fixed single collagen fibril position are measured

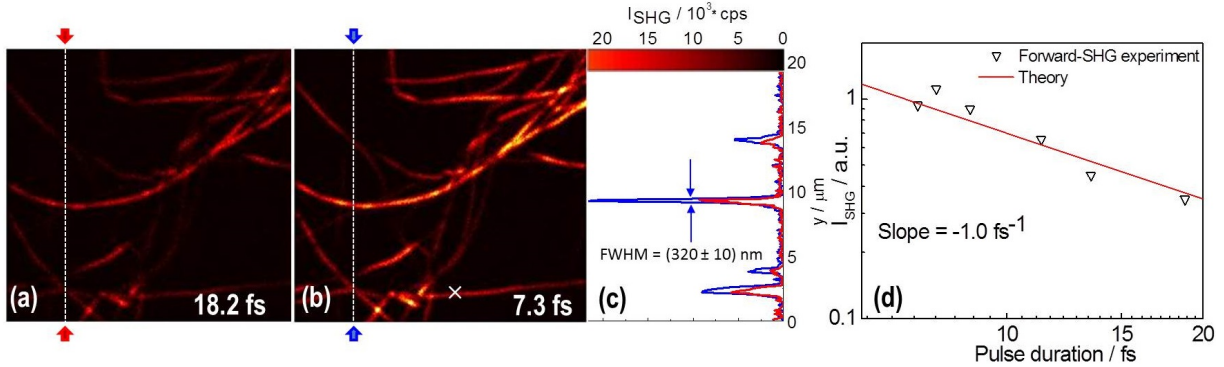


Figure 5.9: Forward-detected SHG images of collagen fibrils obtained with excitation pulse durations of (a) 18.2 fs (sech^2) and (b) 7.3 fs (sech^2) at an average power of $900 \mu\text{W}$ and a pixel dwell time of 2.0 ms. (c) SHG intensity profiles along the lines marked by the arrows in (a) (red curve) and (b) (blue curve). The FWHM of the SHG intensity profile across the fibril located at $y = 9.3 \mu\text{m}$ amounts to $(320 \pm 10) \text{ nm}$. (d) Log-log plot of the measured (∇) and theoretical (red line) SHG intensity as a function of pulse duration.

as a function of pulse duration. In analogy to the experiment presented in section 5.4.1, the pulse duration was adjusted by controlling the insertion of the thin wedges (W) and the average excitation power at the sample was kept constant at $900 \mu\text{W}$. Fig. 5.9 (d) shows the log-log plot of forward-detected SHG signal versus pulse duration (∇). As for the KDP measurement, see fig. 5.7 (b), the good agreement between the experimental data and the simulation (red line) according to eq. 3.26 confirms that the inverse linear dependence of the SHG intensity on pulse duration also holds for type-I collagen fibrils.

5.4.2.3 SHG microspectroscopy of a single collagen fibril

The ratio of forward- to epi-detected SHG intensity is used as an important indicator for the determination of the size of collagen fibrils [70]. In this section, frequency- and time-domain SHG microspectroscopy on a single collagen fibril in both forward- and epi-detection geometries is demonstrated.

Fig. 5.10 (a) shows the frequency-domain SHG spectra recorded in both the forward- (blue curve) and epi- (green curve) detection geometries at a fixed focus position on the single col-

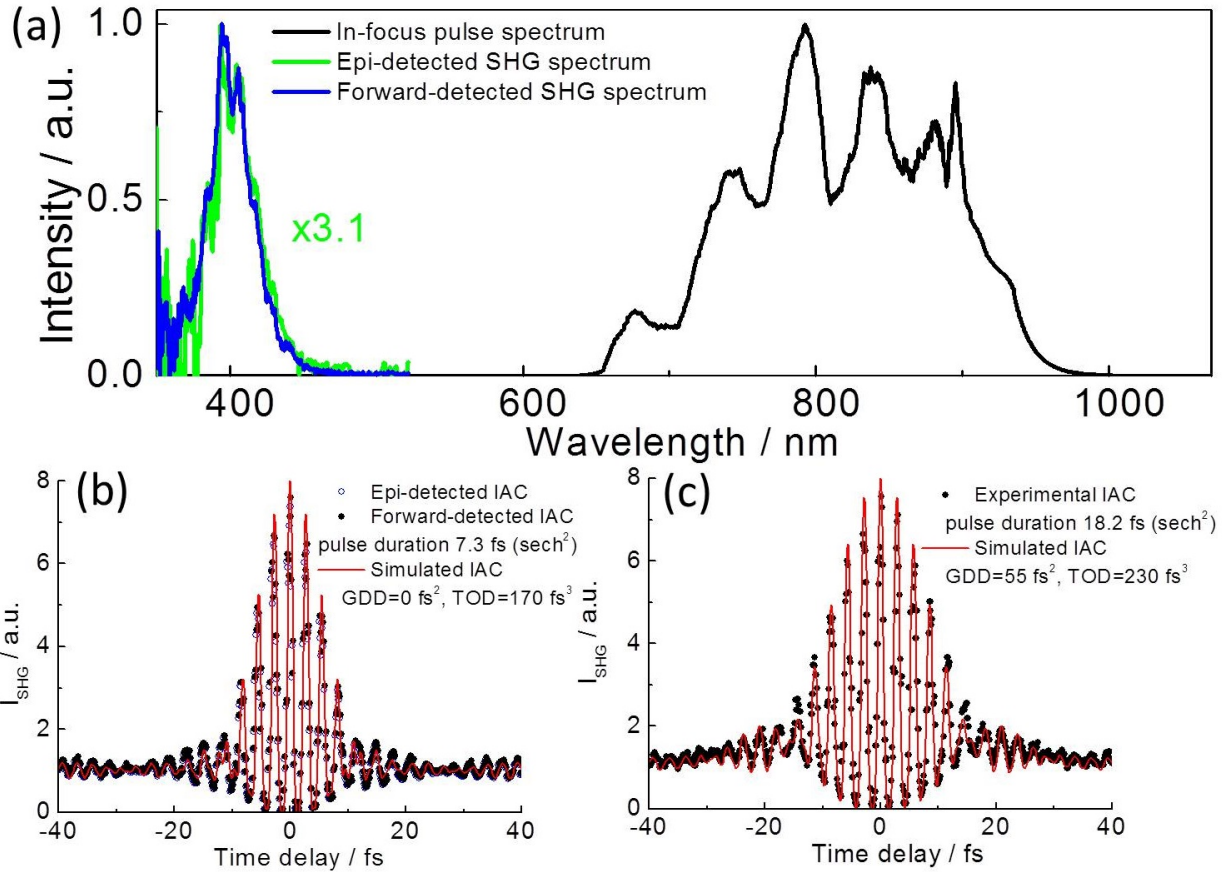


Figure 5.10: (a) SHG spectra of a single collagen fibril recorded in both the forward- (blue curve) and epi- (green curve) detection geometries using excitation with a pulse duration of 7.3 fs ($sech^2$) and an average power of $900 \mu\text{W}$ at the sample. The in-focus excitation pulse spectrum (black curve) is shown for reference. (b) The corresponding epi-detected (empty circles) and forward-detected (solid circles) SHG IAC traces of a single collagen fibril together with the simulated SHG IAC traces (red curve) by assuming the in-focus pulse spectrum shown in (a) and residual dispersion values of $GDD = 0 \text{ fs}^2$ and $TOD = 170 \text{ fs}^3$, which resembles the SHG IAC trace of KDP (see fig. 5.5 (b)). (c) Measured forward-detected SHG IAC trace (black dots) of the same fibril when excited by pulses with a duration of 18.2 fs ($sech^2$) together with a simulated SHG IAC trace by assuming the in-focus pulse spectrum and residual dispersion values of $GDD = 55 \text{ fs}^2$ and $TOD = 230 \text{ fs}^3$.

lagen fibril that is marked by the white cross in fig. 5.9 (b). The average excitation power and pulse duration at the sample are $900 \mu\text{W}$ and 7.3 fs ($sech^2$), respectively. Spectra of isotropic fluorescence centered at about 410 nm of stilbene (Lambdachrome, 4200) dissolved in methanol were recorded in both the epi- and forward-SHG detection geometries. The ratio between the forward- and epi-detected fluorescence was then used to correct the forward- and epi-detected SHG spectra of the single collagen fibril for the different detection sensitivities of the two collection geometries. The SHG spectra shown in fig. 5.10 (a) were also corrected for the spectral

sensitivity response of the camera detector. The forward-detected SHG signal is observed to be (3.1 ± 0.2) times stronger than the epi-detected SHG signal, while their normalized SHG spectra show no difference in spectral features. Using the empirical relation reported by Chu et al. [70], the thickness of this collagen fibril along the z axis was determined to be $2.81 \text{ nm} \times (3.1 \pm 0.2) \text{ nm} + 49.8 = (59 \pm 1) \text{ nm}$. This estimate is a little smaller than the measured AFM peak height for different fibrils shown in fig. 5.8 (b). However, from the AFM experiments [68], we know that the thickness of our self-assembled collagen fibrils vary within the range from 50 to 130 nm. In conclusion, with our novel microscope setup, we can make use of the forward- and epi-detected SHG intensity ratio to estimate the thickness of the collagen fibril. For reference, the in-focus spectrum of the excitation laser pulse is also shown in fig. 5.10 (a).

In the time-domain, fig. 5.10 (b) shows the epi- (empty circles) and forward-detected (filled circles) SHG IAC traces, which are measured on a single collagen fibril, using laser excitation parameters identical to that used for the SHG image in fig. 5.9 (b). Their comparison shows that there is no obvious difference between epi- and forward-detected SHG IAC traces. Both traces nicely resemble the SHG IAC trace recorded for KDP (see fig. 5.5 (b)), for which the best fit with a simulated SHG IAC trace was obtained when using eqs. 3.36 and 3.37 and assuming residual dispersion values of $\text{GDD} = 0 \text{ fs}^2$ and $\text{TOD} = 170 \text{ fs}^3$, shown as red curve in fig. 5.10 (b) for reference.

As shown in fig. 5.10 (c), the forward-detected SHG IAC trace (black dots) was also measured when the pulse duration was increased to 18.2 fs, which corresponds to the same pulse duration used for recording the SHG image in fig. 5.9 (a). The simulated SHG IAC trace (red curve) describes the experimental data best when using the measured in-focus pulse spectrum and residual dispersion values of $\text{GDD} = 55 \text{ fs}^2$ and $\text{TOD} = 230 \text{ fs}^3$.

5.5 Summary and conclusions

In this chapter, the performance of a novel few-cycle NLO microscope for both SHG imaging and SHG microspectroscopy in the frequency- and time-domains was characterized, and the impact of the material dispersion, chromatic and spherical aberrations of common high-N.A. microscope objectives on the focusing of few-cycle pulses was studied.

Using a 1.2-N.A. microscope objective, the diffraction-limited FWHM_{xy} and FWHM_z of the two-photon excitation focus dimensions of $(310 \pm 10) \text{ nm}$ and $(1.3 \pm 0.1) \mu\text{m}$ were achieved.

By purely passive GDD and TOD management, and by using customized low-GDD optical components that support the entire spectral bandwidth of the 6.4-fs oscillator output pulses, near bandwidth-limited pulses with durations ranging from 6.6 fs to 7.3 fs for microscope objectives with N.A.s ranging from 0.5 to 1.2, respectively, were routinely achieved in the focus. From the analysis of SHG IAC traces, the amount of GDD and TOD of the microscope objectives

that need to be pre-compensated in order to achieve the shortest in-focus pulse duration have been estimated. For an objective with N.A. ≥ 0.9 , GDD and TOD values of up to $\sim 2300 fs^2$ and $\sim 1000 fs^3$, respectively, needed to be pre-compensated. Whereas, lower values are required for objectives with lower N.A.s. This observation reflects the expected increase in the optical path length through dispersive glass inside a microscope objective with a higher N.A.. While GDD was pre-compensated successfully for all the objectives studied, residual TOD could not be completely pre-compensated in our setup. The observed increase in the in-focus pulse durations is attributed to the observed increase in residual TOD and higher-order dispersions for objectives with increased N.A.. It has been shown that the residual TOD value extracted from an SHG IAC trace quantitatively explains the narrower spectral bandwidth observed in the corresponding SHG spectrum of the in-focus pulses when compared to their Fourier-limited bandwidth.

The impact of the chromatic and spherical aberrations introduced by the high-N.A. objective on the temporal distortion of the few-cycle pulses inside the focus have been estimated and experimentally tested. It was found that these effects are negligible for the high-quality objectives used throughout our experiments, which are aberration-corrected in the near-infrared wavelength range. In conclusion, residual TOD and higher-order dispersion represent the only limiting factors in our setup for achieving Fourier limited in-focus pulses.

The inverse linear dependence of SHG intensity on the in-focus pulse duration was, to our best knowledge, demonstrated down to 7.1 fs for the first time using an high-N.A. microscope objective. The application of shorter in-focus pulses for the enhancement of SHG image contrast was successfully demonstrated on a single collagen (type-I) fibril as a biological model system for studying protein assemblies under physiological conditions.

Beyond imaging, the capability of our few-cycle NLO microscope to perform SHG microscopy in both the frequency- and time-domains was successfully demonstrated. Experiments on a single collagen fibril in its native conformation with a thickness below ~ 100 nm revealed indistinguishable SHG spectra irrespective of detecting its forward- or epi-scattered SHG. Likewise, SHG IAC traces of a fibril recorded in the forward- and epi-detection geometries are indistinguishable and resemble the instantaneous SHG response observed in KDP or BBO crystals. Consequently, a collagen fibril has been found to act as a purely non-resonant $\chi^{(2)}$ soft matter under the present excitation conditions. However, the absolute forward-detected SHG intensity of a single fibril was observed to be approximately three times stronger than the corresponding epi-detected signal. Based on SHG phase-matching considerations, their ratio allows for the estimation of the fibril thickness of about 60 nm, which corresponds well with the range of the thickness from 50 to 130 nm, as independently determined for various self-assembled fibrils by AFM imaging.

Our successful demonstration of few-cycle NLO microscopy with both diffraction-limited

spatial resolution and near bandwidth-limited 7-fs in-focus pulses is the prerequisite for studying ultrafast plasmon dephasing processes in a single metallic nanoparticle and nanocavity, which will be presented in the following chapters of this thesis. The high peak power that can be achieved in the focus is also desirable for potential applications in laser material processing.

6 Time-resolving ultrashort plasmon dephasing in single gold nanoparticles

6.1 Motivation

The ultrafast dephasing of the localized surface plasmon in the nanoparticle, that occurs on a time scale of only few femtoseconds, has gained a lot of attraction [46] [7] [8] [71] [29] [72–80]. The linear scattering spectroscopy is a standard method to investigate spectral bandwidth and resonance wavelength of the LSPR of individual nanoparticles and its dependence on the nanoparticle's size, shape, composition, and local environment in the frequency-domain [72] [29] [74] [76], from which dephasing time are retrieved. Directly time-resolving the plasmon dephasing time, includes interferometric SHG spectroscopy of an ensemble of nanoparticles [7] [73]. To avoid an inhomogeneous size distribution of nanoparticles, Liao et al. [8] reported a proof of principle experiment with excitation pulses of 23 fs, which was able to resolve a dephasing time of 10 fs for a single Ag colloid of 75 nm diameter. However, a systematic time-domain SHG study of single metal nanoparticles of different sizes and shapes has not been reported yet. For this purpose, much shorter dephasing times are expected, according to the linear scattering spectroscopy, for which the time-resolution of the experiment needs to be shorter than the maximum dephasing time of 18 fs [29]. The motivation of this work is to investigate the single gold nanoparticles of different sizes and shapes using both linear DF scattering in the frequency-domain and interferometric SHG spectroscopy in time-domain with our in-focus 7.3-fs laser excitation pulses. To our best knowledge, such a systematic investigation of linear and second-order LSPR properties on one and the same single nanoparticle is still lacking, which allows testing the applicability of a simple driven damped harmonic oscillator model [46, 75] to explain both linear and SHG scatterings.

In this chapter, we present the experimental study of LSPR properties of individual nanospheres, nanorods, nanodisks, and nanorectangles of various sizes and shapes using linear and SHG properties in the frequency- and time-domains in combination with polarization-resolved experiments.

6.2 Materials and methods

6.2.1 Microscope configurations

Since various experiments are discussed in this chapter, the details of the detection geometry, filters, and detectors of different configurations of the DF scattering microscope and the NLO microscope are listed in table 6.1.

Table 6.1: The DF scattering and NLO microscope configurations for the detection geometry, filters, and detectors used for the different experiments discussed in this chapter.

section	experiments	detection geometry	filters	detectors
6.3.3, 6.3.4 6.4.2, 6.4.3	DF scattering spectrum measurements	Forward	no filters	Spectrometer
6.3.4.2 6.3.4.1 6.4.3, 6.4.2	Polarization-resolved DF scattering measurements	Forward	band-pass filter (Coherent, 660 nm / 40 nm) band-pass filter (Chroma, HQ 585 nm / 80 nm) band-pass filter (Chroma, ET 890 nm / 220 nm)	PMT
6.3.4, 6.4.3 6.6.2, 6.7.2	SHG spectrum measurements	Epi	band-pass filter (Semrock, KFF01 405 nm / 150 nm)	Spectrometer
6.3.4, 6.4.3 6.6.2, 6.7.2	SHG image measurements	Epi	band-pass filter (Semrock, KFF01 405 nm / 150 nm) and short-pass filter (Omega 450 nm)	APD
6.3.4, 6.4.3 6.6.2, 6.7.2	Polarization-resolved SHG measurements	Epi	band-pass filter (Semrock, KFF01 405 nm / 150 nm) and short-pass filter (Omega 450 nm)	APD
6.3.4, 6.4.3 6.6.2, 6.7.2	SHG IAC trace measurements	Epi	band-pass filter (Semrock, KFF01 405 nm / 150 nm) and short-pass filter (Omega 450 nm)	APD
6.3.4, 6.4.3 6.6.2, 6.7.2	Polarization-resolved TPF measurements	Epi	band-pass filter (Chroma, HQ 585 nm / 80 nm) and band-pass filter (Throlabs, FGB37)	APD

6.2.2 The gold nanosphere and nanorod samples

The aqueous suspensions of gold nanospheres with a diameter of 50 nm (NanoPartz, A11-50-NPC-25), 80 nm (NanoPartz, A11-80-NPC-25), 125 nm (NanoPartz, A11-125-NPC-25) and gold nanorods with dimensions of $40 \times 69 \text{ nm}^2$ (NanoPartz, A12-40-600-CTAB-25), $39 \times 155 \text{ nm}^2$ (NanoPartz, A12-40-800-25), and $10 \times 40 \text{ nm}^2$ (NanoPartz, A12-10-808-25) are used. It should be noted that for each nanoparticle with a certain dimension, there is a deviation from the specified shape with a standard deviation of 4% to 10%, according to the manufacturer's specification. For the experiments, the samples were simply prepared as follows: first drop 10 μL gold nanoparticle suspension as purchased on a standard coverslip (Carl Roth GmbH, $24 \times 32 \text{ mm}^2$, #1), which was previously cleaned by methanol and subsequently acetone. Then, the liquid on the coverslip was removed away by using a pipette after two minutes of incubation. Using this method, a sample with nanoparticles homogeneously located in some regions on the

coverslip can be obtained. The adhesion of the nanoparticles on the coverslip, especially for the nanospheres, is compensated by the tightly focus laser pulses, which makes NLO spectroscopy on immobilized nanoparticles difficult or sometimes even impossible. This problem can be solved by heating the sample at 200 °C for 20 minutes by using a hot plate (C-MAG HS 4, Ika). One possible explanation for this is the evaporation of water or the removal of chemicals, which are additives used to prevent nanoparticles from agglomeration in the purchased suspension. If not stated otherwise, refractive index matching immersion oil (Olympus, Type-F, $n=1.518$) was dropped onto the immobilized nanoparticles on the glass surface.

6.2.3 The gold nanodisk and nanorectangle array samples

In order to systematically study the dependence of plasmon dephasing in a nanoparticle on its shape and size, it is a prerequisite to know its shape and size. Electron beam lithography (EBL), which is capable of producing a gold structure with an accuracy of 10 nm is used here for sample fabrication [78]. The gold nanodisks and nanorectangles on a BK7 microscope cover glass (Carl Roth GmbH, $24 \times 32 \text{ mm}^2$, #1) prepared by our collaborator from the Max-Planck-Institut für Festkörperforschung are schematically shown in fig. 6.1. The nanodisks have diameters of 20, 40, 60, 80, 100, 120, 140, and 160 nm, and the nanorectangles have $L_y \times L_x$ dimensions of 25×100 , 33×100 , 50×100 , 100×100 , 100×50 , 100×33 , and $100 \times 25 \text{ nm}^2$. The height of these nanodisks and nanorectangles is 25 nm. The center to center distance between two neighboring individual nanoparticles is designed to be $2.0 \mu\text{m}$ in order to avoid coupling between nanoparticles.

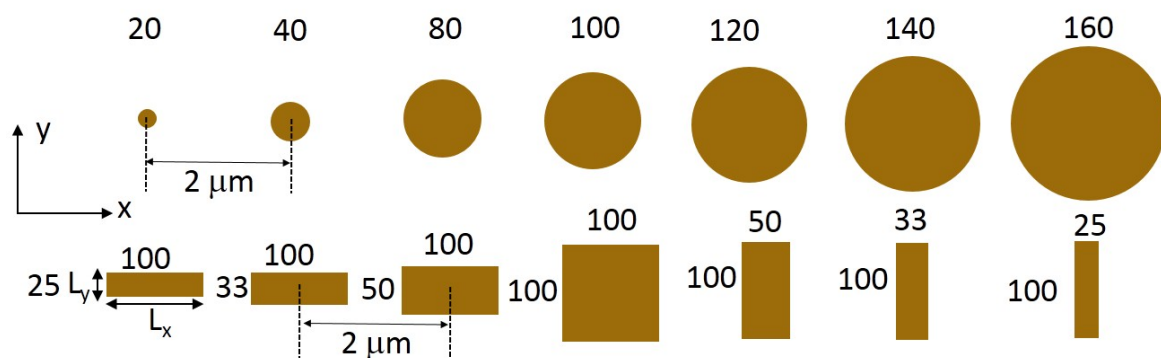


Figure 6.1: Schematic layout showing the arrangement of the gold nanodisks (upper row) with diameters of 20, 40, 60, 80, 100, 120, 140, and 160 nm and of nanorectangles (lower row) with $L_y \times L_x$ dimensions of 25×100 , 33×100 , 50×100 , 100×100 , 100×50 , 100×33 , and $100 \times 25 \text{ nm}^2$ as manufactured by EBL. The center to center distance between two neighboring nanoparticles is $2.0 \mu\text{m}$. For all these nanoparticles, the height is 25 nm.

6.2.4 Extinction measurements

For the bulk characterization of linear plasmon properties of gold nanosphere and nanorod aqueous suspensions, extinction spectra were measured in a quartz cuvette (optical path length of 10 mm) using an UV-VIS spectrometer (PerkinElmer, Lambda 16). Extinction spectra averaged over more than one nanodisk and nanorectangle of the same size were separately measured by our collaborator using a Fourier-transform infrared (FTIR) spectrometer (Bruker Vertex-80).

6.2.5 Scanning electron microscope imaging

For the characterization of the size distribution of the purchased gold nanoparticles, a scanning electron microscope (SEM) (Hitachi Model S-4800) was used.

6.2.6 Extinction and scattering spectra simulations

The linear extinction and scattering spectra of individual gold nanoparticles with different shapes and sizes were simulated in MATLAB R2012a (MathWorks) using the metallic nanoparticle boundary element method (MNPBEM) toolbox, which was developed by Ulrich Hohenester and Andreas Trügler [43]. The main idea of the MNPBEM toolbox is to simulate the electromagnetic properties of a metallic nanoparticle by solving Maxwell's equations for a dielectric environment, where both the nanoparticle and the surrounding environment with homogeneous and isotropic dielectric functions separated by abrupt interfaces are assumed. There are mainly three working procedures of the MNPBEM toolbox for the simulation: construct a nanoparticle object according to its dimensions, define the excitation field, and solve Maxwell's equations. The dielectric function used for the gold nanoparticle was taken from literature [38]. A wavelength-independent refractive index for the surrounding medium is assumed. To define the particle boundaries, 20 vertices and faces were used for all the nanoparticles. The plane wave excitation with linear light polarization was used. In all cases, the full BEM is employed to solve the full set of Maxwell's equations. The scattering and extinction cross sections in units of nm^2 are calculated.

6.3 Gold nanosphere experiments

6.3.1 Size characterization by SEM imaging

In order to determine the derivation from the spherical geometry with a diameter specified by the manufacturer, the size of different gold nanoparticles with a diameter 125 nm were investigated by SEM. From the SEM image shown in fig. 6.2, one can observe that the morphology of these nanoparticles is not perfectly spherical. If we assume that it is an ellipsoid with the long

and short semi-axis defined as a and b , respectively, the statistical analysis of a and b of the five individual nanoparticles shown in fig. 6.2 is listed in table 6.2. The mean values for a and b were determined to be (143 ± 2) nm and (129 ± 2) nm, respectively, which deviate from the spherical diameter 125 nm specified by the manufacturer. The mean of the aspect ratio a/b is (1.10 ± 0.11) , which exhibits a 10% deviation from the perfect spherical shape. This result agrees well with the upper boundary of the standard deviation specified by the manufacturer. The observed inhomogeneous size and shape distributions will consequently introduce the inhomogeneous broadening in ensemble experiments. The single nanoparticle experiments are required in order to avoid inhomogeneous broadening.

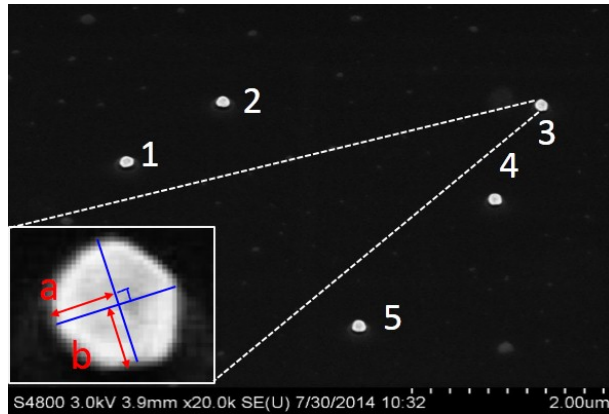


Figure 6.2: SEM image of individual nanosphere 125 particles. The scale bar is $2.00 \mu\text{m}$. The insert image shows a high magnification of nanoparticle 3 with $a = 73.5$ nm and $b = 63.5$ nm.

Table 6.2: Statistical analysis for the five individual nanosphere 125 nanoparticles shown in fig. 6.2.

No.	2a (nm)	2b (nm)	a/b
1	143	123	1.16
2	136	134	1.01
3	147	127	1.16
4	142	129	1.10
5	150	133	1.13
mean \pm std	143 ± 2	129 ± 2	1.10 ± 0.11

6.3.2 Ensemble characterization by UV-VIS spectroscopy

Normalized extinction spectra of the gold nanoparticle suspensions are shown in fig. 6.3. One can observe that the center wavelength of the broad-band extinction spectrum of nanosphere

suspension is red-shifted with the increasing of the size of the nanoparticle. Also, the FWHM of the extinction spectrum is increasing with the increasing of the size of nanoparticle. The manufacturer specified diameter, the measured center wavelength, and the FWHM of the extinction spectra of gold nanosphere suspensions are listed in the table 6.3.

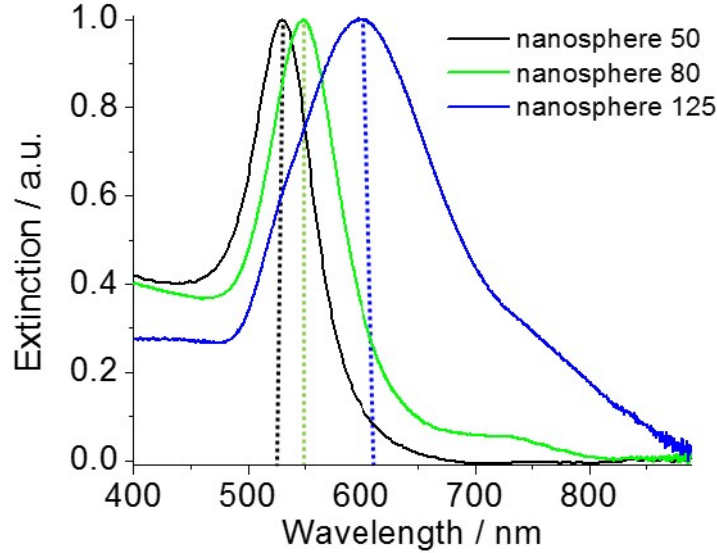


Figure 6.3: Measured ensemble extinction spectra of aqueous suspensions of nanosphere 50, nanosphere 80, and nanosphere 125.

Table 6.3: The ensemble characteristics of aqueous nanosphere suspensions used in this work.

Name	manufacturer specified diameter	ensemble extinction measurements	
	mean \pm std (nm)	center wavelength λ_{center} (nm)	FWHM (nm)
nanosphere 50	50 \pm 7	531	75
nanosphere 80	75 \pm 7	548	86
nanosphere 125	136 \pm 10	598	171

6.3.3 Single nanosphere characterization by DF spectroscopy

Before performing NLO spectroscopy measurements, the single nanoparticles were characterized by a home-built DF microscope. Three representative DF scattering spectra measured for different individual nanospheres with a specified diameter of 50 nm, 80 nm, and 125 nm, are shown in fig. 6.4, which were obtained by using the processing procedures described in section 4.3.3. The acquisition time for each spectrum is 1.0 s. One can observe that the simulated scattering spectrum (red curve) for nanosphere 50, which is based on the Mie theory

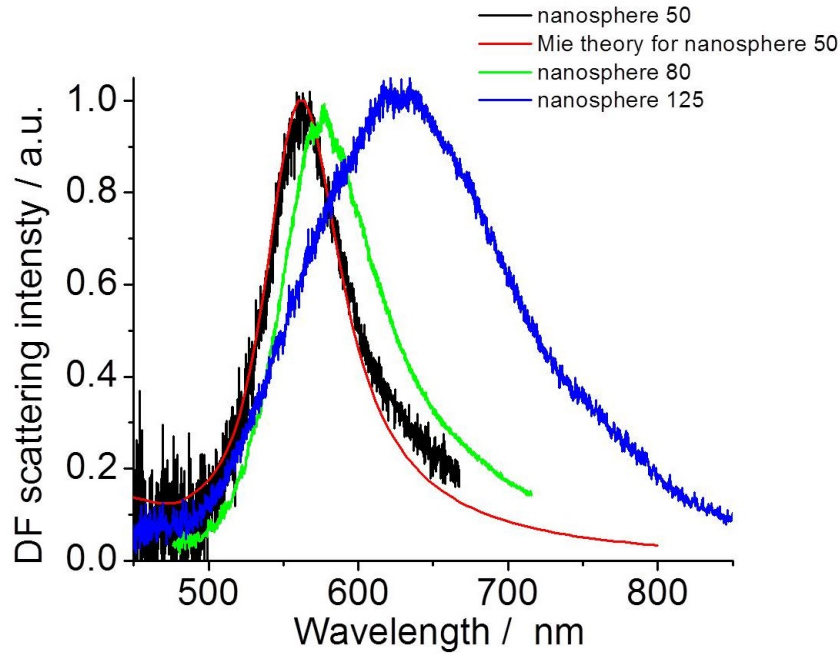


Figure 6.4: Measured DF scattering spectra of individual spherical nanoparticles with specified diameters of 50 nm (black curve), 80 nm (green curve), 125 nm (blue curve) immersed in oil with a refractive index of 1.518. The simulated scattering spectrum (red curve) of a spherical nanoparticle with a designed diameter of 50 nm placed in oil based on Mie theory is also shown for reference.

using MNPBEM toolbox describes the experimental curve (black curve) well. The resonance wavelength of nanosphere 50, 80, and 125 is determined to be 563 nm, 578 nm, and 626 nm, respectively. The respective FWHMs are also determined to be 58 nm, 80 nm, and 160 nm. One can observe that with increasing the particle diameter, the resonance wavelength is red-shifted, and the bandwidth is increasing. Compared to the center wavelength and the FWHM as retrieved from the extinction spectrum of ensemble aqueous suspensions (see table 6.3), the resonance wavelength has a systematic red-shift and the spectral bandwidth is systematically narrower for the corresponding single nanoparticle spectrum. The reasonable explanation for the red-shift is that the immersion medium was changed from water to oil. The lack of inhomogeneous broadening in the single nanoparticle spectrum explains the narrower spectral bandwidth (see eq. 3.64). This observation confirms that single nanoparticle measurements are necessary for the study of the size and shape dependence of plasmon resonance properties.

6.3.4 Single nanosphere characterization by SHG experiments

In this section, first the single nanoparticle is characterized by using DF microspectroscopy. Then the SHG spectroscopy characterization is performed on the same nanoparticle in both the frequency- and time-domains. A whole experimental data set for a single nanoparticle

consists of several measurements including a DF scattering spectrum, a polarization-resolved DF scattering intensity, an SHG spectrum, polarization-resolved SHG intensity, and an SHG IAC trace measurements.

6.3.4.1 The nonresonant excitation case: 80 nm sphere

For the nanosphere 80 sample, the measured DF scattering spectrum (green curve) for a single nanoparticle is shown in fig. 6.5 (a). One can observe the resonance band, which is best fitted by a single Lorentzian line (purple curve, see the square of eq. 3.60) with a resonance wavelength of $\lambda \approx 581$ nm and with a FWHM of $\Delta\omega = (85 \pm 4)$ nm. Using eq. 3.63, the corresponding dephasing time is determined to be $T_2 = (4.2 \pm 0.2)$ fs. Comparing these values with those obtained from the spectrum of the single nanosphere 80 shown in fig. 6.4, there are no big differences. Compared to the ensemble spectrum shown in fig. 6.3, the resonance wavelength of the nanoparticle selected here is 33 nm red-shifted with respect to the center wavelength of the inhomogeneous broadened ensemble spectrum. Compared to the DF scattering experiment for a single gold nanosphere of 80 nm in oil with $\lambda_{res} = 590$ nm and $T_2 = 3.3$ fs reported in reference [29], the corresponding resonance wavelength and dephasing time of the nanosphere selected here is shorter and longer, respectively. This comparison suggests that the actual size of the selected nanosphere is smaller than 80 nm. In fig. 6.5 (a), one can also observe that the DF scattering spectrum of this nanosphere 80 has only small spectral components overlapping with the in-focus excitation laser spectrum (red curve), which suggests that the plasmon resonance enhancement of SHG will be very weak. The measured SHG spectrum of the same nanosphere (black curve) is also shown in fig. 6.5 (a). The purely nonresonant SHG spectrum of a KDP crystal (blue curve) is also shown here for reference. These two spectra are in good agreement, which also indicates that the plasmon resonance observed in the linear DF scattering spectrum does not have an obvious effect on its SHG spectrum.

Fig. 6.5 (b) shows the normalized polarization-resolved DF scattering and SHG intensities recorded on the same single nanoparticle. The DF scattering polar plot is not isotropic, which indicates that a nonperfect spherical nanoparticle was measured. The SHG polar plot is also not isotropic, but is oriented as that of the linear DF scattering. There shows up a narrower intensity 'waist' in SHG polar plot when compared to the DF scattering polar plot, which can be explained by the fact that the SHG signal is more sensitive to the morphology of the nanoparticle.

Fig. 6.5 (c) shows the measured SHG IAC trace (black squares) of this single nanosphere. It is worthy noting that the SHG IAC trace is obtained by averaging 20 individual traces of the same nanoparticle in order to increase the single-to-noise (S/N). The ratio of 8:1 between the SHG intensities measured at time delays zero and ± 40 fs confirms that two-photon excitation process was observed. For comparison, the simulated SHG IAC trace (blue curve) for the instantaneous KDP response to our in-focus excitation pulse of (7.3 ± 0.3) fs ($sech^2$) and residual

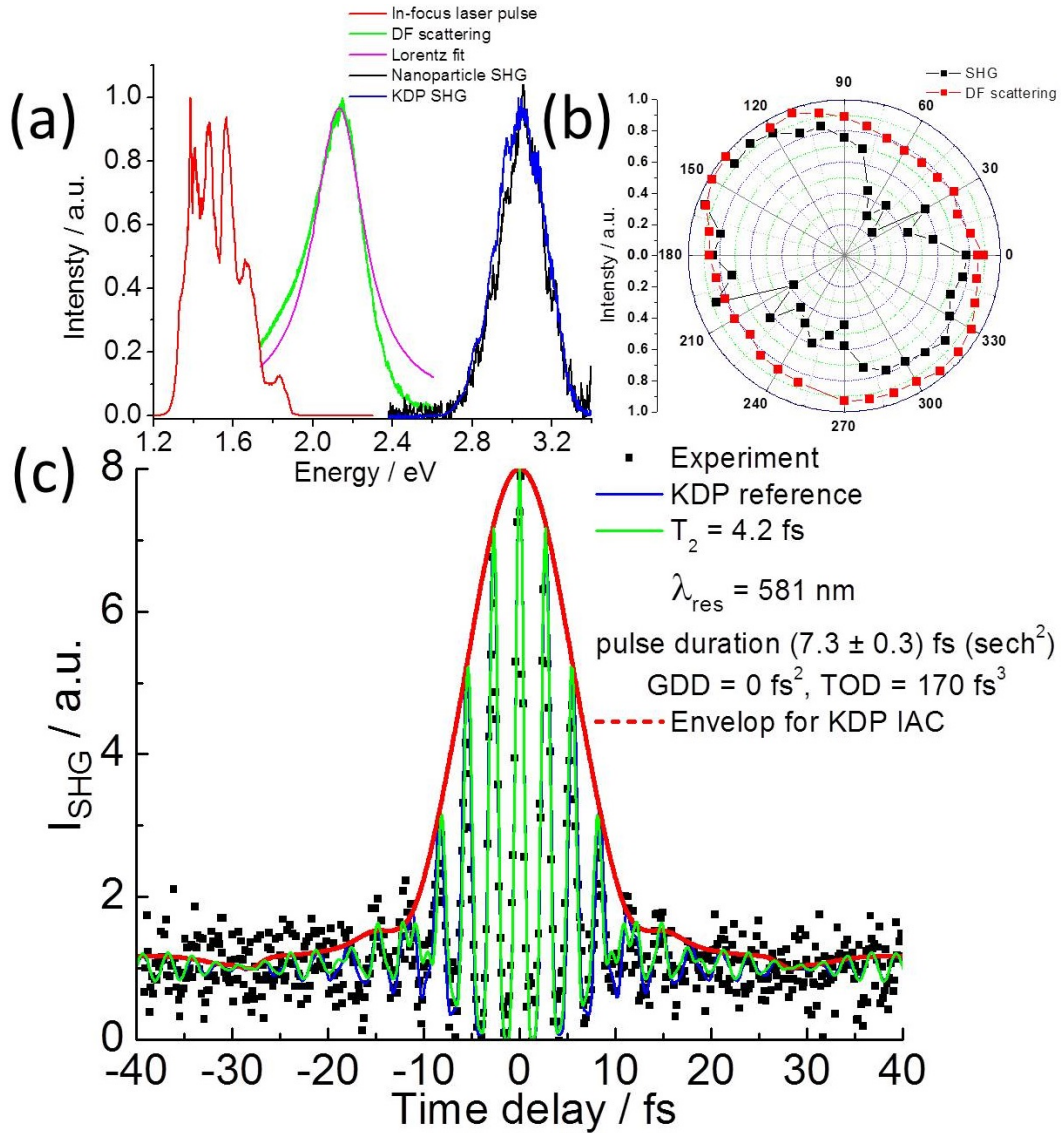


Figure 6.5: (a) Measured DF scattering spectrum (green curve) and the corresponding fit to Lorentzian line-shape (purple curve) are shown together with the SHG spectrum of the same single nanosphere 80 nanoparticle (black curve) in oil. The SHG spectrum of the KDP crystal (blue curve) and the in-focus laser spectrum (red curve) are also shown for reference. (b) Normalized polar plots of the DF scattering intensity (red line symbols) and the SHG intensity (black line symbols) for the same individual nanoparticle. (c) Measured SHG IAC trace (black squares) of the same nanoparticle and the simulated SHG IAC traces for the instantaneous response of KDP (blue curve) and for a plasmon resonance enhanced SHG for a nanosphere with $T_2 = 4.2$ fs and $\lambda_{res} = 581$ nm (green curve) using an in-focus pulse with a pulse duration of (7.3 ± 0.3) fs ($sech^2$) and residual dispersion values of $GDD = 0$ fs² and $TOD = 170$ fs³. The upper envelope (red curve) for the simulated SHG IAC trace of the instantaneous response is shown. The average powers used in the SHG experiments shown in (a), (b), and (c) are 210 μ W, 370 μ W, and 380 μ W, respectively.

dispersion values of $GDD = 0 \text{ fs}^2$ and $TOD = 170 \text{ fs}^3$ is also shown in fig. 6.5 (c). There are no major differences observed between SHG IAC traces of the nanosphere and of the KDP crystal, which indicates that the linear plasmon resonance centered at 580 nm is not efficiently excited by the spectral components within the bandwidth of our in-focus laser spectrum. This explanation is supported by the comparison of the simulated resonance enhanced SHG IAC trace for $T_2 = 4.2 \text{ fs}$ and $\lambda_{res} = 581 \text{ nm}$ (green curve, see section 3.4.5) with that for the nonresonant KDP reference trace, which are almost indistinguishable. A broadening of the envelope (red dash curve) of SHG IAC trace is not observed when the resonance wavelengths are outside the spectral bandwidth of our excitation laser pulses.

6.3.4.2 The near-resonant excitation case: 125 nm sphere

For the nanosphere 125 sample, the measured DF scattering spectrum (green curve) for a single nanosphere is shown in fig. 6.6 (a). One can observe a resonance band, which is best fitted by a single Lorentzian line (purple curve, see the square of eq. 3.60) with a resonance wavelength of $\lambda_{res} \approx 670 \text{ nm}$ and with a FWHM of $\Delta\omega = (194 \pm 4) \text{ nm}$. Using eq. 3.63, the corresponding dephasing time is determined to be $(2.5 \pm 0.2) \text{ fs}$. Comparing these values with those obtained from the spectrum of the single nanosphere 125 shown in fig. 6.4, there is a red-shift of the resonance wavelength, and also the bandwidth is broader. Compared to the ensemble spectrum shown in fig. 6.3, both values for the nanoparticle selected here are larger. These comparisons suggest that the actual size of the selected nanosphere is bigger than the mean value specified by the manufacturer. One can also observe that the DF scattering spectrum of this nanosphere has only spectral overlap with the red-part of the excitation laser spectrum (red curve), which suggests that the plasmon resonance enhancement of SHG will be more efficient than in the nanosphere 80 case. The measured SHG spectrum of the same nanosphere (black curve) is shown in fig. 6.6 (a). The pure nonresonant SHG spectrum of a KDP crystal (blue curve) is also shown here for reference. There are no major differences between these two SHG spectra, which indicates that the plasmon resonance observed in the linear DF scattering spectrum does not have an obvious effect on its SHG spectrum.

Fig. 6.6 (b) shows the normalized polarization-resolved DF scattering and SHG intensities recorded on the same single nanoparticle. The DF scattering polar plot is not isotropic, which indicates that a non-perfect spherical nanoparticle was measured. The ratio of the maximum to minimum intensities in this polar plot is determined to be 1.4, which is close to the mean aspect ratio of (1.1 ± 0.1) obtained from the SEM image analysis (see table 6.2). The SHG polar plot is also not isotropic, but is oriented in the same manner as the linear DF scattering. The SHG polar plot has a narrow intensity waist when compared to the DF scattering polar plot, which can be explained by the fact that SHG signal is more sensitive to the morphology of the nanoparticle.

One typical SHG IAC trace (black squares) measured for a single nanosphere 125 is shown

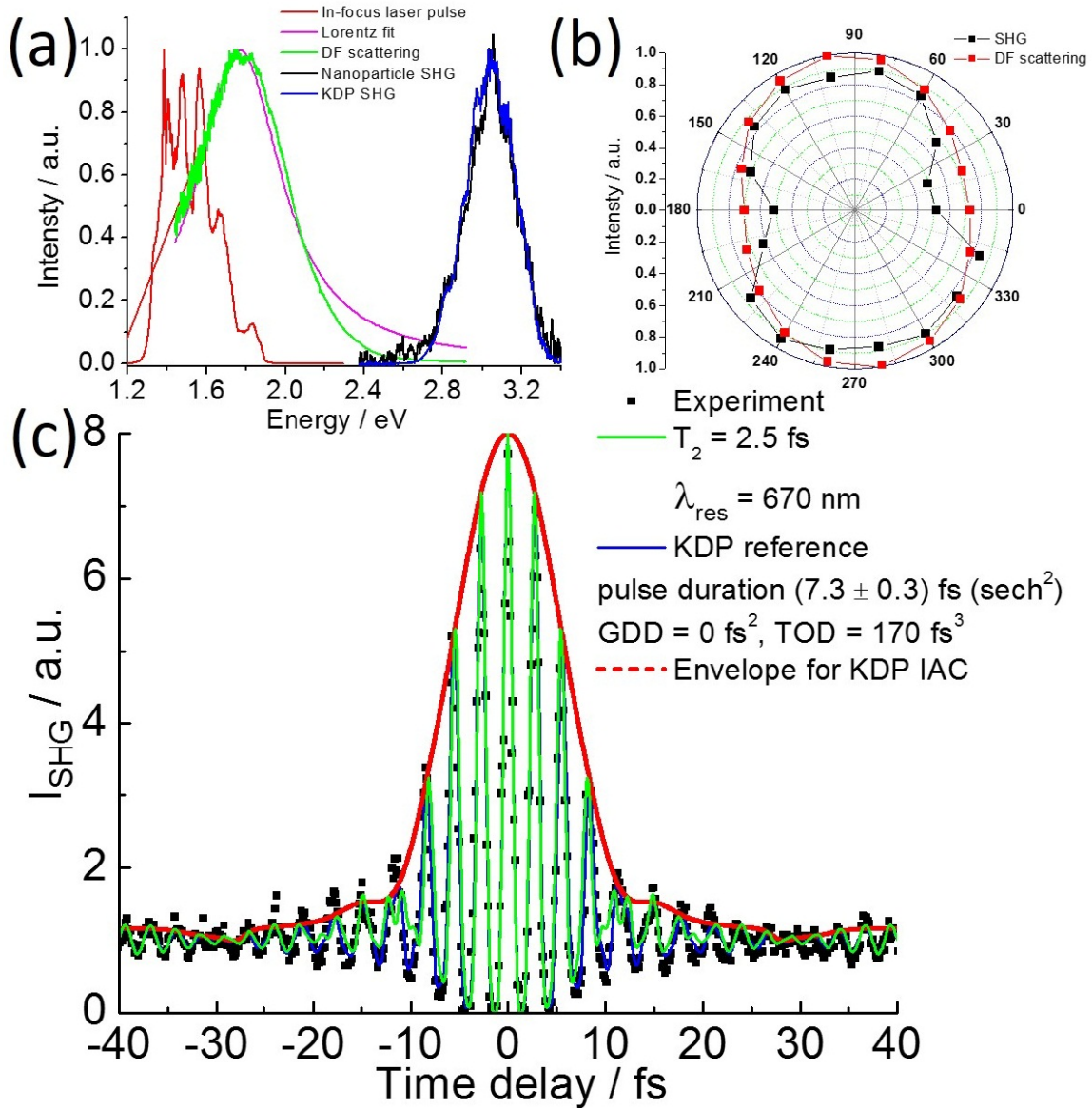


Figure 6.6: (a) Measured DF scattering spectrum (green curve) and the corresponding fit to Lorentzian line-shape (purple curve) are shown together with the SHG spectrum of the same single nanoparticle 125 nanoparticle (black curve) in oil. The SHG spectrum of the KDP crystal (blue curve) and the in-focus laser spectrum (red curve) are also shown for reference. (b) Normalized polar plots of the DF scattering intensity (red symbols) and the SHG intensity for the same nanoparticle. (c) Measured SHG IAC trace (black squares) of the same nanoparticle and the simulated SHG IAC traces (blue curve) for the instantaneous response of KDP (blue curve) and for the plasmon resonance enhanced SHG for a nanoparticle with $T_2 = 2.5$ fs and $\lambda_{\text{res}} = 670$ nm (green curve) using an in-focus pulse with a pulse duration of (7.3 ± 0.3) fs (sech^2) and residual dispersion values of $\text{GDD} = 0 \text{ fs}^2$ and $\text{TOD} = 170 \text{ fs}^3$. The upper envelope (red curve) of a simulated SHG IAC trace for an instantaneous response is shown. The average powers used in the SHG experiments shown in (a), (b), and (c) are $210 \mu\text{W}$.

in fig. 6.6 (c), which is obtained by averaging 20 individual SHG IAC trace measurements of the same nanoparticle in order to increase the S/N. No sample damage was observed during the measurement with an in-focus laser average power of $210 \mu\text{W}$. The ratio of 8:1 between the SHG intensities measured at time delays zero and ± 40 fs confirms that a two-photon excitation process was observed. For reference, the simulated SHG IAC trace (blue curve) for the instantaneous KDP response to our in-focus laser pulse of 7.3 fs (*sech*²) and residual dispersion values of $\text{GDD} = 0 \text{ fs}^2$ and $\text{TOD} = 170 \text{ fs}^3$ is also shown in fig. 6.6 (c). One can observe that there is no obvious difference between the experimental SHG IAC trace of this nanoparticle and the simulated SHG IAC traces of the KDP crystal (blue curve), which indicates that the plasmon resonance centered at 670 nm observed in the linear DF scattering spectrum is not efficiently excited by the blue spectral components of the excitation laser pulse used in our experiment. This explanation is supported by the comparison of the simulated SHG IAC trace (green curve) for a plasmon resonance enhanced SHG with $T_2 = 2.5$ fs and $\lambda_{res} = 670$ nm (see section 3.4.5) with that for the nonresonant KDP reference. As for the nanosphere 80 sample, within the accuracy of our experiment, they are almost indistinguishable and a broadening of the envelope is not observed when compared to that of the KDP crystal reference (red dash curve).

As shown in fig. 6.4, with increasing the diameter of nanospheres, the resonance is red-shifted, and the bandwidth is increased. By extrapolating these trends and the literature values reported by Sönnichsen et al. [29], a nanosphere with $\lambda_{res} = 800$ nm would correspond to $T_2 = 1.2$ fs. While such nanoparticle would be a good candidate for an efficient resonance enhanced SHG, the expected dephasing time is beyond the time-resolution of our experiment. Therefore, we switched to the experiments on single nanorods, which can possess resonance wavelength inside the spectral range of our excitation laser pulses and a narrow bandwidth.

6.4 Gold nanorod experiments

Nanorods are of particular interest because of their strong linear scattering cross sections and narrow spectral bandwidths of the longitudinal localized surface plasmon resonances that can be tuned through our excitation laser spectral region by varying the ratio between the length and the diameter (aspect ratio, AR) of the nanorod. Therefore, the nanorod is expected to yield resonance enhanced SHG and a plasmon dephasing time longer than that of nanospheres. This section will present the experimental characterization of DF scattering and SHG experiments on one and the same nanorods.

6.4.1 Ensemble characterization by UV-VIS spectroscopy

Normalized extinction spectra of various gold nanorod suspensions are shown in fig. 6.7. One can observe that the center wavelength of the broad-band extinction spectrum is red-shifted

with increasing specified aspect ratio of the nanorod. For a given aspect ratio, the FWHM is increasing with decreasing size. The retrieved band shape parameters are listed in table 6.4. For the nanorod 808 suspension, the center wavelength of 808 nm as specified by the manufacturer does not fit exactly to our observed value of 773 nm, which might be caused by the aggregation of nanorods in the investigated suspension.

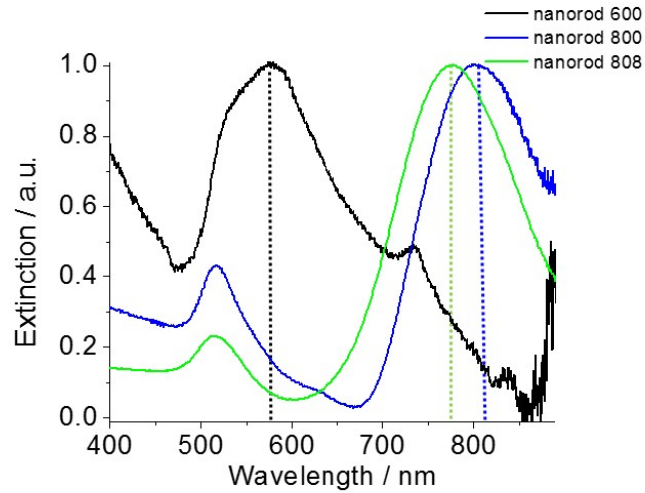


Figure 6.7: Measured ensemble extinction spectra of aqueous suspensions of nanorod 600 ($40 \times 69 \text{ nm}^2$, black curve), nanorod 800 ($39 \times 155 \text{ nm}^2$, blue curve), and nanorod 808 ($10 \times 40 \text{ nm}^2$, green curve).

Table 6.4: The ensemble characteristics of aqueous nanorod suspensions used in this work.

Name	manufacturer specified size		ensemble extinction measurements	
	size $L_y \times L_x$ (nm^2)	aspect ratio L_x / L_y	center wavelength λ_{center} (nm)	FWHM (nm)
nanorod 600	40 X 69	1.7	578	193
nanorod 800	39 X 155	4.0	803	86
nanorod 808	10 X 40	4.0	773	154

6.4.2 Single nanorod characterization by DF scattering spectroscopy

For a single nanorod 800 with a specified size of $39 \times 155 \text{ nm}^2$, DF scattering spectra for different angles α between the linear polarization of the excitation field and the long-axis of the nanorod at 80° (black curve), 120° (red curve), and 160° (blue curve) are shown in fig. 6.8 (a). In all three spectra, both the long-axis and short-axis plasmon modes of the nanorod at the resonance wavelength of 828 nm and 530 nm, respectively, are clearly resolved. The DF scattering intensity of the short-axis mode, which mainly represents the property of the gold

material, is very weak, while the long-axis plasmon mode has a much stronger DF scattering intensity. Because the linear scattering of the short-axis plasmon resonance is weak and exhibits a resonance wavelength outside of the wavelength range from 650 nm to 1000 nm of the excitation laser pulse, we do not consider further the short-axis plasmon mode. Compared to the ensemble extinction spectrum of nanorod 800 suspension shown in fig. 6.7, the FWHM of the long-axis mode is much narrower for the single nanorod ($\Delta\omega = 72$ nm), which manifests that inhomogeneous broadening is responsible for the broader bandwidth observed in the ensemble extinction spectrum (see eq. 3.64). Compared to the single nanosphere experiments presented in section 6.3.3, the nanorod exhibits a much narrower plasmon resonance bandwidth.

The normalized DF scattering intensity obtained by integrating the long-axis plasmon resonance band as a function of α is shown in fig. 6.8 (b). The experimental data are well described by the $\cos^2(\alpha - \alpha_0)$ dependence (see eq. 3.42), which reflects the well-known dipole characteristic of the linear scattering intensity of the long-axis plasmon resonance mode [29] [77]. The orientation of the long-axis of the nanorod (red line) is determined to $\alpha_0 = 160^\circ$ in the coordinate system of x-y sample plane defined in fig. 6.1.

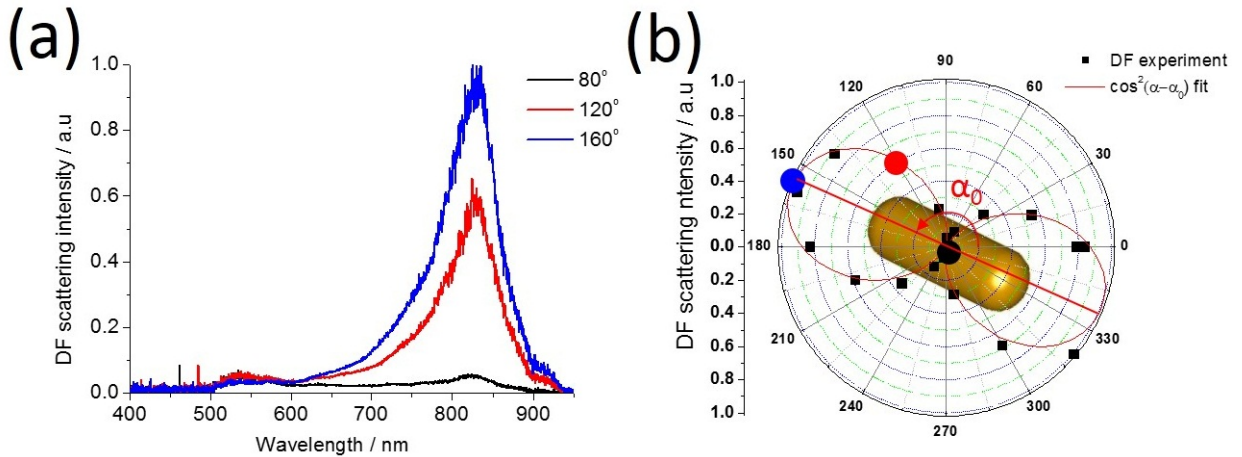


Figure 6.8: DF scattering spectroscopy of a single nanorod with specified dimensions of $39 \times 155 \text{ nm}^2$, which is immersed in refractive index matching oil. (a) DF scattering spectra recorded with an angle α between the linear excitation polarization and the long axis of the nanorod at 80° , 120° , and 160° . (b) Polar plot of the integrated DF scattering intensity of the long-axis plasmon resonance mode as a function of α . The corresponding fit to the $\cos^2(\alpha - \alpha_0)$ dependence is also shown.

6.4.3 Single nanorod characterization by SHG experiments

As for the nanosphere case, a whole set of experiments for a single nanorod consists of the DF scattering spectrum, the polarization-resolved DF scattering intensity, the SHG spectrum,

the polarization-resolved SHG intensity, and the SHG IAC trace measurement. Based on the linear DF scattering spectroscopy, individual nanorods with long-axis plasmon resonance bands within the spectral range of our in-focus excitation laser spectrum were selected from the inhomogeneous size distribution of nanorods of the purchased samples.

Fig. 6.9 (a) shows the DF scattering spectrum of a single nanorod selected from the nanorod 800 sample. The observed resonance band is well described by the fit to a Lorentzian line (purple curve, see the square of eq. 3.60) with $\lambda_{res} \approx 880$ nm and $\Delta\omega = (87 \pm 4)$ nm. Using eq. 3.63, the corresponding dephasing time is $T_2 = (9.8 \pm 0.2)$ fs. Comparing these values to those obtained from the single nanorod 800 shown in fig. 6.8, there are no big differences. Compared to the ensemble spectrum shown in fig. 6.7, the resonance wavelength of the nanorod 800 selected here is red-shifted with respect to the center wavelength of the inhomogeneously broadened ensemble extinction spectrum. By taking into account the red-shift of 180 nm when replacing the aqueous environment of the nanorod with oil, it indicates that the dimension and/or the aspect ratio for this particular nanorod is smaller than the respective mean values specified by the manufacturer. Because of the efficient plasmon resonance excitation with our laser pulses, the average power incident on the nanorod can be lower for SHG experiments than used for the nanosphere SHG experiments. The SHG spectra measured for the same selected nanorod 800 (black curve) and for a KDP crystal (blue curve) are also shown in fig. 6.9 (a). In contrast to the nanosphere cases, the peak of the SHG spectrum of the nanorod is red-shifted and the spectral width is narrowed when compared to that of the SHG spectrum of the KDP crystal. The center wavelength of the SHG spectrum of the nanorod amounts to (436 ± 4) nm, which corresponds to approximately twice the resonance frequency of its linear DF scattering spectrum. This observation indicates that the long-axis plasmon resonance observed in the linear DF scattering spectrum strongly affects its SHG spectrum.

Fig. 6.9 (b) shows the normalized polarization-resolved DF scattering intensity of the long-axis plasmon mode and the SHG intensity recorded on the same selected nanorod 800 as a function of the angle α between the linear excitation field and the long axis of the nanorod, which are well described by the $\cos^2(\alpha - \alpha_0)$ and $\cos^4(\alpha - \alpha_0)$ dependencies (see eq. 3.42 and eq. 3.43), respectively. For the measured DF scattering and SHG intensities, the orientation angles α_0 were independently determined to be $(19.6 \pm 0.6)^\circ$ and $(19.2 \pm 1.2)^\circ$, respectively. This observation provides not only an evidence for the presence of a single nanorod in this experiment, but also confirms the fact that the SHG is maximized when the excitation field is polarized parallel to the linear plasmon resonance mode of the long-axis of the nanorod.

The dependence of the SHG intensity on the average excitation power is shown in the log-log plot in the insert of fig. 6.9 (c). The linear fit (red curve) to the experimental data (black squares) results in a slope of (1.9 ± 0.2) counts/(s μ W), which agrees well with the expected quadratic dependence of the SHG signal on the average excitation power (see eq. 3.26). It also indicates

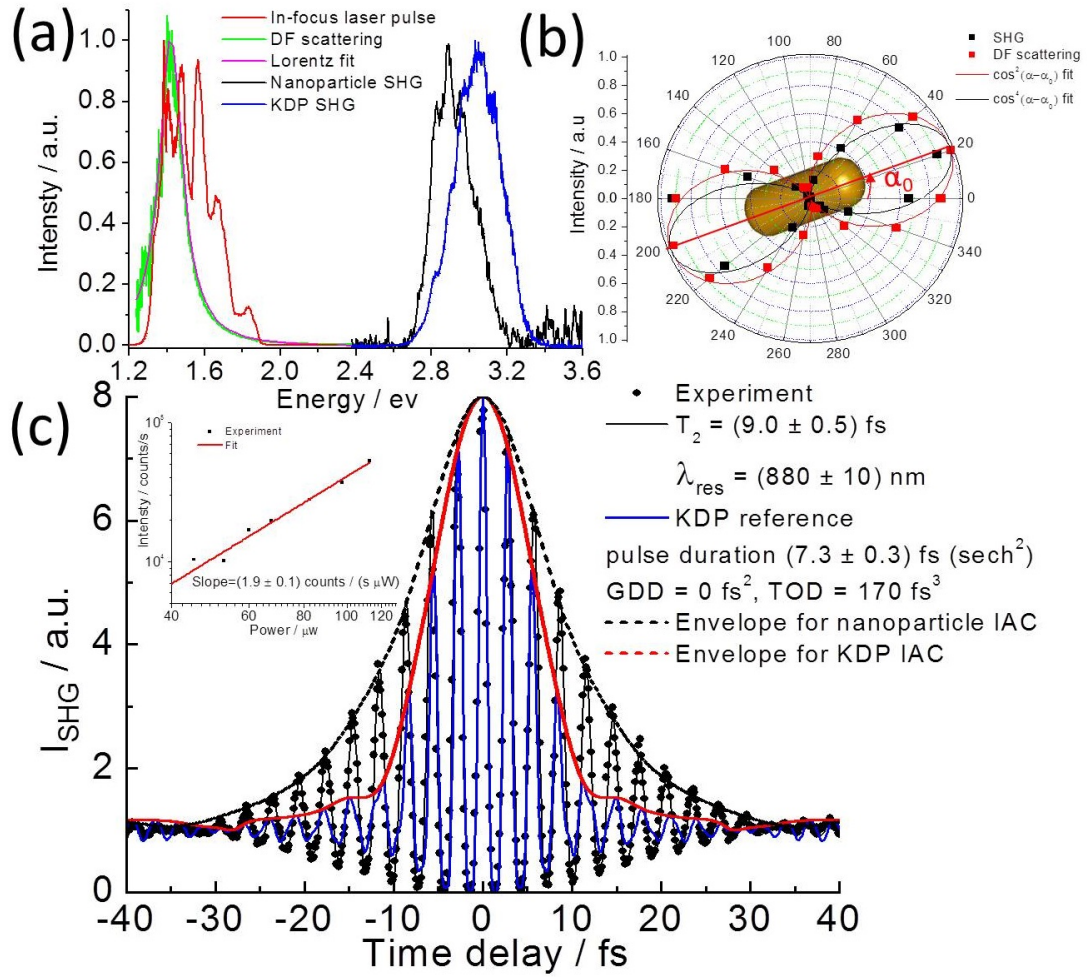


Figure 6.9: (a) Measured DF scattering spectrum (green curve) and the corresponding fit to a Lorentzian line shape (purple curve) are shown together with the SHG spectrum of the same single nanorod 800 (black curve) in oil. The SHG spectrum of a KDP crystal (blue curve) and the in-focus laser spectrum (red curve) are also shown for reference. (b) Normalized DF scattering (red symbols) and SHG intensity (black symbols) polar plots for the same nanoparticle together with fits to eq. 3.42 (red curve) and eq. 3.43 (black curve), respectively. (c) Measured SHG IAC trace (black squares) of the same nanoparticle and the simulated SHG IAC traces for the instantaneous response of a KDP crystal (blue curve) and for the plasmon resonance enhanced SHG of a nanoparticle with $T_2 = (9.0 \pm 0.5) \text{ fs}$ and $\lambda_{\text{res}} = (880 \pm 10) \text{ nm}$ (black curve) using an in-focus pulse with a duration of $(7.3 \pm 0.3) \text{ fs}$ (sech^2) and residual dispersion values of $\text{GDD} = 0 \text{ fs}^2$ and $\text{TOD} = 170 \text{ fs}^3$. The upper envelopes for the simulated SHG IAC traces of the KDP (red dash curve) and for the nanorod (black dash curve) are shown. The inset shows the log-log plot of SHG intensity (black squares) as a function of average excitation laser power at the sample. The red line shows the best fit to the experimental data with a slope of $(1.9 \pm 0.1) \text{ counts}/(\text{s } \mu\text{W})$. The average powers used in the SHG experiments shown in (a), (b), and (c) are $30 \mu\text{W}$, $25 \mu\text{W}$, and $25 \mu\text{W}$, respectively.

that an additional third-order or an higher-order nonlinear process does not contribute to the measured signal. Fig. 6.9 (c) shows the measured SHG IAC trace of the same single nanorod 800 (black squares), which is obtained by averaging 15 individual SHG IAC traces of the same nanorod in order to increase the S/N. The ratio of 8:1 between the SHG intensities measured at time delays zero and ± 40 fs also confirms that a two-photon excitation process was observed. The simulated SHG IAC trace for the plasmon resonance enhanced SHG (black curve), which best fits the measured SHG IAC trace of the nanorod, is also shown. Here, achieving minimal residuals was served as a criterion for obtaining the best fitting. A very good agreement between experimental and simulated SHG IAC traces is obtained for $T_2 = (9.0 \pm 0.5)$ fs and $\lambda_{res} = (880 \pm 10)$ nm. For reference, the simulated SHG IAC trace for the instantaneous material response of a KDP crystal (blue curve) with our in-focus laser pulse of 7.3 fs ($sech^2$) and residual dispersion values of $GDD=0$ fs^2 and $TOD = 170$ fs^3 is also shown. For the clarity of the presentation, only the upper envelopes of the simulated SHG IAC traces of the nanorod (black dash curve) and of the KDP crystal (red dash curve) are shown. Clearly one can observe that the SHG IAC trace of the single gold nanorod is broadened with respect to the corresponding simulated SHG IAC trace of the instantaneous KDP response. The plasmon dephasing time and resonance wavelength extracted from this time-domain SHG IAC experiment are in good agreement with $T_2 = (9.8 \pm 0.2)$ fs and $\lambda_{res} \approx 880$ nm, respectively, retrieved from the linear DF scattering spectrum of this nanorod. This consistency clearly demonstrates that a common driven damped harmonic oscillator model can explain our experimental results in both the linear and the second-order LSPR enhanced scattering processes.

Experiments for a smaller single nanorod from the nanorod 808 sample (10×40 nm^2) with a specified aspect ratio similar to that of the nanorod 800 sample are presented next. The DF scattering spectrum (green curve) of a selected single nanorod is shown in fig. 6.10 (a). The observed resonance band is well described by the fit to a Lorentzian line (purple curve, see the square of eq. 3.60) with $\lambda_{res} \approx 832$ nm and $\Delta\omega = (57 \pm 4)$ nm. Using eq. 3.63, the corresponding dephasing time is $T_2 = (12.7 \pm 0.2)$ fs. This long-axis plasmon resonance mode fully overlaps with the spectral bandwidth and coincides with the center frequency of our in-focus laser spectrum, which suggests an efficient resonance enhanced SHG in our experiments. Compared to the ensemble spectrum shown in fig. 6.7, the resonance wavelength and spectral bandwidth of the nanorod 808 selected here is red-shifted and narrower, respectively, with respect to the inhomogeneously broadened ensemble extinction spectrum. Compared to a DF scattering experiment for a single gold nanorod with $L_y \times L_x$ dimensions of approximately 20×80 nm^2 in oil with $\lambda_{res} = 827$ nm and $T_2 = 18$ fs reported in reference [29], the corresponding resonance wavelength of the nanorod selected here is similar, while our recorded dephasing time is shorter. Because of a possible aggregation of the nanorods in the ensemble experiments, no conclusion about the actual size of the selected single nanorod 808 can be drawn. The SHG

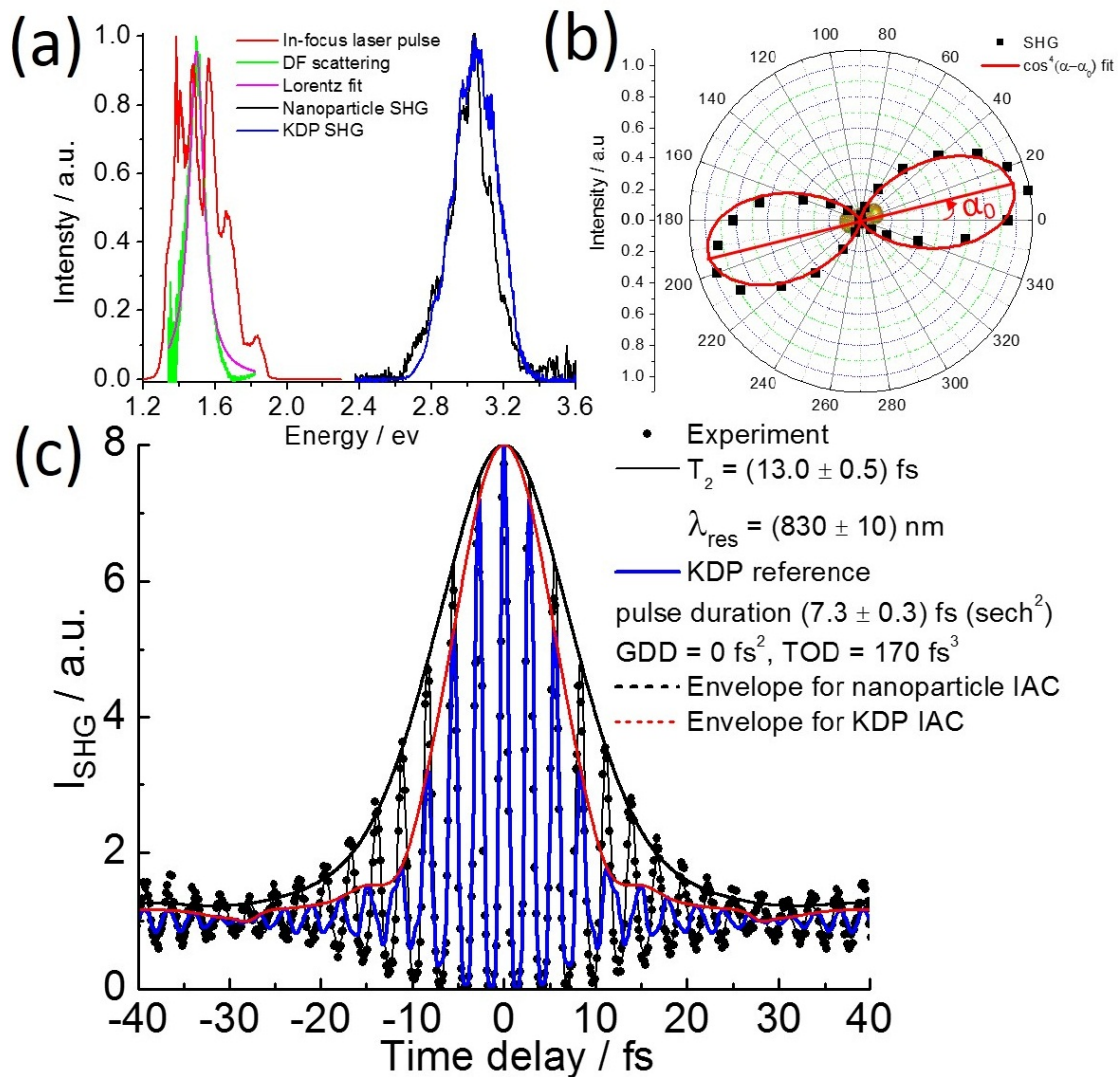


Figure 6.10: (A) Measured DF scattering spectrum (green curve) and the corresponding fit to a Lorentzian line-shape (purple curve) are shown together with the SHG spectrum of the same single nanorod 808 (black curve) in oil. The SHG spectrum of a KDP crystal (blue curve) and the in-focus laser spectrum (red curve) are also shown for reference. (b) Normalized SHG intensity (black symbols) polar plot for the same nanoparticle together with a fit to eq. 3.43 (red curve). (c) Measured SHG IAC trace (black squares) of the same nanorod and the simulated SHG IAC traces for the instantaneous response of a KDP crystal (blue curve) and for the plasmon resonance enhanced SHG of the nanorod with $T_2 = (13.0 \pm 0.5)$ fs and $\lambda_{res} = (830 \pm 10)$ nm (black curve) using an in-focus pulse with a duration of (7.3 ± 0.3) fs ($sech^2$) and residual dispersion values of GDD = $0 fs^2$ and TOD = $170 fs^3$. The upper envelopes for the simulated SHG IAC traces of KDP (red dashed curve) and of the nanorod (black dashed curve) are shown. The average powers used in the SHG experiments shown in (a), (b), and (c) are $42 \mu W$, $50 \mu W$, and $56 \mu W$, respectively.

spectra measured for the same nanorod (black curve) and for a KDP crystal (blue curve) are also shown in fig. 6.10 (a). The center wavelength of the SHG spectrum of the nanorod is at (413 ± 4) nm, which is approximately twice the resonance wavelength of its linear DF scattering spectrum. Also the bandwidth of the SHG spectrum is narrower than that of the SHG spectrum of KDP. Both observations indicate that this long-axis plasmon resonance observed in the linear DF scattering spectrum has a strong impact on its SHG spectrum.

Fig. 6.10 (b) shows the normalized SHG intensity (black squares) recorded for the same single nanorod as a function of the angle α between the linear excitation field and the long-axis of the nanorod. The SHG polar plot is well described by a $\cos^4(\alpha - \alpha_0)$ dependence (see eq. 3.43) for a two-photon induced scattering process. This observation provides an evidence for the presence of a single nanorod in this experiment. As for the nanorod 800 experiment, it was verified that the linear DF scattering intensity of the long-axis resonance mode also shows the dipole characteristic according to eq. 3.42 (not shown) and that its maximum intensity coincides with the maximum of the polarization-dependent SHG intensity, for which an orientation angle of $\alpha_0 = (12.0 \pm 0.6)^\circ$ was determined.

Fig. 6.10 (c) shows the measured SHG IAC trace of the same nanorod 808 (black squares), which is obtained by averaging 15 individual SHG IAC traces of the same nanorod in order to increase the S/N. The ratio of 8:1 between the SHG intensities measured at time delays zero and ± 40 fs also confirms that a two-photon excitation process was observed. The simulated SHG IAC traces for the plasmon resonance enhanced SHG (black curve), which best fits the measured SHG IAC trace of the nanorod, is also shown. Here, achieving minimal residuals was served as a criterion for obtaining the best fitting. A very good agreement between the experimental and the simulated SHG IAC traces is obtained for $T_2 = (13.0 \pm 0.5)$ fs and $\lambda_{res} = (830 \pm 10)$ nm. For reference, the simulated SHG IAC trace for the instantaneous material response of a KDP crystal with our in-focus laser pulse of 7.3 fs ($sech^2$) and residual dispersion values of $GDD=0$ fs^2 and $TOD = 170$ fs^3 are shown. For the clarity of the presentation, only the upper envelopes of the simulated SHG IAC traces of the nanorod (black dashed curve) and of a KDP crystal (red dash curve) are shown. Clearly one can observe that the SHG IAC trace of the single gold nanorod is broadened with respect to the simulated SHG IAC trace of the instantaneous KDP response. The plasmon dephasing time and the resonance wavelength extracted from this time-domain SHG experiment are in very good agreement with $T_2 = (12.7 \pm 0.2)$ fs and $\lambda \approx 832$ nm, respectively, as retrieved from the linear DF scattering spectrum of this nanorod. This clearly demonstrates that the common driven damped harmonic oscillator model can explain our experimental results in both the linear and the second-order LSPR enhanced scattering processes.

6.5 Summary of nanosphere and nanorod experiments

Table 6.5 summarizes the results of the combined studies using linear DF scattering, ensemble extinction, and SHG spectroscopies of the single gold nanospheres and nanorods described in sections 6.3 and 6.4, respectively. The linear DF scattering experiments on single nanoparticles confirm the inhomogeneous size distribution of nanospheres and nanorods in the purchased suspensions that results in ensemble dephasing time shorter than those expected for a single nanoparticle with specified mean dimensions (see eq. 3.64). The strong dependence of the plasmon dephasing time and resonance wavelength on the size and shape of the nanoparticle, which has previously been demonstrated by using linear DF scattering spectroscopy [29], could only be confirmed by experiments carried out on the single nanoparticle level. For the nanorods, we observed an increase of the extracted dephasing time when the resonance wavelength blue-shifts, whereas the dephasing time of the nanospheres was observed to decrease for more red-shifted resonance wavelengths. For nanorods with a similar aspect ratio, the nanorod with a smaller volume has a longer dephasing time and a blue-shifted resonance wavelength compared to the bigger nanorod. Furthermore, the extracted dephasing times for the nanospheres are much shorter than those of the nanorods. These dependencies are attributed to the increased radiation damping in nanoparticles of increased volume [29] (see also discussion in section 3.4.4).

Having established single nanoparticle plasmon characteristic by using the conventional DF scattering spectroscopy, the plasmon resonance enhanced SHG on the same nanoparticle was confirmed by polarization-resolved SHG experiments, SHG spectroscopy in the frequency-domain, and SHG IAC trace measurements in the time-domain. In the case of a single nanorod, the maximum SHG intensity is observed when the linear polarized excitation field is parallel to the long-axis plasmon resonance mode observed in the linear DF scattering spectrum.

Table 6.5: Summary of the plasmon information retrieved from single gold nanoparticles using linear DF scattering and SHG spectroscopies and from ensemble extinction spectroscopy of nanoparticles suspensions.

Name	Single nanoparticle DF scattering spectrum				SHG IAC		Ensemble dephasing time
	retrieved from experiments		values in literature [29]		measurements		
	T_2 / fs	λ_{res} / nm	T_2 / fs	λ_{res} / nm	T_2 / fs	λ_{res} / nm	T' / fs
nanosphere 80	4.2 ± 0.2	581	3.3	590	—	—	3.7 ± 0.2
nanosphere 125	2.5 ± 0.2	670	—	—	—	—	2.2 ± 0.2
nanorod 800	9.8 ± 0.2	880	—	—	9.0 ± 0.5	880 ± 10	9.2 ± 0.2
nanorod 808	12.7 ± 0.2	832	18	827	13.0 ± 0.5	830 ± 10	4.0 ± 0.2

For the single nanorods, our SHG IAC trace measurements directly demonstrated plasmon dephasing in the time-domain on the sub-14 fs time scale. Based on a driven damped harmonic

oscillator model and on the specific in-focus excitation pulse properties of our experiment, the simulated SHG IAC traces that best describe the experiments are used to extract the plasmon resonance properties from these SHG time-domain experiments. The excellent agreement between the resonance wavelengths and dephasing times obtained from the SHG IAC traces and the corresponding linear DF scattering spectra indicates that a common driven damped harmonic oscillator model can explain both the linear and the SHG scattering responses to the LSPR in a single gold nanoparticle. For nanospheres with resonance wavelengths outside the spectral bandwidth of our excitation pulses, the plasmon resonance enhanced SHG is negligible, and plasmon dephasing processes cannot be resolved in our time-domain SHG IAC trace measurements.

6.6 Gold nanodisk array experiments

In order to systematically study gold nanoparticles with well-defined sizes and shapes, the plasmon resonance properties of gold nanodisks of various diameters are investigated in this section. First, the extinction spectra of nanodisk ensembles with different dimensions were investigated. Second, the SHG images and spectra of single nanodisks were measured. Next, the SHG IAC trace measurements for each single nanodisk with few-cycle pulses were performed. Based on the driven damped harmonic oscillator model, the plasmon resonance properties of single nanodisks with different diameters obtained by linear extinction and SHG spectroscopies are compared.

6.6.1 Ensemble measurements of extinction spectra

Fig. 6.11 (a) shows extinction spectra of ensembles of nanodisks for different disk diameters in air measured with linear horizontal polarization excitation using FTIR microspectroscopy (dashed lines). Since the nanodisks have almost circular cross sections, the extinction spectra recorded with vertical linear polarization excitation are almost identical, and are not shown here. Each spectrum consists of a plasmon resonance band that is described by a resonance wavelength and bandwidth listed in table 6.6. One can observe that the peak extinction is increasing and the resonance wavelength is red-shifting with the increasing of the disk diameter. For the diameters larger than 120 nm, no obvious trend was observed. For each single nanodisk size, the simulated extinction spectra based on full MNPBEM (solid lines) are shown for comparison. One can observe that the center wavelengths of the simulated and experimental spectra nicely match, whereas for the nanodisks with diameters smaller than 120 nm, the bandwidths of the experimental extinction spectra are systematically larger than those retrieved from the simulated spectra. For the nanodisks 160, the opposite trend is observed. This discrepancy may be attributed to an inhomogeneous broadening effect in the experimental extinction spectra, which

is caused by size deviations from the designed dimensions of the manufactured nanodisks. The discrepancy of the bandwidth indicates that it is critical to implement SHG measurements on single nanodisks in order to retrieve the accurate plasmon resonance information.

DF scattering spectrum measurements of single nanodisks in the nanoarray sample was tried. Since the center to center distance between neighboring nanodisks is $2.0 \mu\text{m}$, the collection of the background scattered light from neighboring nanodisks made the observation of the resonance DF scattering spectrum difficult. Also for the large disks, the spectrum of the DF spectroscopy light source was not broad enough in order to cover the entire extinction spectra.

SHG spectroscopy of single nanodisks is implemented in a refractive index matching oil. The simulated scattering spectra of nanodisk 80, nanodisk 100, nanodisk 120, nanodisk 140, and nanodisk 160 in oil were also computed, as shown in fig. 6.11 (b). The excitation laser spectrum (black curve) is shown for reference. From these spectra, one can observe that with increasing diameter, the scattering cross section is increasing and the resonance wavelength is red-shifting. Compared to the simulated spectra in air (see fig. 6.11 (a)), the resonance wavelength is red-shifted because of the increased refractive index of the immersion medium. One can observe that the spectral overlap between the scattering spectrum and the excitation laser spectrum is increasing with the nanodisk diameter, and starts to decrease for the nanodisk 160.

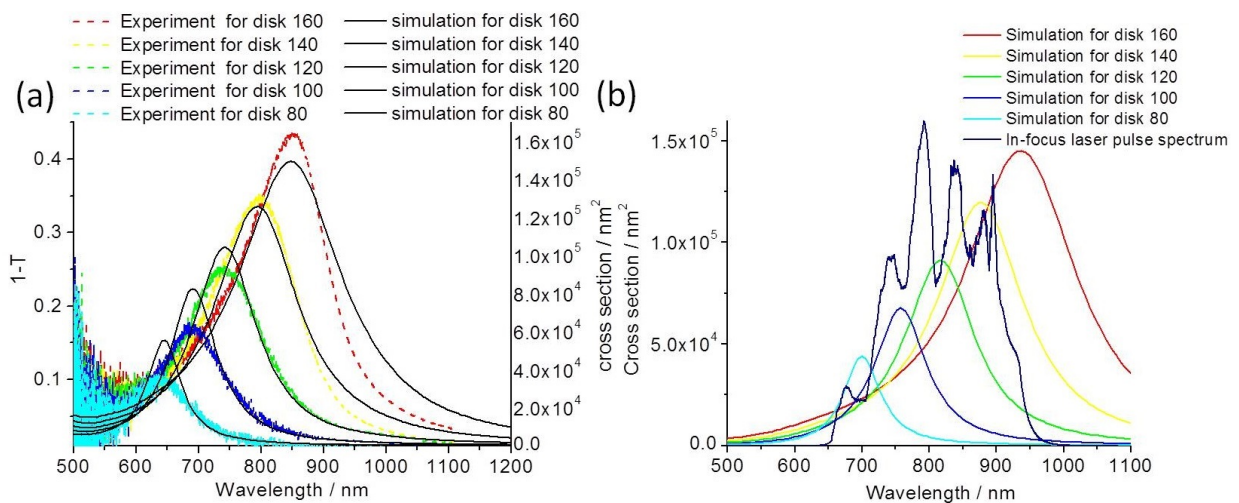


Figure 6.11: (a) Experimental extinction spectra (dashed curves) of ensembles of nanodisks and simulated extinction spectra (black curves) of single nanodisks with diameters of 80 nm, 100 nm, 120 nm, 140 nm, and 160 nm. (b) The corresponding simulated scattering spectra of single nanodisks in oil and the in-focus laser spectrum (black curve) are shown for comparison.

Table 6.6: The plasmon resonance parameters for nanodisks of different diameters extracted from experimental ensemble extinction spectra and from simulated extinction spectra for single nanodisks in air.

Name	Dimension	Extinction spectrum		MNPBEM simulation	
	diameter / nm	λ_{res} / nm	FWHM / nm	λ_{res} / nm	FWHM / nm
Disk 80	80	635	124 ± 4	646	67 ± 4
Disk 100	100	696	136 ± 4	691	91 ± 4
Disk 120	120	752	158 ± 4	744	124 ± 4
Disk 140	140	804	161 ± 4	797	164 ± 4
Disk 160	160	859	162 ± 4	846	206 ± 4

6.6.2 Single nanodisk characterization by SHG experiments

Single nanodisks with different diameters were investigated by SHG spectroscopy. Their arrangement in the nanodisk array is schematically shown in fig. 6.12 (a). Each nanodisk can be identified by the help of the orientation of the specially designed markers, which are located on the left side of the nanodisk array. In each row, the nanodisks were designed to have the same dimensions. The SHG image of these nanodisks is shown in fig. 6.12 (b). One can observe that the SHG intensities of the individual nanodisks along each row exhibit nearly the same brightness, which indicates that the reproducibility of the nanodisk dimension is good. To quantitatively analyze the SHG intensity of each nanodisk, a lateral SHG intensity profile for one column of nanodisks with different diameters along the white line shown in fig. 6.12 (b) is plotted in fig. 6.12 (c). From the intensity profile, one can observe that for increasing diameters, the SHG intensity first increases and then decreases for the nanodisk 160. Nanodisks with diameters 140 nm exhibits the strongest SHG signals. This size dependence of the SHG intensity on the nanodisk diameter follows that of the spectral overlap between the linear plasmon resonance band and our laser excitation spectrum used for the SHG experiments (see fig. 6.11 (b)). For nanodisks with a diameter below 80 nm, which exhibit low linear scattering cross sections and a small overlap between their resonance bands and the excitation laser spectrum, the SHG signals are too weak to be detected. The FWHM of the SHG intensity profile of the nanodisk with a diameter of 120 nm is (320 ± 10) nm, which indicates that a diffraction-limited spot is achieved at the focus of the high N.A. objective. The normalized polarization-resolved SHG intensity measured for a single nanodisk with a diameter of 160 nm is shown in the insert of fig. 6.12 (c). Due to its circular shape, the SHG polar plot of this nanodisk exhibits a near isotropic dependence on the angle of the incident linearly polarized excitation field.

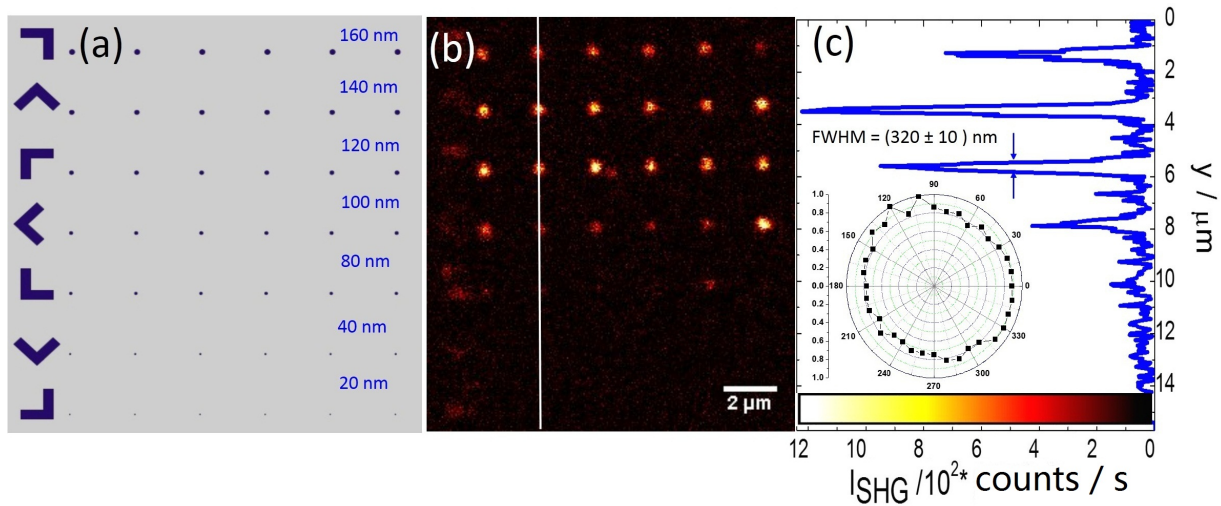


Figure 6.12: (a) Schematic layout of the nanodisk array consisting of single nanodisks arranged in rows of same diameters and columns with diameters ranging from 20 to 160 nm. The height of the nanodisk is fixed to be 25 nm. (b) SHG image of the nanodisk array which corresponds to (a). (c) The SHG intensity profile along the white line shown in (b). Insert: the normalized polarization-resolved SHG intensity for a single nanodisk with a diameter of 160 nm as a function of the incident angle of the linearly polarized excitation field. The average excitation laser powers used in the SHG experiments shown in (b) and the polar plot in (c) are 40 μ W and 130 μ W, respectively.

The normalized SHG spectra (black curves) measured for a single nanodisk with a diameter of 80 nm, 100 nm, 120 nm, 140 nm, and 160 nm are shown in figs. 6.13 (a), (c), (e), (g), and (i), respectively. The SHG spectrum of the KDP crystal (red curve) measured under the same experimental conditions is also shown here for reference. One can observe that the SHG spectrum is affected by the linear plasmon resonance wavelength of the nanodisk, which is also expected from the discussion in section 3.4.5. The center wavelength of the SHG spectrum, which is listed for each size in table 6.7, red-shifts and the shape of the SHG spectrum changes with the increasing of the nanodisk diameter. Compared to the SHG spectrum of a KDP crystal, the SHG spectra of nanodisks exhibit narrower bandwidths. Fig. 6.14 shows the absolute SHG intensity (black circles) obtained by the spectral integration as a function of the nanodisk diameter. Again, the same size dependence as observed for the lateral SHG intensity profile shown in fig. 6.12 (c) is obtained.

Figs. 6.13 (b), (d), (f), (h), and (j) show the measured SHG IAC traces (black squares) for the same nanodisks with diameters of 80 nm, 100 nm, 120 nm, 140 nm, and 160 nm, respectively. Each SHG IAC trace is obtained by averaging 10 to 20 individual SHG IAC traces of the same nanodisk in order to increase the S/N. The ratio of 8:1 between the SHG intensities measured at time delays zero and ± 40 fs also confirms that a two-photon excitation process was observed.

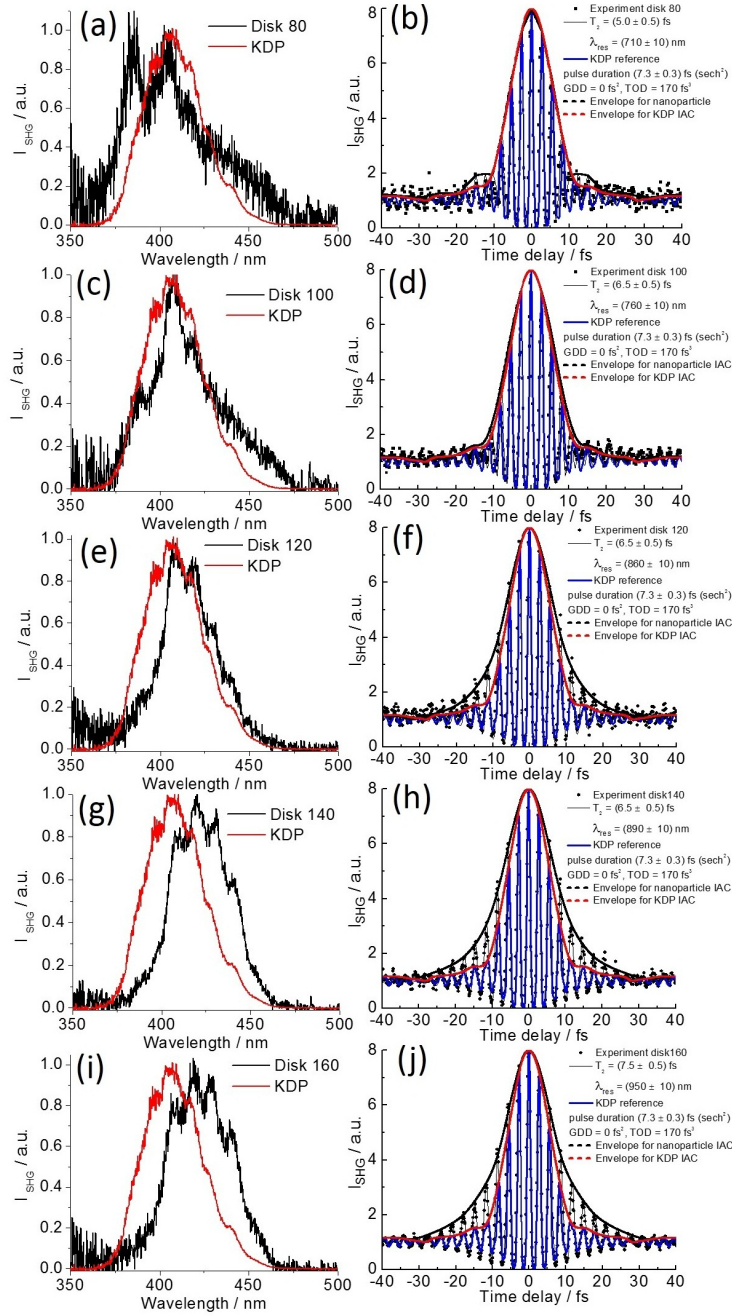


Figure 6.13: Measured SHG spectra (black curves) (a), (c), (e), (g), (i) and SHG IAC traces (black squares) (b), (d), (f), (h), (j) of single nanodisks with diameters of 80 nm, 100 nm, 120 nm, 140 nm, and 160 nm, respectively. The measured SHG spectrum of a KDP crystal (red curves) is shown for reference. For each nanodisk size, the simulated SHG IAC traces for both the plasmon resonance enhanced SHG with a dephasing time and a resonance wavelength that best fit the experimental data, as indicated in the figures and for the KDP reference using in-focus laser pulses of (7.3 ± 0.3) fs ($sech^2$) and residual dispersion values of $GDD = 0$ fs^2 and $TOD = 170$ fs^3 are also shown. The upper envelopes of both the simulated SHG IAC traces of the nanodisks (black dash curves) and for instantaneous KDP response (red dash curves) are also shown. The average excitation laser powers used for SHG spectra measurements is 35 μW and for the SHG IAC trace measurements range from 20 to 40 μW .

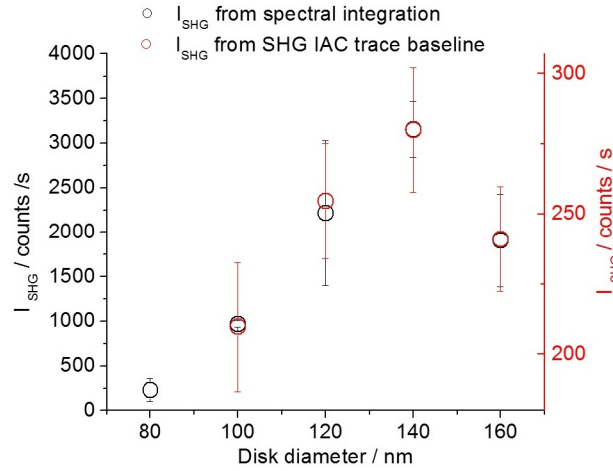


Figure 6.14: SHG intensities retrieved from the integration of SHG spectra (black circles) and from measured SHG IAC traces (red circles) at fixed time delay of ± 40 fs for single nanodisks with diameters of 80 nm, 100 nm, 120 nm, 140 nm, and 160 nm. The error bars represent the standard deviation obtained from 60 independent SHG spectra and from 10 to 20 independent SHG IAC traces.

Fig. 6.14 shows the SHG intensity retrieved from averaging SHG IAC traces (red circles) at a fixed time delay of ± 40 fs for each single nanodisk. This dependence of the SHG intensity on the nanodisk diameter is in a good agreement with the SHG intensity retrieved from the integration of the SHG spectrum (see fig. 6.14, black circles) and with the lateral SHG intensity profile (see fig. 6.12 (c)). For reference, the SHG IAC traces for the instantaneous response of a KDP crystal (blue curve) with our excitation laser pulses of (7.3 ± 0.3) fs (sech^2) and residual dispersion values of $\text{GDD} = 0 \text{ fs}^2$ and $\text{TOD} = 170 \text{ fs}^3$ are also shown. By comparing the upper envelopes of the SHG IAC traces for the instantaneous response (red dash curves) and for the individual nanodisks (black dash curves), one can observe a broadening effect due to the presence of plasmon dephasing in the nanodisks. The simulated SHG IAC traces for the plasmon resonance enhanced SHG (black curves), which best fit the respective experimental SHG IAC traces of the nanodisks are also shown. Very good agreements between the simulated and experimental SHG IAC traces are obtained for the T_2 and λ_{res} values listed in table 6.7. Their errors represent the respective range of values used for those simulated SHG IAC traces, for which the residuals are indistinguishable within our experimental noise levels.

Figs. 6.15 (a) and (b) compare the dependencies of the resonance frequency and the dephasing time on the disk diameter, respectively, retrieved from the simulated linear scattering spectra (black curve) with those extracted from the experimental SHG IAC traces (red symbols). The decrease of the simulated plasmon resonance frequency with an increasing nanodisk diameter is in good agreement with the experiment. Although the T_2 values between 5 and 8 fs retrieved from experiments are comparable with those obtained from simulations, the trend of the T_2 re-

Table 6.7: Summary of the plasmon resonance parameters retrieved from full MNPBEM simulations of linear scattering spectra and from the measured SHG IAC traces for the single nanodisks in oil. The center wavelengths retrieved from corresponding SHG spectra are also shown.

Name	SHG IAC measurements		SHG spectrum	MNPBEM simulation	
	T_2 / fs	λ_{res} / nm	λ_{center} / nm	T_2 / fs	λ_{res} / nm
Disk 80	5.0 ± 0.5	710 ± 10	405 ± 2	7.8 ± 0.2	700
Disk 100	6.5 ± 0.5	760 ± 10	409 ± 2	6.5 ± 0.2	758
Disk 120	6.5 ± 0.5	860 ± 10	419 ± 2	6.1 ± 0.2	821
Disk 140	6.5 ± 0.5	890 ± 10	423 ± 2	5.3 ± 0.2	885
Disk 160	7.5 ± 0.5	950 ± 10	426 ± 2	5.0 ± 0.2	949

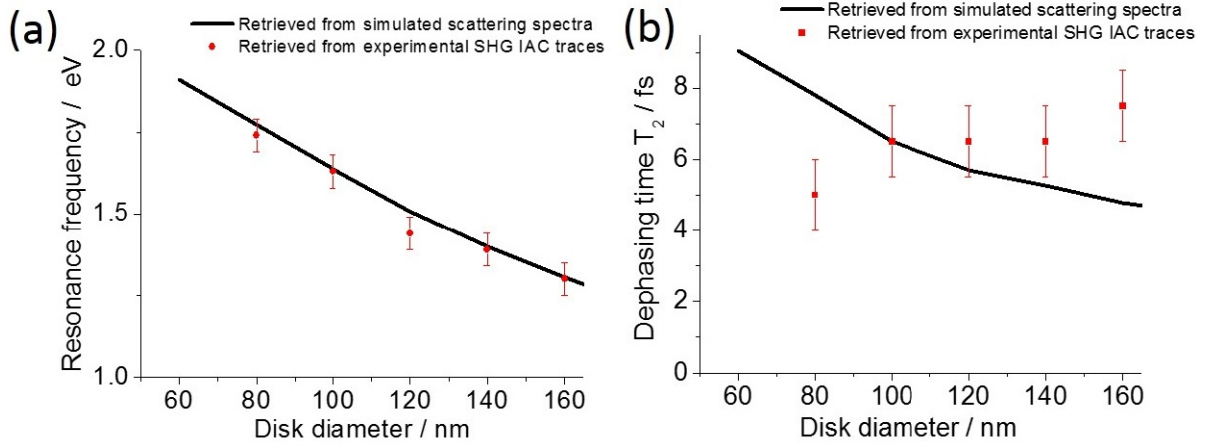


Figure 6.15: Dependence of the plasmon resonance frequency (a) and of the dephasing time (b) retrieved from experimental SHG IAC traces (red dots) and from simulated linear scattering spectra (black curves) for the single nanodisk on their nanodisk diameter. The error bars represent the range of values used for those simulated SHG IAC traces, for which the residuals are indistinguishable within our experimental noise levels.

retrieved from simulated linear scattering spectra versus the nanodisk diameter is not reproduced by the T_2 extracted from SHG IAC trace measurements. For nanodisk diameters bigger than 100 nm, the dephasing times are longer than the simulated ones. For a diameter smaller than 100 nm, the dephasing time is shorter than the simulated one. It is worthy noting that the dependence of T_2 retrieved from a simulation of linear scattering spectra on the nanodisk diameter is qualitatively confirmed by the observed trend of the reciprocal bandwidth retrieved from an

ensemble extinction spectrum listed in table 6.6. To resolve this discrepancy between the simulated and experimental trends of T_2 versus the nanodisk diameter, further investigations are needed.

6.7 Gold nanorectangle array experiments

The plasmon resonance properties of well-defined nanorectangles, which can be tuned by varying the ratio between the length L_x and the width L_y are studied in this section. The same set of experiments as used for the nanodisk array has been performed.

6.7.1 Ensemble measurements of extinction spectra

Fig. 6.16 (a) shows the extinction spectra (solid lines) of the ensemble of the nanorectangles of different sizes measured in air with the linearly polarized excitation parallel to the long axis of the nanorectangles using FTIR microspectroscopy. The corresponding MNPBEM simulations of the extinction spectra (black line scatters) for the single nanorectangles are also shown for comparison. Each spectrum exhibits a resonance band that is described by a resonance wavelength and a bandwidth, which are listed in table 6.8. In both the experimental and the simulated spectra, the same trends for the resonance wavelength and for the peak extinction versus the aspect ratio (L_x/L_y) are observed. With increasing aspect ratio, the resonance wavelength of the nanorectangle red-shifts and the peak extinction decreases. Except for the nanorectangle 100×100, the resonance wavelength of the simulated extinction spectrum is in reasonable agreement with the experimental value. No obvious trend for the resonance bandwidth versus the aspect ratio is observed in the ensemble extinction spectra, whereas the corresponding simulations for a single nanorectangle suggest a decrease of the bandwidth with an increasing aspect ratio. In addition, the bandwidth values retrieved from the simulations are systematically smaller than those observed in the ensemble extinction spectra. As in the case of the nanodisks (see section 6.6), this discrepancy may be attributed to the inhomogeneous spectral broadening present in ensemble measurements, which was caused by the deviations from the designed dimensions of the individually manufactured nanorectangles. This discrepancy indicates that single nanoparticle measurements are required in order to retrieve the accurate plasmon resonance information. For the same reasons that prevented DF scattering spectroscopy of the single nanodisks, DF scattering spectra of single nanorectangles could not be measured.

Since the SHG spectroscopy of the single nanorectangles is implemented in a refractive index matching oil, the simulated scattering spectra of these nanorectangles in oil were also computed, which are shown in fig. 6.16 (b). The excitation laser spectrum (black curve) is also shown for reference. Compared to the simulated spectra in air (see fig. 6.16 (a)), the resonance wavelength is red-shifted because of the increased refractive index of the immersion

medium. As in air, the peak scattering cross section is decreasing and the resonance wavelength is red-shifting with an increasing aspect ratio.

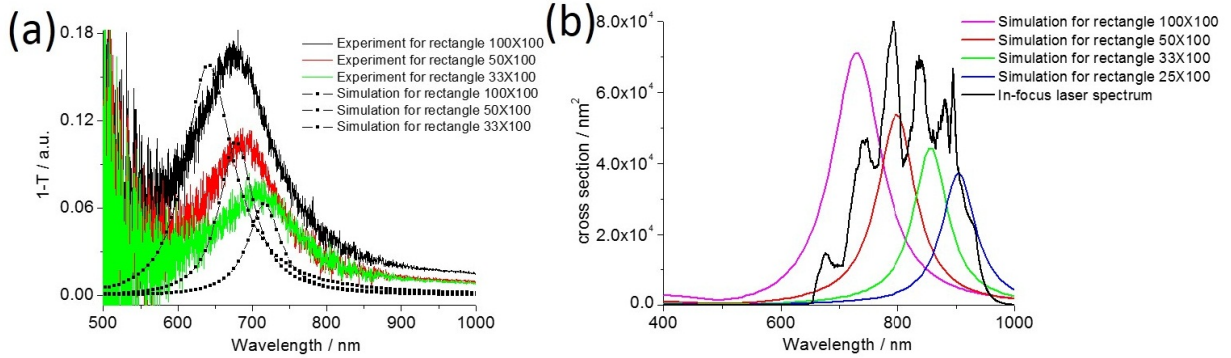


Figure 6.16: (a) Experimental extinction spectra (solid curves) of ensembles of nanorectangles and simulated extinction spectra for single nanorectangles (black line scatters) with dimensions of $100 \times 100 \text{ nm}^2$, $50 \times 100 \text{ nm}^2$, and $33 \times 100 \text{ nm}^2$ in air. (b) The corresponding simulated scattering spectra of single nanorectangles in oil and the in-focus excitation laser spectrum (black curve) are shown. The linear polarization of the excitation field for both the experimental and the simulated spectra is oriented along the long axis of the nanorectangles.

Table 6.8: The plasmon resonance parameters extracted from the experimental extinction spectra of ensembles of nanorectangles and from the simulated extinction spectra of single nanorectangles of different aspect ratios in air.

Name	Dimension	DF scattering spectrum		MNPBEM simulation	
	$L_y \times L_x / \text{nm}^2$	$\lambda_{\text{res}} / \text{nm}$	FWHM / nm	$\lambda_{\text{res}} / \text{nm}$	FWHM / nm
Rectangle 33 X 100	33 X 100	711	134 ± 4	720	55 ± 4
Rectangle 50 X 100	50 X 100	685	132 ± 4	681	58 ± 4
Rectangle 100 X 100	100 X 100	680	144 ± 4	642	78 ± 4

6.7.2 Single nanorectangle characterization by SHG experiments

Polarization-resolved SHG imaging of single nanorectangles with identical dimensions but orthogonal orientations in the x-y sample plane was performed. Figs. 6.17 (a) and (e) define the orientations of the nanorectangle 50x100 and the nanorectangle 100x50 in the sample plane. Figs. 6.17 (b) and (f) show the SHG images recorded with the excitation polarization parallel to the x-axis. Figs. 6.17 (c) and (g) show the SHG images recorded with the excitation polarization parallel to the y-axis. No SHG was observed when the linear polarization of the excitation field is perpendicular to the long axis of the nanorectangle. When the linear polarization of the

excitation field is parallel to the long axis of the nanorectangle, a strong plasmon resonance enhanced SHG is observed, which is expected from the large overlap between the simulated linear scattering spectrum and the in-focus excitation laser spectrum (see fig. 6.16 (b)). The SHG intensities of those nanorectangles with an identical size arranged in one row were observed to be the same. This observation indicates that the reproducibility of the nanorectangle dimension is good. The SHG intensity profiles along the red and blue lines for the single nanorectangle 50×100 and the nanorectangle 100×50 are shown in figs. 6.17 (d) and 6.17 (h), respectively. When the linear excitation field is polarized parallel to the short axis, no SHG is observed, which is explained by the inefficient nonresonant excitation of the short-axis plasmon resonance centered at 520 nm with our excitation laser pulses. One can also observe that the SHG intensities of these two orthogonal nanorectangles are almost the same when the polarization of the excitation field is oriented parallel to the long axis of the nanorectangles. This result also indicates that the fabrication accuracy of the single nanorectangle dimensions is high.

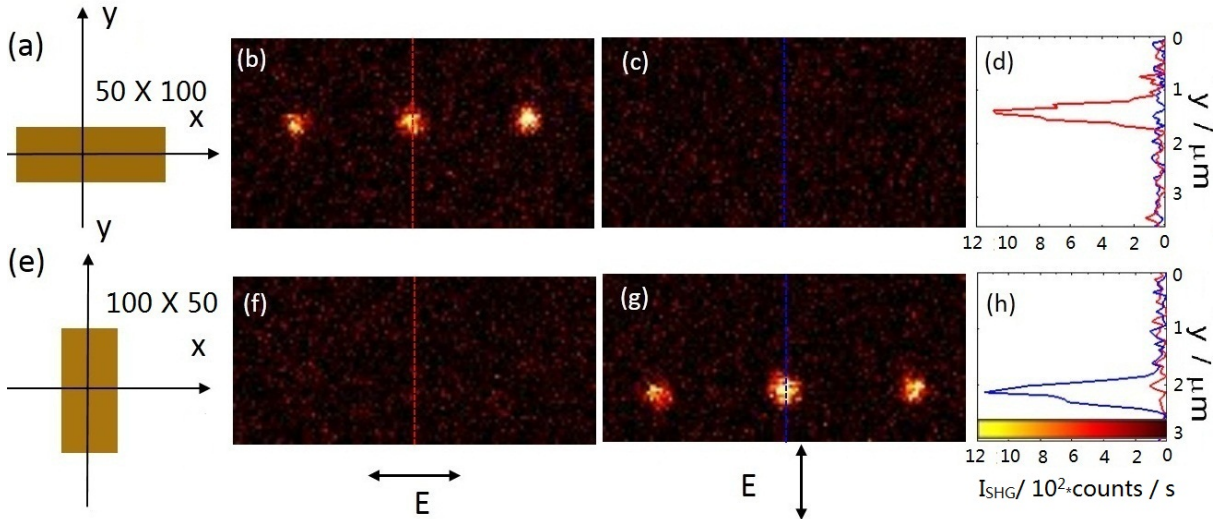


Figure 6.17: Schematic of the orientation of a single nanorectangle 50×100 (a) and of a nanorectangle 100×50 (e) in the x-y sample plane. SHG images of a row of three identical nanorectangles 50×100 recorded with a linearly polarized excitation field (E) parallel (b) and perpendicular (c) to the x-axis. SHG images of a row of three identical nanorectangles 100×50 recorded with a linearly polarized excitation field parallel (f) and perpendicular (g) to the x-axis. SHG intensity profiles along the red and blue dashed lines shown in the images for a single nanorectangle 50×100 (d) and for a nanorectangle 100×50 (h). The average excitation power used for this SHG experiment is $40 \mu\text{W}$.

The normalized polarization-resolved SHG intensities measured for two orthogonally oriented nanorectangles of the same dimensions are shown in fig. 6.18. The SHG polar plots for a single nanorectangle 25×100 (black squares) and for a single nanorectangle 100×25 (red squares) clearly follow two orthogonal dipole patterns, which are within the experimental errors

well described by the simulations for $\cos^4(\alpha - 0^\circ)$ (black curve) and $\cos^4(\alpha - 90^\circ)$ (red curve) according to eq. 3.43, respectively.

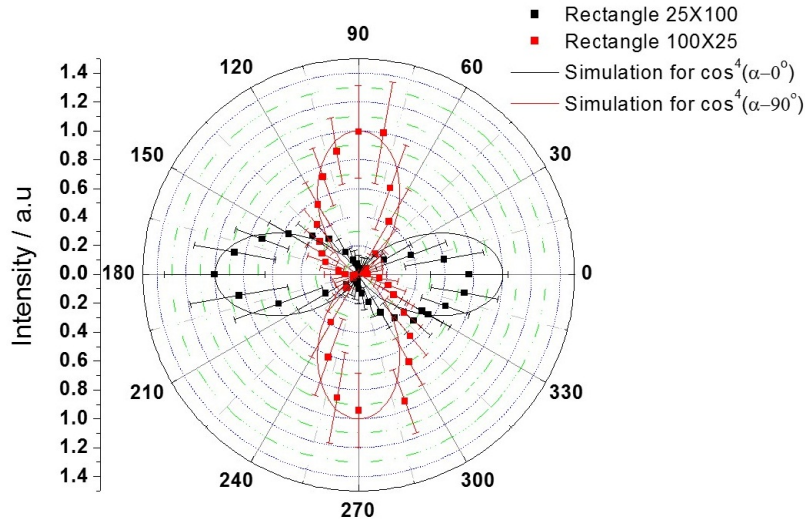


Figure 6.18: Normalized SHG intensity polar plots for the single nanorectangle 25×100 (black squares) and for the nanorectangle 100×25 (red squares) together with the respective simulations according to eq. 3.43 (black and red lines). The error bars represent the standard deviation of the fluctuation of the SHG intensity time trace. The excitation average power used for the SHG imaging is $40 \mu\text{W}$.

The normalized SHG spectra measured for single nanorectangles with $L_y \times L_x$ dimensions of 25×100 , 33×100 , 50×100 , and $100 \times 100 \text{ nm}^2$ and with linearly x-polarized excitation fields (black curves) are shown together with the normalized SHG spectra measured for their corresponding single nanorectangles with orthogonal orientations in the x-y sample plane and with linearly y-polarized excitation fields (blue curves) in figs. 6.19 (a), (d), (g), and (j), respectively. The SHG spectrum for the KDP crystal (red curve) is also shown here for reference. One can observe that the SHG spectra are mostly reproduced when nanorectangles of the same dimensions are orthogonally oriented to each other and the excitation polarization is oriented along long axis of the nanorectangles. The discrepancies between the SHG spectra observed in (a) and (j) are attributed to deviations of the manufactured dimensions. One can observe that the aspect ratio of the nanorectangle has a strong effect on its SHG spectrum. The center wavelength of the SHG spectrum of each nanorectangle, which is listed in table 6.9, red-shifts with an increasing aspect ratio of the nanorectangle, whereas its corresponding spectral bandwidth narrows. Compared to the SHG spectrum of the KDP reference, the SHG spectra of the nanorectangles exhibit narrower bandwidths.

The SHG IAC traces for the rectangle 25×100 , rectangle 33×100 , rectangle 50×100 , and rectangle 100×100 (black squares) measured with the polarization of the excitation field oriented along the long axis of the nanorectangles are shown in figs. 6.19 (b), (e), (h), and (k),

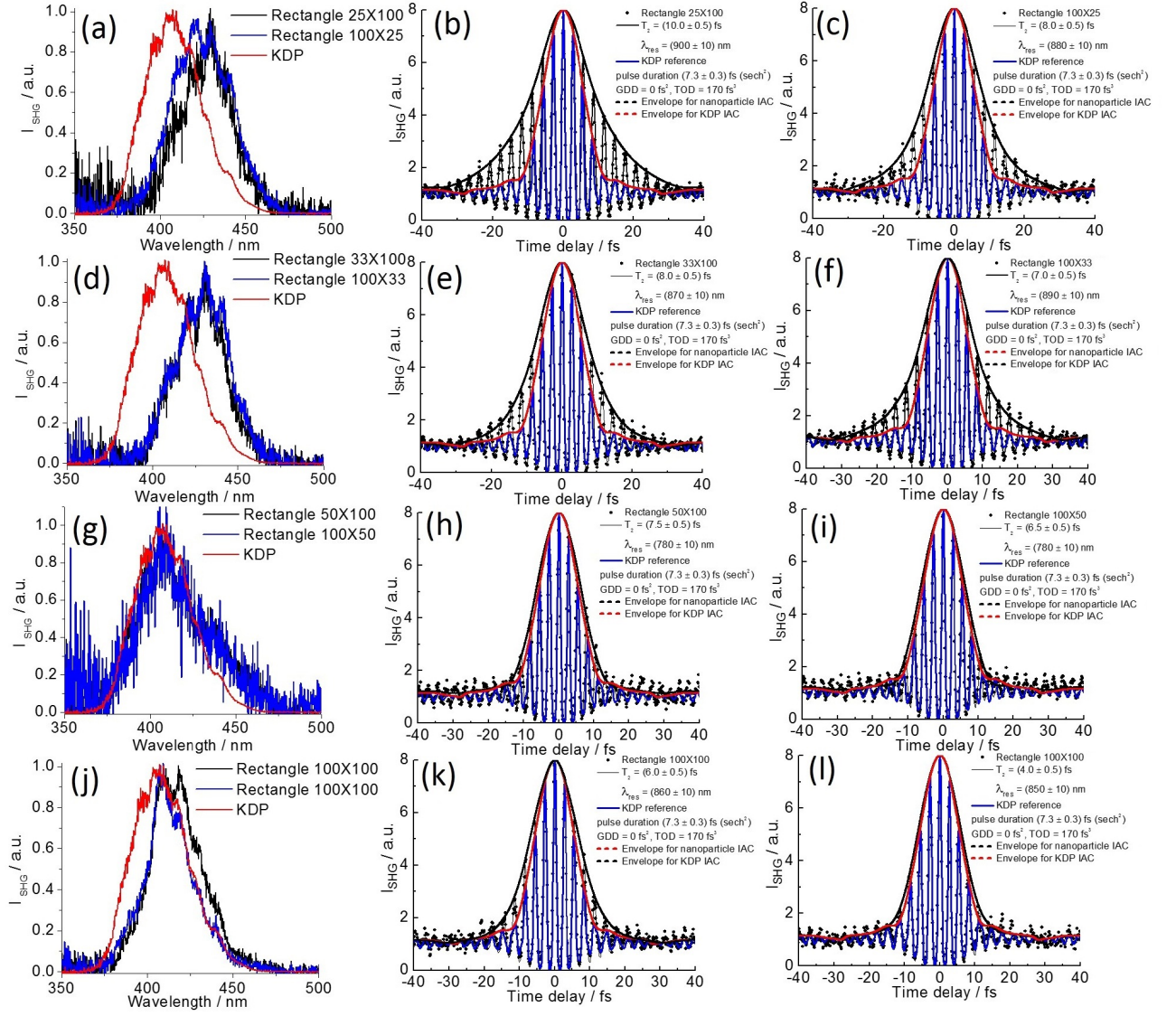


Figure 6.19: Normalized SHG spectra for single rectangles (a) 25×100 , 100×25 , (b) 33×100 , 100×33 , (c) 50×100 , 100×50 , and for square (d) 100×100 measured in oil with linearly x-polarized (black curves) and y-polarized (blue curves) excitation fields. The measured SHG spectrum of a KDP crystal (red curves) is shown here for reference. The SHG IAC traces (black dots) of single rectangles (b) 25×100 , (e) 33×100 , and (h) 50×100 , (k) 100×100 measured with an x-polarized excitation field. (c), (f), (i), (l): The SHG IAC traces measurements for the corresponding orthogonally orientated nanorectangles. For each single nanorectangle, the simulated SHG IAC traces for the KDP reference (blue curves) and for the plasmon resonance enhanced SHG with dephasing times and resonance wavelengths that best fit the experimental curves (black curves), using in-focus laser pulses of (7.3 ± 0.3) fs ($sech^2$) with residual dispersion values of $GDD=0$ fs² and $TOD = 170$ fs³ are shown. The upper envelopes for both simulated SHG IAC traces for the nanorectangles (black dashed curves) and for the instantaneous KDP response (red dashed curves) are also shown. The excitation average laser powers for the SHG spectrum measurements is $35 \mu\text{W}$ and used for the SHG IAC trace measurements range from 20 to $40 \mu\text{W}$.

respectively. The SHG IAC traces of the orthogonally oriented rectangle 100×25 , rectangle 100×33 , rectangle 100×50 , and rectangle 100×100 (black squares) measured with the polarization of excitation field oriented along the long axis of the nanorectangles are shown in figs. 6.19 (c), (f), (i), and (l), respectively. The SHG IAC traces of the nanorectangles are obtained by averaging 10 to 20 individual SHG IAC traces of the same nanorectangle in order to increase the S/N. The ratio of 8:1 between the SHG intensities measured at time delays zero and ± 40 fs confirms that a two-photon excitation process was observed. For reference, the simulated SHG IAC trace for the instantaneous response of KDP (blue curves) using in-focus laser pulses of (7.3 ± 0.3) fs (*sech*²) and residual dispersion values of $GDD = 0$ fs² and $TOD = 170$ fs³ is also shown. By comparing the upper envelopes in the SHG IAC traces for the KDP response (red dashed curves) and for the nanorectangles (black dash curves), an increasing broadening with an increasing aspect ratio is observed, which is attributed to the increasing plasmon dephasing time and the resonance wavelength of the nanorectangles. In order to quantitatively analyze the plasmon resonance information, the simulated SHG IAC traces for plasmon resonance enhanced SHG (black curves), which best fit the respective experimental SHG IAC trace measurements, are also shown. The simulated SHG IAC traces describe the experimental SHG IAC traces well for the plasmon dephasing times and resonance wavelengths listed in table 6.9. The errors shown in the table represent the range of values used for those simulated SHG IAC traces, for which the residuals are indistinguishable within our experimental noise levels.

Table 6.9: Summary of the plasmon resonance parameters retrieved from full MNPBEM simulations of the linear scattering spectra and from the SHG IAC traces measured for the investigated single nanorectangles of a varying aspect ratio and of orthogonal orientations in oil. The center wavelengths extracted from the corresponding SHG spectra are also listed.

Name $L_y \times L_x / \text{nm}^2$	SHG spectrum	SHG IAC measurements		MNPBEM simulation	
	$\lambda_{\text{center}} / \text{nm}$	$\lambda_{\text{res}} / \text{nm}$	T_2 / fs	$\lambda_{\text{res}} / \text{nm}$	T_2 / fs
Rectangle 25X100	430 ± 2	900 ± 10	10.0 ± 0.5	906	12.5 ± 0.2
Rectangle 100X25	427 ± 2	880 ± 10	8.0 ± 0.5	906	12.5 ± 0.2
Rectangle 33X100	430 ± 2	870 ± 10	8.0 ± 0.5	855	10.7 ± 0.2
Rectangle 100X33	430 ± 2	890 ± 10	7.0 ± 0.5	855	10.7 ± 0.2
Rectangle 50X100	416 ± 2	780 ± 10	7.5 ± 0.5	802	8.4 ± 0.2
Rectangle 100X50	414 ± 2	780 ± 10	6.5 ± 0.5	802	8.4 ± 0.2
Rectangle 100X100	415 ± 2	860 ± 10	6.0 ± 0.5	732	5.5 ± 0.2
Rectangle 100X100	409 ± 2	850 ± 10	4.0 ± 0.5	732	5.5 ± 0.2

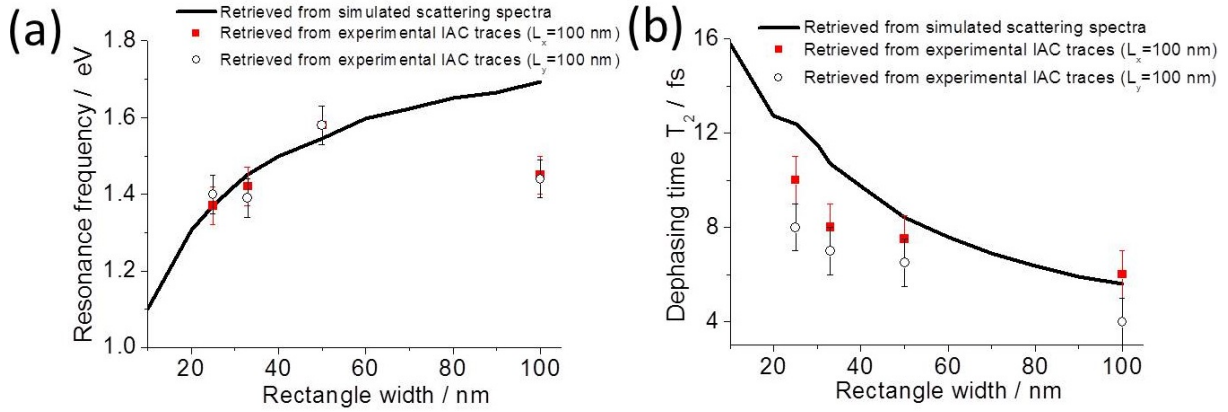


Figure 6.20: Dependence of the plasmon resonance frequency (a) and the dephasing time (b) retrieved from simulations of the linear scattering spectra (black lines) and from the experimental SHG IAC traces of single nanorectangles on their short-axis dimension when $L_x = 100$ nm (red squares) or $L_y = 100$ nm (black circles) are fixed. In all cases, linearly polarized excitation fields parallel to the long axis of the nanorectangles are used. The error bars represent the range of values used for those simulated SHG IAC traces, for which the residuals are indistinguishable within our experimental noise levels.

Figs. 6.20 (a) and (b) compare the dependencies of the resonance frequency and the dephasing time on the rectangle width, respectively, retrieved from the experimental SHG IAC traces (symbols) with those extracted from simulated linear scattering spectra (black lines). The increase of the plasmon resonance frequency for an increasing nanorectangle width (or for a decreasing aspect ratio) retrieved from experimental SHG IAC traces is in good agreement with the dependencies extracted from the simulated linear scattering spectra. The observed dependencies of the simulated and the experimental plasmon dephasing times on the nanorectangle width exhibit the same trend, where the dephasing time is decreasing with an increasing nanorectangle width. However, the dephasing times obtained from simulations of linear scattering spectra are systematically longer.

The case of the single rectangle 100×100 represents an exception. The SHG spectra of the two nanosquares measured with orthogonal excitation polarizations exhibit different center wavelengths beyond the experimental errors. In addition, the plasmon dephasing times retrieved from the corresponding experimental SHG IAC traces are also different beyond the experimental errors (see fig. 6.20 (b)), and their retrieved resonance wavelengths deviate most from those extracted from simulations of the linear scattering spectra (see fig. 6.20 (a)). These discrepancies indicate that either the investigated nanosquare has not a perfect square geometry or that its plasmon resonance enhanced SHG is very sensitive to the excitation field polarization orientation. This is not the case for nanorectangles, which only exhibit a strong SHG enhancement for the excitation parallel to the short-axis plasmon mode and no SHG for excitation perpendicular

to the long axis with our excitation laser pulses.

6.8 Summary of nanodisk and nanorectangle results

This chapter presented SHG microspectroscopies that systematically characterize the plasmon resonance properties of single nanoparticles with well-defined dimensions. The strong dependence of the SHG intensity on the diameter of a nanodisk and on the aspect ratio of a nanorectangle were observed to follow the dependence of the spectral overlap between the linear plasmon resonance band and the excitation laser spectrum. For the nanorectangles, the SHG intensity is confirmed to be strongly dependent on the linear polarization of the excitation laser pulse. As for a single nanorod, strong plasmon resonance enhanced SHG is observed only when the linear polarized excitation field is parallel to the long-axis plasmon resonance mode of the nanorectangle. For the nanodisk, the expected near isotropic dependence of the SHG intensity on the incident angle of the excitation field is confirmed. For nanodisks and nanorectangles, with a plasmon resonance wavelength outside our excitation laser pulse spectrum, the plasmon resonance enhanced SHG is negligible and the plasmon dephasing time cannot be resolved in our time-domain SHG IAC experiment.

Based on the driven damped harmonic oscillator model and the in-focus excitation pulse properties of our experiment, the simulated SHG IAC traces that best describe the experiments are used to extract the plasmon resonance properties from the SHG time-domain experiments. Tables 6.7 and 6.9 summarize the results of the combined studies using linear scattering spectrum simulations and experimental SHG IAC trace measurements of the single gold nanodisks and nanorectangles, as described in sections 6.6 and 6.7. When the diameter of the nanodisk or the aspect ratio of nanorectangle is increasing, the resonance wavelength retrieved from the SHG IAC trace measurements is red-shifted, which is in excellent agreement with values obtained from corresponding simulated linear scattering spectra. For the nanorectangles, the plasmon dephasing times retrieved from SHG IAC trace measurements exhibit the same increasing trend as obtained from two linear scattering spectrum simulations when the aspect ratio is increasing. However, the dephasing times obtained from the simulated linear scattering spectra are systematically longer. In analogy to the work on nanorods presented by Sönnichsen et al. [29], this dependence on the aspect ratio is attributed to the increased radiation damping in nanorectangles with increasing volume (see discussion in section 3.4.4). For the nanodisks, the dependence of the dephasing time retrieved from the experimental SHG IAC traces and from the simulated linear scattering spectra on the disk diameter do not match. To resolve this discrepancy, further experiments are required. Consequently, only for the investigated nanorectangles, we can confirm that a common driven damped harmonic oscillator model explains qualitatively the linear and the SHG responses to the LSPR in a single nanorectangle.

6.9 Summary and Conclusions

In this chapter, we systematically characterized the SHG responses of single gold nanoparticles with different shapes and sizes to the interaction with our tightly focused 7.3-fs pulses. By comparisons with the conventional linear scattering spectroscopy performed on the same nanoparticles, and with the simulations for the linear scattering spectrum of a plasmon resonance with a given resonance wavelength and dephasing time, the following conclusions can be drawn:

For the nanoparticle with an LSPR wavelength outside the excitation laser spectrum, the plasmon resonance enhanced SHG is negligible, and the dephasing processes cannot be time-resolved with our laser pulses. In these cases, the nanoparticle exhibits an SHG response similar to that of a nonresonant material (for example KDP), as was observed in the SHG experiments of single nanospheres.

As demonstrated for the nanorods, the nanodisks, and the nanorectangles, a strong plasmon resonance enhanced SHG is observed, where the SHG intensity strongly depends on the spectral overlap between the LSPR band and the excitation laser spectrum.

The dependence of the plasmon resonance enhanced SHG intensity on the incident angle of the linearly polarized excitation field follows that of an isotropic and a dipole scatterer for a disk and a rod (rectangle), respectively. These observations provide the evidence for the presence of single nanoparticles in our experiments.

As demonstrated for the single nanorods and nanorectangles, the SHG with our excitation laser pulses originates only when the linear polarized excitation field is parallel to their long-axis plasmon resonance modes observed in their polarization-resolved linear scattering spectra. From the direct comparison between the polarization dependencies of the LSPR induced linear and SHG scatterings, the polarization-dependent SHG intensity is demonstrated to exhibit a higher sensitivity to the morphology of the nanoparticle.

For all nanoparticles that show a plasmon resonance enhanced SHG, the effect of the size and the shape on the LSPR properties is directly observed in the time-domain SHG experiments. While the resonance wavelength retrieved from SHG IAC trace measurements are in good agreement with those obtained from simulated linear scattering spectra, the respective dephasing times only match in the nanorod and nanorectangle cases. Additional experiments are required in order to resolve the observed discrepancy in the nanodisk case. Consequently, only for the single nanorods and nanorectangles of different sizes and aspect ratios, we confirm that a common driven damped harmonic oscillator model for the LSPR in the nanoparticle can qualitatively explain both the linear scattering spectra in the frequency-domain and the SHG response in the time-domain.

To our best knowledge, this study is the first systematic experimental demonstration of

time-resolving the ultrashort plasmon dephasing in single gold nanoparticles by performing time-domain SHG experiments in combination with the linear scattering spectroscopy. The shortest and longest dephasing times that could be resolved by the SHG IAC trace measurements amount to (4.0 ± 0.5) fs for a single nanosquare ($100 \times 100 \text{ nm}^2$) and to (13.0 ± 0.5) fs for a single nanorod ($10 \times 40 \text{ nm}^2$). For a nanorod with a same aspect ratio but a larger volume, we experimentally confirmed the decrease of the plasmon dephasing time due to the expected increase of the radiation damping [29].

Studying of the ultrafast dynamics of localized surface plasmon resonances in a single nanohole in gold films

7.1 Motivation

Nanoholes with sizes smaller than the wavelength of the incident light in a metal film exhibit a wide variety of unexpected linear optical properties [81] [48] [82] [83] [49] [84] [14] [50] [85] [51]. Resonance bands in transmission and scattering spectra have been observed [48], [82] [83] [50] [51], which are assigned to LSPR modes of the electric field distribution around the nanohole with qualitatively similar resonance properties as a nanoparticle. Compared to the LSPR of a nanoparticle of similar size, the nanohole plasmon resonance was found to exhibit a broader spectral bandwidth, which indicates the existence of an additional decay channel to the plasmon resonance dephasing [83] [49] [51].

The polarization-resolved nonlinear optical properties of the single nanoholes with different shapes and symmetries were also reported by using SHG [10] and multi-photon emission [11] microscopies. However, systematical SHG studies of the size effect in the LSPR of the single nanoholes in the metal films and of their ultrafast dephasing dynamics have not been reported yet. The motivation of this work is to investigate the size-dependent SHG properties of a single rectangular nanohole and to test the feasibility of directly time-resolving the LSPR dephasing in a single nanohole by performing SHG-IAC trace measurements with our 7.3-fs focus excitation pulses.

While the applicability of Babinet's principle [12], which states that the polarization of the electric field incident on a nanocavity must be rotated by 90° in order to yield the same radiation pattern as from the complementary nanoparticle structure, has been previously experimentally demonstrated for linear optical frequency nanostructures and metamaterials with intrinsic resonance [13] [14] [54] [52] [53] [51], the question as to whether Babinet's principle can even be applied in nonlinear optical scattering measurements remains to be answered. The objective of

this work is the experimental demonstration of Babinet’s principle for SHG of a single rectangular nanohole in a thin gold film as a complementary nano-structure to the rectangular gold nanoparticle investigated in chapter 6.

In this chapter, we present the experimental study of LSPR properties of individual rectangular nanoholes of varying sizes in gold films using simulated linear transmission spectra, SHG spectroscopy in both frequency and time domains, and SHG imaging in combination with SHG polarization-resolved experiments in both forward- and epi-detection geometries.

7.2 Materials and methods

7.2.1 Microscope configurations

Since various experiments are discussed in this chapter, the details of the detection geometry, filters, and detectors of the different configurations of the NLO microscope are listed in table 7.1.

Table 7.1: The NLO microscope configurations for the detection geometry, filters, and detectors used for different experiments discussed in this chapter.

section	experiments	detection geometry	filters	detectors
7.4.1	SHG spectrum measurements	Epi	band-pass filter (Semrock, KFF01 405 nm/150 nm)	Spectrometer
7.4.2		Forward		
7.4.1	SHG image measurements	Epi	band-pass filter (Semrock, KFF01 405 nm / 150 nm) and short-pass filter (Omega 450 nm)	APD
7.4.2		Forward		
7.4.1	Polarization-resolved SHG intensity measurements	Epi	band-pass filter (Semrock, KFF01 405 nm / 150 nm) and short-pass filter (Omega 450 nm)	APD
7.4.2		Forward		
7.4.1	SHG IAC trace measurements	Epi	band-pass filter (Semrock, KFF01 405 nm / 150 nm) and short-pass filter (Omega 450 nm)	APD
7.4.2		Forward		
7.4.1	Polarization-resolved TPF intensity measurements	Epi	band-pass filter (Chroma, HQ 585 nm / 80 nm) and band-pass filter (Throlabs, FGB37)	APD

7.2.2 Gold nanohole array sample

The gold nanohole array sample was provided by our collaborator from the Weizmann Institute of Science. The scheme of the designed nanohole array is shown in fig. 7.1. The sample coordinate system (x-y) was defined. A nanohole array consists of single rectangular nanoholes with $L_y \times L_x$ dimensions of 50×50 , 50×100 , 50×150 , 50×200 , 50×250 , 50×300 , 50×350 , 50×400 , 50×450 , and $50 \times 500 \text{ nm}^2$. The edge-to-edge distance between two neighboring nanoholes is designed to be $15.0 \mu\text{m}$ in order to diminish the coupling possibility

between neighboring nanoholes. The Au films have thicknesses of 300 nm and 350 nm, which were evaporated onto a clean glass substrate ($10 \times 25 \text{ mm}^2$, thickness: #1a) under high vacuum conditions, with a measured roughness less than 1 nm. These rectangular nanoholes have been fabricated by a focused ion beam (FIB, FEI Helios Nano Lab 600i, DualBeam FIB/SEM) [10], which offers a precise and reproducible fabrication with a resolution down to 10 nm.

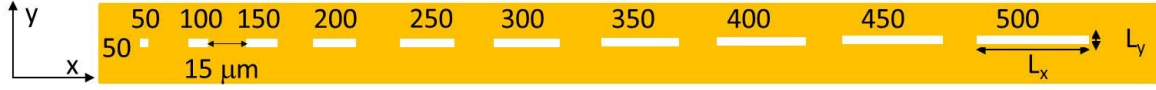


Figure 7.1: Schematic layout showing the arrangement of the rectangular nanohole array in the gold film consisting of nanoholes with $L_y \times L_x$ dimensions of 50×50 , 50×100 , 50×150 , 50×200 , 50×250 , 50×300 , 50×350 , 50×400 , 50×450 , and $50 \times 500 \text{ nm}^2$ manufactured by FIB. The nearest edge-to-edge distance between two neighboring nanoholes is $15.0 \mu\text{m}$. The thickness of the gold film is designed to be 300 or 350 nm.

7.2.3 Transmission spectrum simulation

The simulated transmission spectra of the rectangular nanoholes were provided by our collaborator from the Weizmann Institute of Science. These transmission spectra are simulated using a software package named Lumerical FDTD solutions. The simulations were performed in the same configurations as the experiments, glass-gold-air and glass-gold-oil configurations, where the illumination is from below through the glass substrate, and the collection is in the forward direction in air and in oil, respectively. The dielectric function used for the gold nanoparticle and glass substrate were also taken from literature [38] and [86], respectively. The wavelength-independent refractive index for the surrounding medium oil of 1.518 is assumed. Plane wave excitation with linear polarization was used.

7.2.4 Scanning electron microscope imaging

For the characterization of the actual dimensions of the manufactured nanoholes, the SEM images of different nanoholes in the array were measured using the same setup (FEI Helios NanoLab 600i, DualBeam FIB/SEM). The SEM images were also provided by our collaborator from the Weizmann Institute of Science. The SEM image of two rectangle holes, which have the nearest edge-to-edge distance of $14.96 \mu\text{m}$, is shown in fig. 7.2. As an example, a high resolution SEM image of one nanohole is shown in the inset. The length L_x , width L_y are determined to be 156.2 nm, 53.22 nm (aspect ratio AR: L_x / L_y), which has a deviation of 4.1% and 6.4% from the designed dimensions, respectively. The maximum deviation of both length and width from the designed dimensions were determined to be 7.7% and 6.3%, respectively,

by evaluation of the measured rectangular nanoholes with different dimensions measured by using SEM imaging.

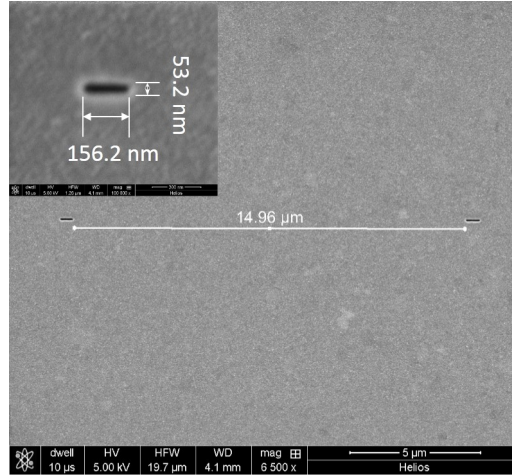


Figure 7.2: SEM image of the rectangular nanohole array made in a gold film (thickness = 300 nm). A high magnification image of one nanohole is shown in the inset with $L_x = 156.2$ nm and $L_y = 53.2$ nm. The nearest edge-to-edge distance between two neighboring nanoholes is $14.96 \mu\text{m}$.

7.3 Simulated transmission spectra of single rectangular nanoholes

Fig. 7.3 (a) shows the transmission spectra of single rectangular nanoholes for different sizes in 300-nm thick film (solid curves) simulated in air with linearly polarized excitation parallel to the short-axis of the rectangular nanohole. The corresponding simulated transmission spectra for single rectangular nanoholes in 350-nm thick film (dashed curves) are also shown for comparison. Each spectrum exhibits a resonance band that is described by the resonance wavelength and bandwidth, which are listed in table 7.2. In these simulated transmission spectra, the same trends for the resonance wavelength, the spectral bandwidth, and the peak transmission on the aspect ratio (L_x/L_y) are observed. With increasing aspect ratio, the resonance wavelength of rectangular nanoholes red-shifts, the FWHM and the peak extinction increase. For a given dimension, the resonance wavelength has a slight blue-shift for nanoholes in the 350-nm thick film compared to in 300 nm thickness film, which is increasing with the aspect ratio of the nanohole. The dephasing time retrieved from the bandwidth varies between 4 and 6 fs, and has no systematic dependence on the aspect ratio. One can also observe that the transmission spectra of rectangle nanoholes 50×150 and 50×200 in air overlap with the spectral range of our in-focus excitation laser pulse (red curve), which indicates that these two rectangular nanoholes may show efficient resonance enhanced SHG.

The simulated transmission spectra of the nanohole 50×150 in two different surrounding immersion media oil and air are demonstrated in fig. 7.3 (b). One can observe that the transmission spectrum red-shifts in oil and the peak transmission is 130 times weaker compared to that in air. This rectangular nanohole exhibits almost the same FWHM of the transmission spectra and also almost the same dephasing time in oil and in air. For comparison, the transmission spectrum of the 350 nm thickness gold film in oil, which exhibits a characteristic peak around 493 nm and four orders of magnitude weaker transmission intensity compared to the rectangular nanohole 50×150 in air is shown in fig. 7.3 (b). The peak position of the transmission spectrum of the film is far away from that of nanoholes. There is no spectral overlap between those two spectra. The transmission spectrum of the film is not within the wavelength range of our excitation laser pulses, which indicates SHG would be very weak. From above observations, three conclusions can be drawn:

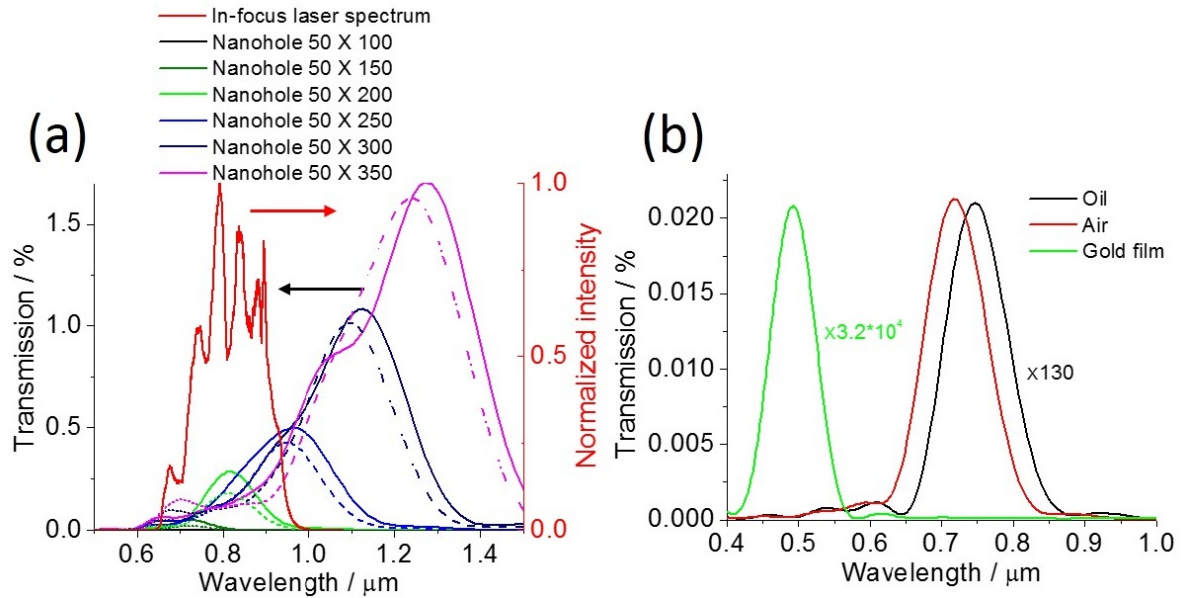


Figure 7.3: (a) Simulated transmission spectra of single rectangular nanoholes in air with $L_y \times L_x$ dimensions of 50×100 , 50×150 , 50×200 , 50×250 , and $50 \times 300 \text{ nm}^2$ in the 300-nm (solid curves) and 350-nm (dashed curves) thick gold films. The in-focus laser spectrum (red curve) is also shown for reference. (b) The simulated transmission spectra of nanohole 50×150 in oil (black curve), air (red curve), and of a bare gold film with a thickness of 350 nm (green curve) in oil are shown. The linear excitation polarization of the excitation field in all simulated spectra is along the short-axis of the rectangular nanohole.

First, the suitable candidates for further SHG experiments are nanohole 50×150 and nanohole 50×200 , which exhibit a plasmon resonance wavelength within the spectral range of our excitation laser pulses.

Second, the linear transmission intensity of nanorectangle holes in air is much stronger than

Table 7.2: The plasmon resonance parameters extracted from simulated transmission spectra of individual rectangular nanoholes ($L_y = 50$ nm, $L_x = 100\text{--}350$ nm) in the gold film with thicknesses of 300 nm and 350 nm in air, respectively.

Name	Dimension	Thickness 300 nm			Thickness 350 nm			
		$L_y \times L_x / \text{nm}^2$	$\lambda_{\text{res}} / \text{nm}$	FWHM / nm	T_2 / fs	$\lambda_{\text{res}} / \text{nm}$	FWHM / nm	T_2 / fs
Nanohole 50 X 100	50 X 100		641 ± 2	75 ± 5	5.8 ± 0.2	640 ± 2	74 ± 5	5.8 ± 0.2
Nanohole 50 X 150	50 X 150		725 ± 2	98 ± 5	5.6 ± 0.2	717 ± 2	100 ± 5	5.4 ± 0.2
Nanohole 50 X 200	50 X 200		817 ± 2	139 ± 5	5.1 ± 0.2	808 ± 2	135 ± 5	5.1 ± 0.2
Nanohole 50 X 250	50 X 250		970 ± 2	245 ± 5	4.0 ± 0.2	950 ± 2	195 ± 5	4.9 ± 0.2
Nanohole 50 X 300	50 X 300		1126 ± 2	270 ± 5	5.2 ± 0.2	1092 ± 2	237 ± 5	5.3 ± 0.2
Nanohole 50 X 350	50 X 350		1270 ± 2	340 ± 5	5.0 ± 0.2	1242 ± 2	327 ± 5	5.0 ± 0.2

in oil, which also suggests that the SHG intensity will be weaker in oil.

Third, from the previous experience of nanoparticle experiments, one can expect that our system is able to temporally resolve plasmon resonance dephasing of nanohole 50×150 and nanohole 50×200 .

7.4 Single rectangular nanohole characterization by SHG experiments

In this section, the size effect in the SHG response of individual rectangular nanohole in gold films with thicknesses of 300 nm and 350 nm are investigated. The SHG efficiency as a function of the average excitation laser power and of the linearly polarized excitation field dependence are also studied for both forward- and epi-detection geometries. By employing SHG IAC trace measurements with sub 8-fs laser pulses, ultrafast plasmon resonance enhanced SHG properties of the single rectangular nanoholes will be studied.

7.4.1 Epi-detected SHG

Single rectangular nanoholes with different dimensions were investigated by SHG imaging and spectroscopy. The SHG image of the rectangular nanohole array is shown in fig. 7.4 (a). The linear polarization of the excitation laser field is parallel to the long-axis of the rectangular nanohole. One can observe that the SHG intensities of individual rectangular nanoholes along

each column exhibit nearly the same brightness, which indicates that the reproducibility of the nanoholes dimensions is good. To quantitatively analyze the SHG intensity on the rectangular nanohole dimensions, a lateral SHG intensity profile for one row of nanoholes with different dimensions along the blue arrows shown in fig. 7.4 (a) is shown in fig. 7.4 (b). One can observe that the single nanohole exhibits an SHG intensity enhancement when compared to a constant background SHG signal from the gold film between rectangular nanoholes. The ratio between these two SHG intensities ranges from 4 to 8. The SHG peak observed when focused on the single nanoholes shows no clear dependence on the L_x dimensions of rectangular nanoholes. Its width corresponds to the diffraction-limited focus dimensions of (320 ± 10) nm, which is close to the result shown in section 6.6.2. The SHG signal on the film marked by (*) is assigned to surface imperfections, such as fine structural corrugations and roughness on the film, which are SHG-active.

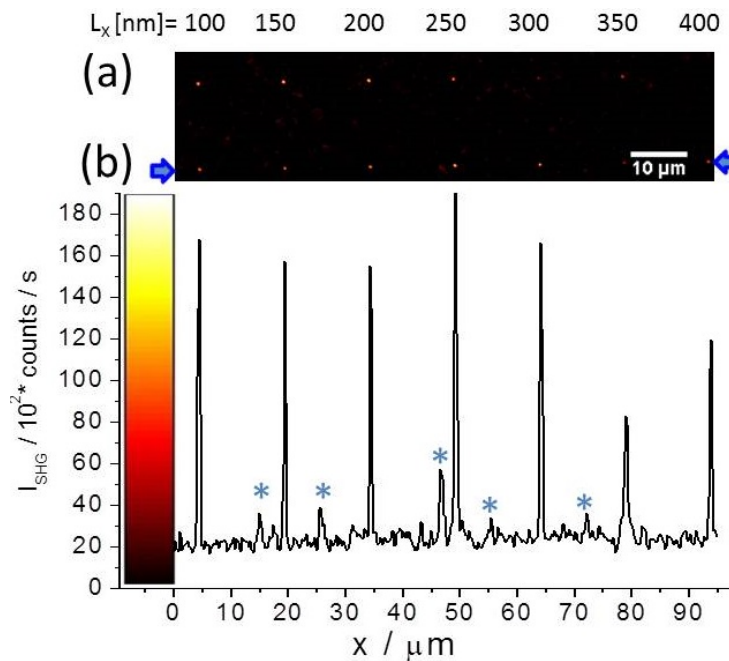


Figure 7.4: (a) Epi-detected SHG image of an array consisting of single rectangular nanoholes in rows of varying L_x from 100 to 400 nm and constant width of $L_y = 50$ nm in air. The gold film thickness is 300 nm. (b) The SHG intensity profile along the blue arrows shown in (a). SHG features marked by the blue star (*) account for SHG-activated imperfection of the film. The linearly polarized excitation field is parallel to the long-axis of the rectangular nanohole. The average excitation laser power used here is $750 \mu\text{W}$.

In order to systematically study the dependence of the SHG intensity on the size of single rectangular nanoholes, the SHG intensity time traces for different rectangular nanoholes were measured. The relatively low average excitation laser power of $260 \mu\text{W}$ was used in order to avoid possible sample damage. Fig. 7.5 (a) shows the absolute SHG intensity of the film (red

squares), which is measured on a position far away from the nanoholes. The SHG intensity on the film is (265 ± 50) counts/s. The error is derived from the standard deviation of fluctuation in the SHG intensity time trace. The absolute SHG intensities of the nanoholes (black squares) obtained by averaging SHG intensity time traces as a function of the nanohole dimension is also shown in fig. 7.5 (a). One can observe that the SHG intensity for the rectangular nanoholes varies from 800 to 1000 counts/s, and the relative errors of $\leq 55\%$ derived from standard deviations of averaging SHG intensities of two individual nanoholes are obtained. The ratio between SHG intensity on the nanoholes and film is around 6, which indicates that there is an SHG enhancement when the excitation laser is focused on the nanoholes. From the comparison among these rectangular nanoholes, no significant enhancement of the SHG response is observed even when the excitation laser wavelength matches the plasmon resonance band. As for the lateral SHG intensity profile shown in fig. 7.4 (b), again, no obvious dependence of the SHG intensity on the size of the rectangular nanohole is observed within the error introduced by the reproducibility of the rectangular nanohole dimensions [10]. The strong SHG intensity for nanohole 50×300 marked by *, which is 3 to 4 times stronger than that for the other nanoholes is attributed to a SHG-active 'hot spot' as observed in reference [10] for similar nanohole arrays.

The dependence of the SHG intensity recorded when focused on the nanohole 50×200 (blue squares) and 300-nm thick film (black squares) on the average excitation laser power is shown in the log-log plot in the fig. 7.5 (b). The errors were derived from the standard deviations of SHG intensity fluctuations, which are larger than the shot noise limit. Both experimental curves are well described by a quadratic power dependence with a slope of two (solid lines) in accordance with eq. 3.26, which indicates that additional third-order and high-order nonlinear processes do not contribute to the measured SHG signal for both the nanohole and the film within the experimental error. The ratio between SHG intensities of the nanohole and of the film ranges from 5 to 6, which agrees well with the ratios extracted from the SHG intensity profile shown in fig. 7.4 (b) and extracted from the SHG intensity time trace measurements shown in fig. 7.5 (a).

The epi-detected SHG polarization properties for both the single rectangular nanohole and the 300-nm thick gold film were also studied. The orientation of the rectangular nanohole in the x-y sample plane and the angle α between the linearly polarized excitation field and the x-axis were defined in fig. 7.6 (a). Fig. 7.6 (b) shows the polarization-resolved SHG intensity recorded when focused on the film. The SHG polar plot was normalized to that observed for a single nanohole shown in fig. 7.6 (c). One would expect that the polar plot on the film is isotropic. However, the SHG polar plot shown here has a strong polarization dependence, which might be introduced by the film's imperfections. The shown relative errors for both cases were derived from the standard deviations of fluctuations in SHG intensity time traces. The experimental polarization-resolved SHG intensity for the single rectangular nanohole is

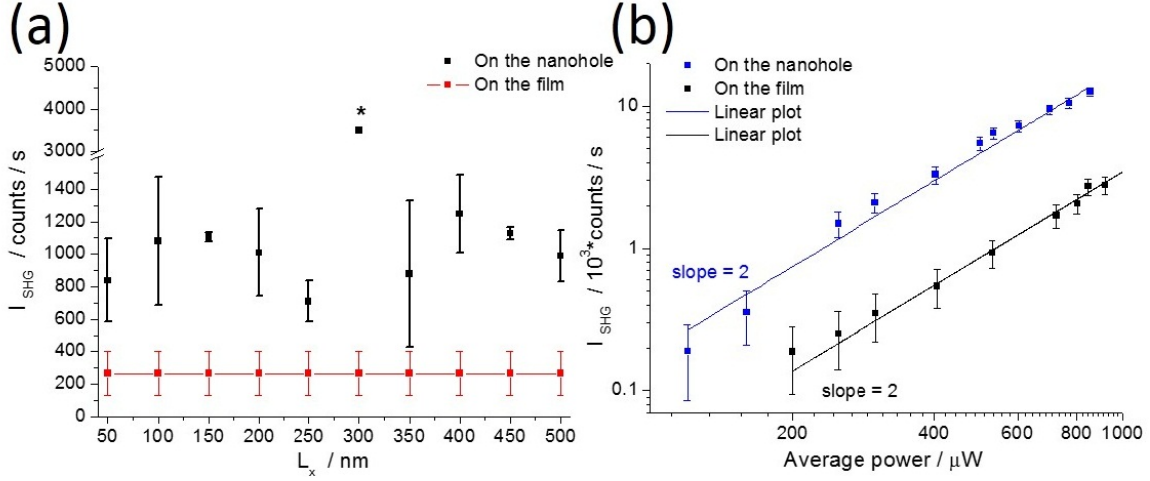


Figure 7.5: (a) SHG intensities retrieved from measured SHG intensity time traces when focused on 300-nm thick film (red squares) and on the single rectangular nanoholes (black squares) with $L_y \times L_x$ dimensions of 50×50 , 50×100 , 50×150 , 50×200 , 50×250 , 50×300 , 50×350 , 50×400 , 50×450 , and $50 \times 500 \text{ nm}^2$. The error bars for the film and nanohole measurements represent standard deviations of fluctuations of SHG intensity time traces and average SHG intensities of two different individual nanoholes, respectively. The average powers used here are $260 \mu\text{W}$. (b) The log-log plot of SHG intensity of the single nanohole 50×200 (blue squares) and of the film (black squares) as a function of the average excitation laser power. The theoretical curves with a slope of two (solid curves) are shown for references.

well described by the $\cos^4(\alpha - \alpha_0)$ function (red curves) (see eq. 3.43), which indicates that the epi-detected SHG response from the rectangular nanohole exhibits a well-defined dipole pattern with $\alpha_0 = (9 \pm 2)^\circ$. This result confirms that the enhancement of the SHG intensity is maximized when the excitation field is polarized parallel to the long-axis of the rectangular nanohole [10]. The ratio between the SHG intensities of the hole and the film at $\alpha_0 = 9^\circ$ amounts to about 5.5, which again agrees with the signal-to-background ratios observed in figs. 7.4 and 7.5.

The SHG spectra measured for a single rectangular nanohole 50×250 (black curve) and for the film (blue curve) in the epi-detection geometry are shown in fig. 7.7(a). The SHG spectra demonstrate that no observed luminescence or other multi-photon process was excited. The ratio of the peak SHG intensities at 410 nm between the rectangular nanohole and the film is around 4, which is also close to the values determined by SHG imaging and SHG intensity time trace measurements. Fig. 7.7 (b) shows the normalized SHG spectra of the film and the rectangular nanoholes with $L_y \times L_x$ dimensions of 50×100 , 50×150 , 50×200 , 50×250 , 50×300 , 50×350 , 50×400 , 50×450 , and $50 \times 500 \text{ nm}^2$. No obvious differences between the individual normalized SHG spectra of the rectangular nanoholes and between those of the nanoholes and of the film were observed. From the simulated linear transmission spectra in fig. 7.3, we expected some affect on the SHG spectra introduced by plasmon resonance. However,

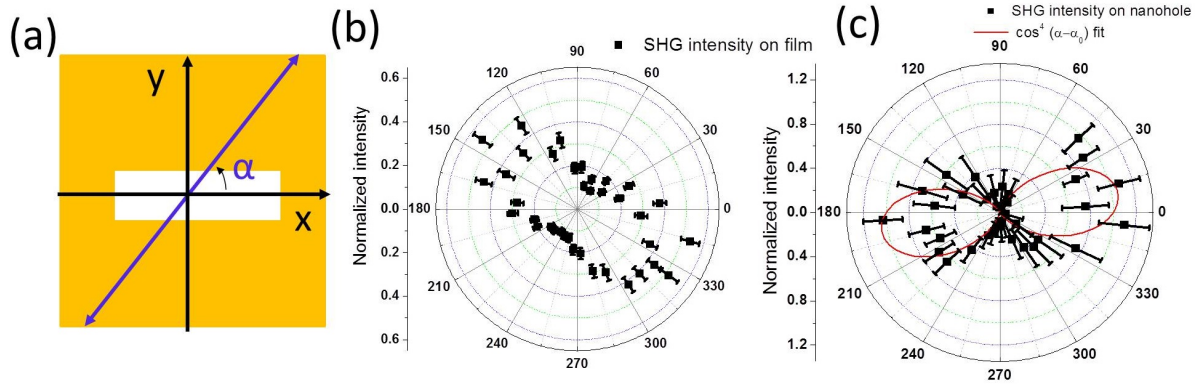


Figure 7.6: (a) Schematic layout showing the arrangement of a single rectangular nanohole in the x-y sample plane and defining the angle α between the linearly polarized excitation field (double arrow) and the x-axis. (b) Experimental SHG intensity polar plot (black squares) recorded on the bare film. (c) Difference SHG intensity polar plot (black squares) together with a fit to eq. 3.43 (red line), obtained by subtracting the SHG intensity recorded on the individual rectangular nanohole 50×200 with the SHG background of the film shown in (b). The average excitation laser power in these SHG experiments is $750 \mu\text{W}$.

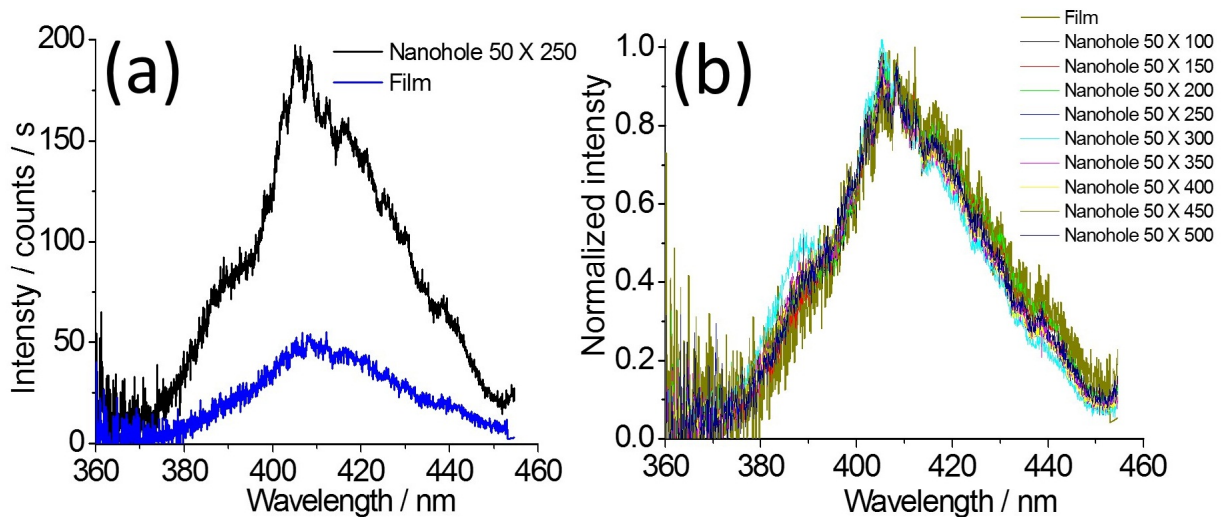


Figure 7.7: (a) The epi-detected SHG spectra measured for a single rectangular nanohole 50×250 (black curve) and for the 300-nm thick gold film (blue curve). (b) Normalized SHG spectra of single rectangular nanoholes with different dimensions and of the film. The linear polarization of the excitation field is parallel to the long-axis of the rectangular nanohole. The average excitation laser power is $520 \mu\text{W}$.

no dependence of the measured SHG spectrum on the linear transmission resonance properties was found.

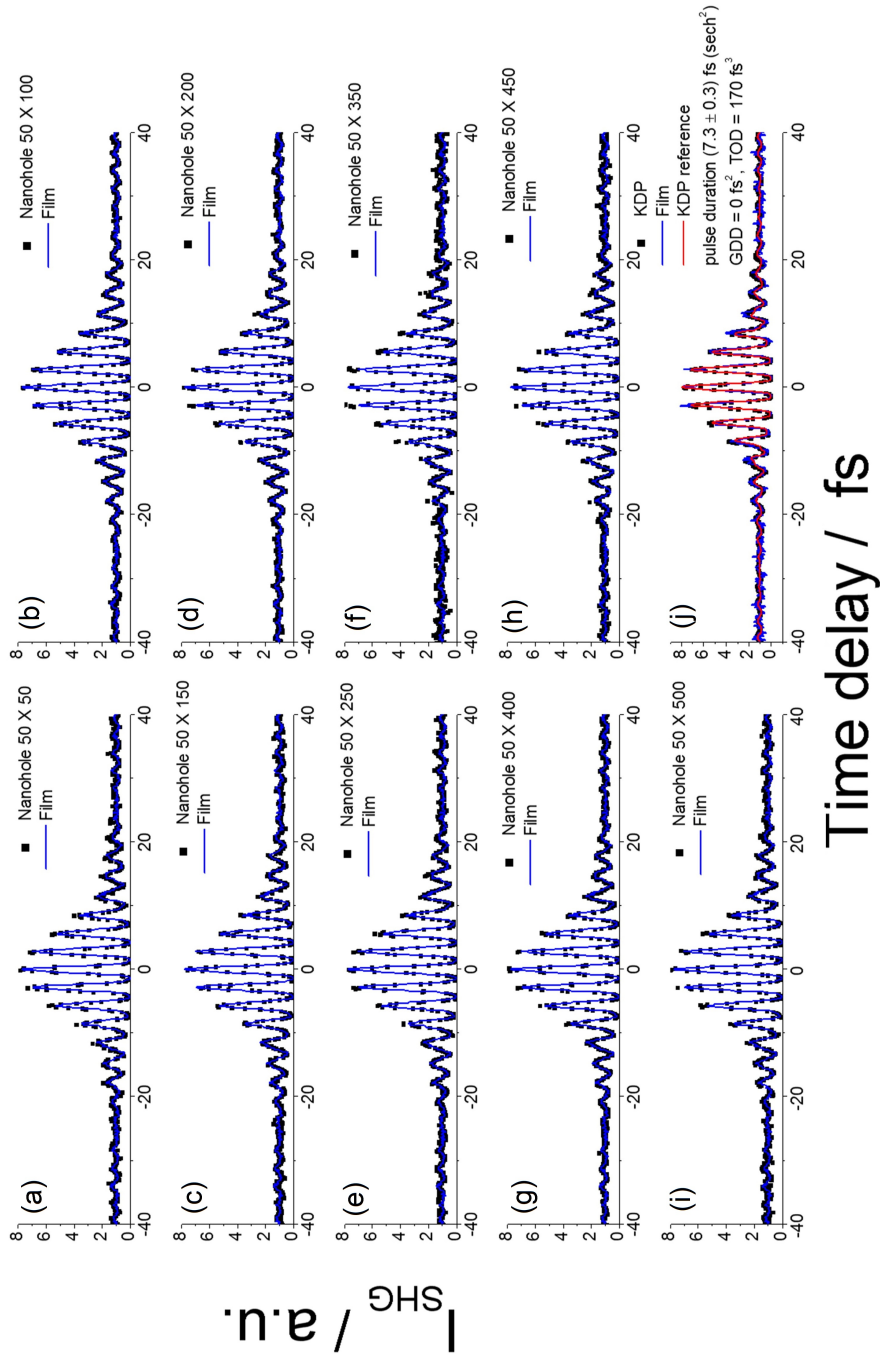


Figure 7.8: Measured SHG IAC traces (a), (b), (c), (d), (e), (f), (g), (h), and (i) of single rectangular nanoholes (black squares) with $L_y \times L_x$ dimensions of 50×50 , 50×100 , 50×150 , 50×200 , 50×250 , 50×350 , 50×400 , 50×450 , and $50 \times 500 \text{ nm}^2$, respectively, together with the measured SHG IAC trace of 300-nm thick gold film (blue curves). The experimental SHG IAC trace of the KDP crystal (black squares) measured under the identical experimental conditions and of the simulated SHG IAC trace (red curve) with shortest in-focus excitation laser pulses of $(7.3 \pm 0.3) \text{ fs}$ (sech^2) and residual dispersion values of $\text{GDD} = 0 \text{ fs}^2$ and $\text{TOD} = 170 \text{ fs}^3$ are also shown in (j). The average excitation laser power in all experiments is $260 \mu\text{W}$, and the excitation polarization field is linearly polarized parallel to the long-axis of the rectangular nanoholes.

Figs. 7.8 (a), (b), (c), (d), (e), (f), (g), (h), and (i) show the measured SHG IAC traces (black squares) of the single rectangular nanoholes with $L_y \times L_x$ dimensions of 50×50 , 50×100 , 50×150 , 50×200 , 50×250 , 50×350 , 50×400 , 50×450 , and $50 \times 500 \text{ nm}^2$, respectively. For reference, the measured SHG IAC traces of 300-nm thick gold film (blue curves) are also shown. The SHG IAC traces are obtained by averaging 10 to 20 individual SHG IAC traces to increase the single-to-noise ratio. The ratio of 8:1 between SHG intensities measured at time delay 0 and time delay $\pm 40 \text{ fs}$ also confirms that pure SHG signals without any THG and three-photon induced luminescence being present. The fringe spacing in the SHG IAC traces of the different rectangular nanoholes and of the gold bare film are identical. Also the SHG IAC intensity envelope profiles (not shown) of the different nanoholes and of the film are identical within the experimental error. Hence, for all the measured nanoholes, there is no evidence for a dependence of the SHG IAC response on the linear plasmon resonance properties. In the fig. 7.8 (j), the experimental SHG IAC trace of the film (blue curve) and that of the KDP (black squares) measured under identical experimental conditions are shown and observed to be identical. It is worthy noting that there is an obvious broadening for the experimental SHG IAC trace of KDP compared to the SHG IAC trace (red curve) simulated according to eqs. 3.36 and 3.37, where our in-focus excitation laser pulses of $(7.3 \pm 0.3) \text{ fs}$ (sech^2) with residual dispersion values of $\text{GDD} = 0 \text{ fs}^2$ and $\text{TOD} = 170 \text{ fs}^3$ are assumed. The observation indicates that the temporal resolution in these epi-detected SHG experiments is degraded when compared to the shortest in-focus pulses presented in chapters 5 and 6. We cannot explain the observed broadening of the SHG IAC envelope when the APD detector is used in these experiments. The alternative use of the PMT detector is not a good option, because it is not sensitive enough to detect the weak SHG signal of the single nanohole.

The consequences of the degraded temporal resolution in the epi-detected SHG IAC trace measurements are discussed in fig. 7.9, which shows the simulated SHG IAC traces according to eqs. 3.36 and 3.37 for the single rectangular nanohole 50×100 , 50×150 , 50×200 , 50×250 , and 50×350 based on the plasmon resonance parameters retrieved from the simulated linear transmission spectra listed in table 7.2 and assuming our shortest in-focus excitation laser pulses of $(7.3 \pm 0.3) \text{ fs}$ (sech^2) with residual dispersion values of $\text{GDD} = 0 \text{ fs}^2$ and $\text{TOD} = 170 \text{ fs}^3$ using eqs. 3.69 to 3.72. From the comparison between these simulated SHG IAC traces with the experimental time-resolving capability demonstrated by SHG IAC trace of the film (black curve), it is obvious that intensity envelope profiles for the simulated SHG IAC traces of the nanoholes will not be broader than that of the experimental SHG IAC traces of the film. For the fringe spacings, one would expect to observe differences at a time delay of around 10 fs between these SHG IAC traces. Since these differences were not observed in our experiments, we are not able to retrieve the plasmon resonance information for these individual rectangular nanoholes by using epi-detected SHG IAC experiments.

Summarizing all SHG measurements in the epi-detection geometry, the following conclusions can be drawn: First, there is an SHG intensity enhancement when focused on the single rectangular nanohole compared to the SHG intensity of the bare gold film. While in both cases, the dominant SHG contributions originate from the component of the second-order susceptibility with all diagonal coefficients perpendicular to the metal film surface [87] [88] [89], the induced SHG dipoles are of different origins for the two regions [9]: The dominant SHG contribution when focused on the single nanohole is attributed to the induced nonlinear dipole at the aperture surface parallel to the film. In contrast, the origin of the smaller SHG signal from the bare gold film is attributed to the nonlinear dipole contribution induced by the weaker field components in the tightly focused excitation beam that are normal to the film surface [25]. Second, the polarization-resolved SHG intensity of the single rectangular nanohole has $\cos^4(\alpha - \alpha_0)$ dipole dependence according to eq. 3.43. The orientation of the aperture edge induced dipole is parallel to the long axis of the rectangular nanohole. Third, no size dependence of neither SHG intensity, SHG spectrum, or SHG IAC traces for different rectangular nanoholes was resolved, which suggests that the contribution due to the field enhancement at aperture edges perpendicular to the incident electric field [11] rather than the LSPR contribution dominates the epi-detected SHG signal from individual gold nanoholes.

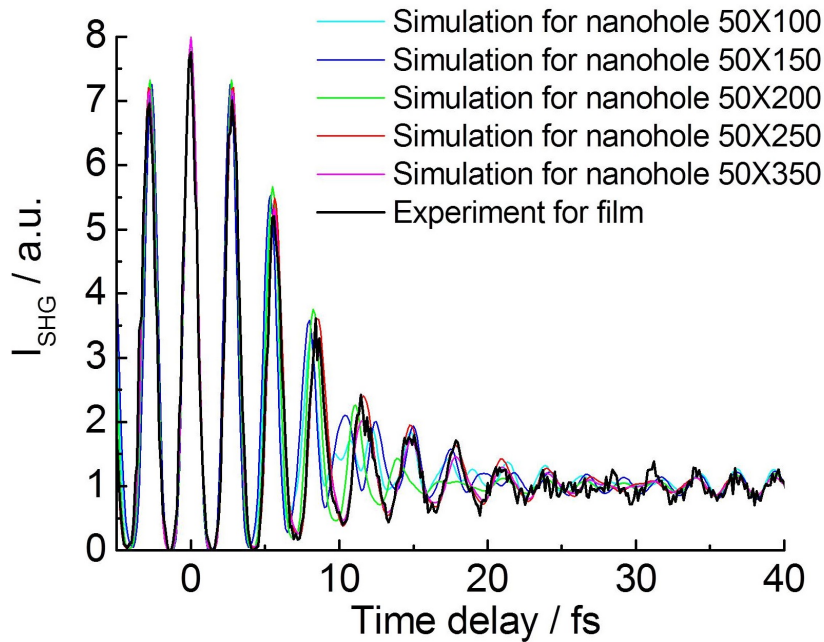


Figure 7.9: Comparison between the experimental SHG IAC trace recorded on the bare 300-nm thick gold film (black curve) and the simulated SHG IAC traces of single rectangular nanoholes with dimensions 50×100 , 50×150 , 50×200 , 50×250 , and $50 \times 300 \text{ nm}^2$ when assuming the plasmon resonance parameters as listed in table 7.2 and our shortest in-focus excitation laser pulses of $(7.3 \pm 0.3) \text{ fs}$ (sech^2) with residual dispersion values of $\text{GDD} = 0 \text{ fs}^2$ and $\text{TOD} = 170 \text{ fs}^3$.

In summary, the temporal resolution is degraded beyond the expected dephasing time of about 5.8 fs in the epi-detection geometry. There is always a nonresonant contribution to the SHG signal from the bare gold film, which is independent of the plasmon properties of the nanohole. In order to avoid these experimental limitations that are present in our epi-detected SHG measurements of these nanohole array samples, the SHG IAC trace of the individual rectangular nanoholes will be measured in the forward-detection geometry, as will be discussed in the following section.

7.4.2 Forward-detected SHG

Since the refractive index is mismatched, using air as immersion medium is not a good option to achieve high SHG collection efficiency in the forward detection. The use of water as immersion medium and a water-immersion objective (Olympus UPlanAPO 60× N.A. 1.2W IR) for the SHG experiment were tested, but the collected SHG intensity is very weak. The ratio of the SHG signal-to-noise is around 1.4. Then immersion oil (Olympus, Type-F, $n = 1.518$) and an Olympus oil immersion objective (PlanApo 60× N.A., 1.4) were used to collect the SHG signal, which resulted in best SHG signal-to-noise ratio. With the same excitation power, the SHG signal in forward-detection geometry is about one order of magnitude lower than that recorded in epi-detection geometry.

Figs. 7.10 (a) and (b) show the polarization-resolved SHG images recorded for one and the same single rectangular nanohole 50×300 in 350-nm thick gold film with linearly polarized excitation perpendicular and parallel to the x-axis, respectively. The orientation of the rectangular nanohole in the x-y sample plane is defined in fig. 7.11 (c). Since the SHG intensity detected in forward-detection geometry is one order of magnitude weaker than that detected in epi-detection geometry, the average excitation laser power of 1500 μW was chosen here in order to obtain a SHG signal with a similar signal-to-noise ratio. No SHG was observed when the linear polarization of the excitation field is parallel to the long-axis of the rectangular nanohole (see fig. 7.10 (b)). When the polarization of the excitation field is perpendicular to the long-axis of the rectangular nanohole (see fig. 7.10 (a)), the SHG intensity is enhanced when focused on the nanohole, and no SHG was observed when focused on the bare gold film. Two SHG intensity profiles along the white lines shown in fig. 7.10 (a) and (b) are shown in (c) and (d), respectively. Comparing the SHG intensity profiles, the SHG background signals from the film are near to the dark-counts level in the forward-detection geometry. This observation indicates that background SHG signal contributions from the gold film are negligible. The FWHM of the SHG intensity profile shown in fig. 7.10 (c) has a value of (410 ± 10) nm, which exceeds the diffraction-limited focus spot dimension (see fig. 5.1). The convolution of the focus spot size with a L_x dimension of the rectangular nanohole can explain the observed value.

Fig. 7.11 (a) shows the log-log plot of the SHG intensity as a function of average excita-

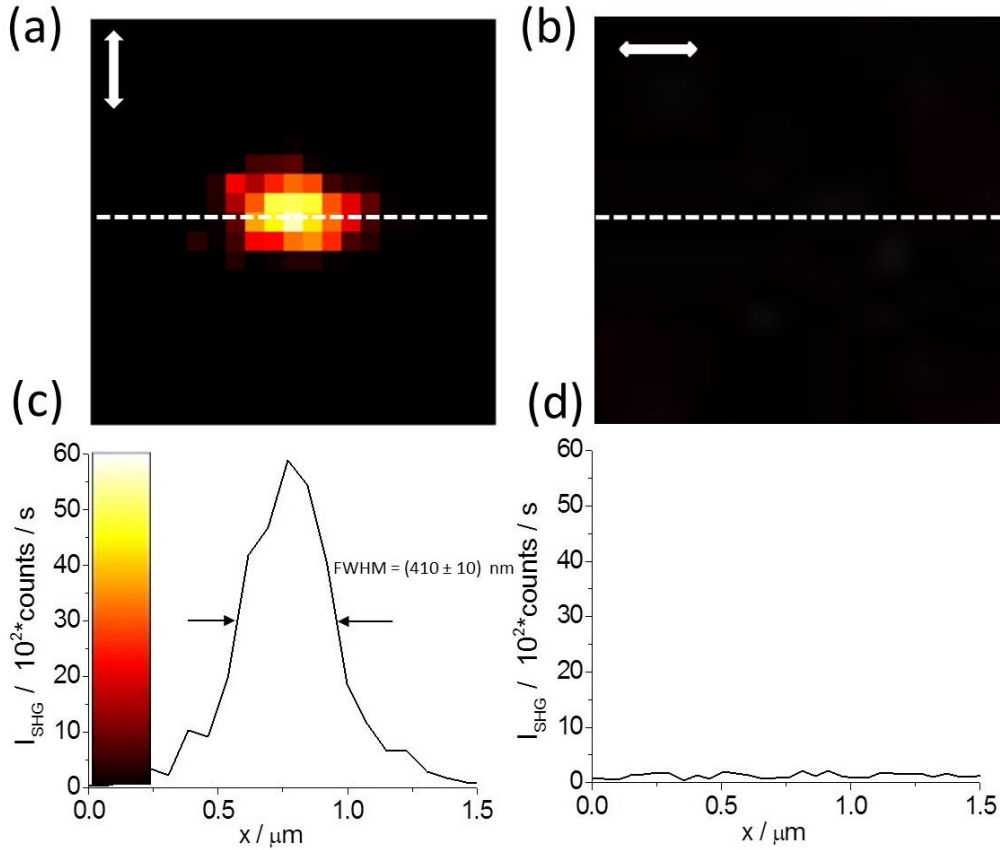


Figure 7.10: Forward-detected SHG images of an individual rectangular nanohole with $L_y \times L_x$ dimensions of $50 \times 300 \text{ nm}^2$ in a 350-nm thick gold film oriented in the x - y sample plane according to fig. 7.11 (c) and recorded with linearly polarized excitation perpendicular (a) and parallel (b) to the x -axis. (c), (d) SHG intensity profiles along the white dashed lines shown in the images (a) and (b), respectively. The average excitation laser power is $1500 \mu\text{W}$.

tion laser power at the nanohole 50×200 (black squares). The errors were derived from the standard deviation of the fluctuations in the SHG intensity time traces. The theoretical curve for a SHG with slope of two (red curve) is shown for reference. Within the experimental error, the measured signal follows the quadratic dependence on the in-focus average excitation power (see eq. 3.26), which indicates that additional third-order and high-order nonlinear processes do not contribute to the measured signal.

Fig. 7.11 (b) shows the normalized polarization-resolved SHG intensity recorded for a single rectangular nanohole 50×200 in a 350-nm gold film as a function of the angle α , as defined in fig. 7.11 (c). In order to avoid any sample damage in these measurements with relative long data acquisition time, the average excitation laser power was kept at $580 \mu\text{W}$. Contrary to the polarization-SHG intensity measured in the epi-detection geometry (see fig. 7.6), there is no SHG signal contribution from the film in the forward-detection geometry. The relative errors are derived from the standard deviation of fluctuations in the recorded SHG intensity time

traces. Because the SHG signals are weak, the big relative errors appear. This angle dependence of SHG intensities is well described by the $\cos^4(\alpha - \alpha_0)$ function (see eq. 3.43), which reflects the well-known dipole characteristics for a two-photon induced scattering process. For the measured SHG intensity, the orientation angle α_0 was determined to be $(98 \pm 6)^\circ$. This result confirms the fact that forward-detected SHG is maximized when the excitation field is polarized perpendicular to the long-axis of the rectangular nanohole. Compared to the polar plot of the epi-detected SHG intensity of its complementary structure, that is a single rectangular nanoparticle shown in fig. 6.18, the polarization-resolved SHG polar plot measured for the rectangular nanohole with the same orientation in the x-y sample plane exhibit an orthogonal rotation. This orthogonal polarization dependence of SHG signals is similar to that expected for the linear optical properties (see fig. 3.5), which are explained by Babinet's principle [12]. To our best knowledge, this is the first demonstration of the Babinet's principle in second-harmonic scattering at a single rectangular nanohole in a metal film.

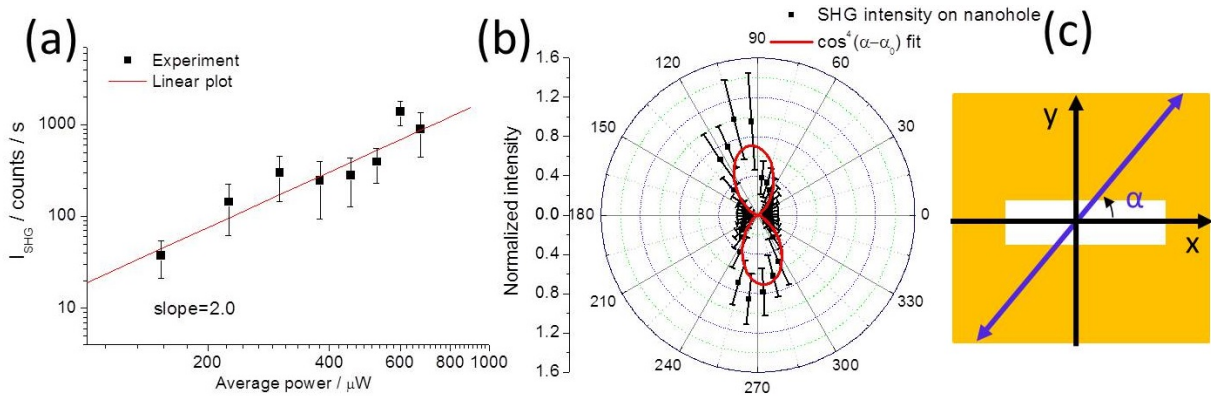


Figure 7.11: (a) The log-log plot of forward-detected SHG intensity of a single nanohole 50×200 in a 350-nm thick gold film as a function of average excitation powers (black squares). The theoretically expected quadratic power dependence with slope of two (red curve) is shown for reference. (b) SHG polar plot of the individual nanohole 50×200 detected in the forward direction together with a fit to eq. 3.43 (red curve). The average excitation laser power is $580 \mu\text{W}$. (c) Schematic layout showing the arrangement of a single rectangular nanohole in the x-y sample plane and defining the angle α between the linearly polarized excitation field (double arrow) and the x-axis.

According to the plasmon resonance information obtained from simulated linear transmission spectra listed in table 7.2, rectangular nanohole 50×200 and 50×350 were chosen for SHG IAC trace measurements shown in fig. 7.12 (a) and (b), respectively. The rectangular nanohole 50×200 was expected to exhibit resonance enhanced SHG because its linear resonance wavelength is within the spectral range of the excitation laser pulses. The rectangular nanohole 50×300 was chosen to represent the non-resonant control experiment, since its linear plasmon resonance wavelength is outside the spectral range of excitation laser pulses. In both

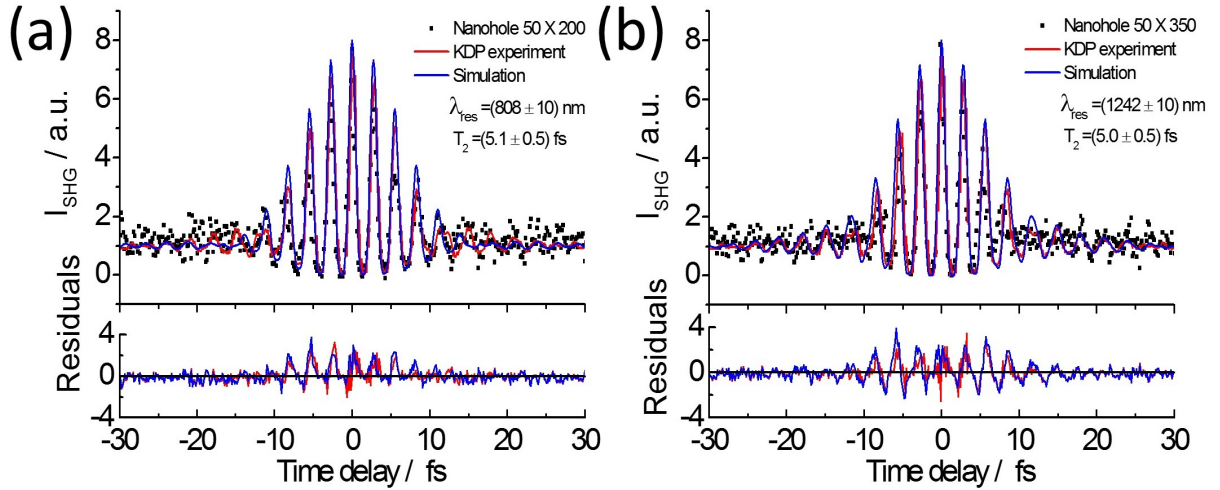


Figure 7.12: (a) The measured SHG IAC traces of the single rectangular nanohole 50×200 (black squares) in 350-nm thick gold film in oil and of the KDP reference (red curve) together with simulated SHG for a plasmon resonance enhanced SHG with parameters $T_2 = (5.1 \pm 0.5)$ fs and $\lambda_{res} = (808 \pm 10)$ nm using our in-focus laser pulses of 7.3 fs ($sech^2$) with residual dispersion $GDD = 0 \text{ fs}^2$ and $TOD = 170 \text{ fs}^3$ (blue curve). (b) The corresponding SHG IAC traces measured for a single nanohole 50×350 (black squares) and for the KDP reference (red curve) together with the corresponding SHG IAC simulation for plasmon resonance enhanced SHG with parameters $T_2 = (5.0 \pm 0.5)$ fs and $\lambda_{res} = (1242 \pm 10)$ nm (blue curve). The average excitation laser power in all experiments is $1200 \mu\text{W}$ and the excitation field is linearly polarized parallel to the short-axis of the rectangular nanohole.

SHG IAC traces, the ratio of SHG intensity at time delay zero to that at ± 40 fs is close to the theoretical value of 8, which indicates that additional third-order and high-order nonlinear processes do not contribute to the measured signal.

The comparison of the intensity envelopes, fringe spacings, and the residual (red curve) between the experimental SHG IAC trace measured for the rectangular nanohole 50×200 (black squares) with that measured for the KDP reference (red curve) illustrate that both traces are indistinguishable within the experimental errors. It is worthy noting that no degradation of the temporal resolution of the system was observed. No obvious effect of plasmon dephasing was observed for the nanohole 50×200 when compared to the KDP simulation (blue curve), which is considered to exhibit an instantaneous response (see eq. 3.33).

The simulated SHG IAC trace (blue curve) obtained by assuming the plasmon resonance parameters of $T_2 = 5.1$ fs and $\lambda_{res} = 808$ nm (see table 7.2) and eqs. 3.36, 3.37, 3.69 to 3.72 is also shown for comparison. Within the experimental error, there are no differences between the intensity envelope profiles, the fringe spacings, and the residuals (blue curve) in the simulated and experimental SHG IAC traces for the rectangular nanohole. At the delay time of 8.3 fs, the relative SHG peak intensity difference between the simulated and experimental KDP

SHG IAC traces is expected to be about 27%, whereas the relative error of the experimental peak SHG intensity is about 30%, which is derived from averaging the SHG peak intensities of 10 to 20 subsequent SHG IAC trace measurements of one and the same nanohole. We conclude that the signal-to-noise ratio in our SHG IAC experiments is too low in order to time-resolve the plasmon dephasing with T_2 of 5.1 fs in this single rectangular nanohole. Hence, we are not able to prove or disprove the hypothesis that plasmon resonance properties of single rectangular nanohole as obtained from linear transmission spectrum will also affect the ultrafast dephasing in SHG time-domain experiments. This experimental demonstration requires further enhancement of the detection sensitivity.

For the nonresonant case of rectangular nanohole 50×350 (see fig. 7.12 (b)), the corresponding comparison of the intensity envelopes, fringe spacings, and the residual (red curve) between the experimental SHG IAC traces recorded for the rectangular nanohole 50×350 (black squares) with that measured for the KDP reference (red curve) illustrate that both traces are indistinguishable within the experimental errors. From the comparison between simulated SHG IAC trace (blue curve) obtained by assuming plasmon resonance parameters of $T_2 = 5.0$ fs and $\lambda_{res} = 1242$ nm (see table 7.2) and eqs. 3.36, 3.37, 3.69 to 3.72, and experimental SHG IAC trace of the nanohole, there are no differences for the intensity envelope profiles, the fringe spacings, and the residuals (blue curves) observed within the experimental error. As discussed for the measurements of rectangular nanohole 50×200 , the same signal-to-noise limitation exists in our experiments. The intensity difference between the simulated and experimental KDP SHG IAC traces at delay time of 8.3 fs is around 26%, which is smaller than the experimental error around 30%. Also for the actual experiment, within our experimental error, we are not able to prove or disprove our hypothesis.

Summarizing all the SHG experiments of rectangular nanoholes recorded in the forward-detection geometry, the following conclusion can be drawn:

First, the forward-detected SHG signal only originates when focused on the single rectangular nanohole. The SHG intensity collected in the forward-detection geometry is around one order of magnitude weaker than that collected in the epi-detection geometry. No forward-detected SHG signal from the bare gold film was observed.

Second, the polarization-resolved SHG intensity of the single rectangular nanohole detected in the forward-detection geometry follows the characteristic $\cos^4(\alpha - \alpha_0)$ dependence of the second-order dipole. Its orientation is perpendicular to its complementary structure, which is orthogonal to the long axis of the rectangular nanohole.

Third, although forward-detected SHG signal from the single nanohole is background-free and no degradation of the temporal resolution is observed, the weak signal-to-noise ratio in these experiments prohibits the experimental demonstration of the effect of linear plasmon resonance properties on the corresponding SHG properties. Further experiments with improved SHG

detection sensitivity are needed.

7.5 Summary and Conclusions

In this chapter, we have investigated second-harmonic optical response of individual rectangular nanoholes with different dimensions in a gold film in both forward- and epi-detection geometries to the interaction with our tightly focused 7.3-fs excitation laser pulses. By comparison with simulated transmission spectra for these rectangular nanoholes, the following conclusions can be drawn:

Both the forward- and epi-detected SHG emissions from single rectangular nanoholes are observed, which for a given excitation power is one order of magnitude stronger when collected in the epi-direction. Because of the presence of non-resonance SHG background signal from the bare gold film, the dominant aperture edge induced contribution to SHG, and of the degraded temporal resolution in the epi-detection geometry, and because of a poor signal-to-noise ratio in the forward-detected SHG for a single nanohole, no ultrafast dephasing dynamic of LSPRs in rectangular nanoholes could be time-resolved. Also, the dependence of the rectangular nanohole plasmon resonance on the aspect ratio observed in the linear transmission spectra could not be reproduced in SHG intensities, which indicates that contributions from LSPRs enhanced SHG to the detected SHG signal are negligible. More work needs to be done in order to overcome the current experimental limitations. To give an example, by using custom-made band-pass filters with increased transmission at the SHG wavelengths, we expect an improvement of the forward-detected SHG detection sensitivity by about 60%.

In both forward- and epi-detection geometries, the dependence of the SHG intensity from the single rectangular nanohole on the angle between the incident linearly polarized excitation field and the long-axis of the rectangular nanohole follows that of a second-order dipole pattern. While the epi-detected SHG dipole pattern is oriented parallel to the long-axis of the rectangular nanohole, the forward-detected SHG dipole pattern is oriented perpendicular to the long-axis of the rectangular nanohole. To our best knowledge, the latter observation represents the first experimental demonstration of Babinet's principle in second-order nonlinear scattering of a single nanohole in a gold film, where the plasmon resonance enhanced SHG is expected to be rotated by 90° when compared to that of its complementary rectangular nanoparticle.

8 Acknowledgments

I am most grateful to my advisor, Dr. Andreas Volkmer, who conceived the idea of this project, for his critical discussion, for his guidance, and for his financial support throughout this project. His help during all the time in the experiment design, in conducting experiments, in physical model simulation, data analysis, and also in writing of this thesis have benefited me most. His tireless efforts in solving scientific problems and broadband analytical thinking have always inspired me.

I thank Prof. Dr. J. Wrachtrup for the possibility to do a PhD in his institute. Then I thank former group member Dr. Hilton Barbosa de Aguiar and Dr. Gabriel Tempea from Femtolasers Produktion GmbH for the help in dispersion management in the early part of this research project. I thank Johanna Konrad for her recipe for the preparation of collagen fibrils. I thank Dr. Rolf Reuter and Dr. Zappe Andrea for their help in the preparation of the nanoparticle suspension. I thank Stefan Gomes da Costa for his help in technical discussion during the experiments. I thank Dr. Gregor Hehl for his proof-reading of this thesis. I thank Paola Piredda and all group members for all the discussions, the nice atmosphere and the good collaboration.

I want to acknowledge our collaboration partners for their fruitful discussion and preparations of plasmonic nanoparticle and nanohole arrays: I thank Prof. Dr. Markus Lippitz from Universität Bayreuth and Prof. Dr. Klas Lindfors from Universität zu Köln for manufacturing the gold nanodisk and nanorectangle arrays at Max Planck Institut für Festkörperforschung. I thank Prof. Dr. Yehiam Prior and Yaara Bondy from Weizmann Institute of Science for manufacturing the nanohole array samples and for simulating their linear optical properties. The mechanical workshop of the University of Stuttgart I owe many custom made mechanics of all sizes and the glass workshop for cutting the glass filters.

Financial support from the German Federal Ministry of Education and Research (BMBF) of the projects MEDICARS (FKZ:13N10776) and QuantumCARS (FKZ:13GW0026) is gratefully acknowledged.

Finally, I would like to thank my family and all of my friends for their support since I went to study abroad. They have supported me in countless ways throughout the years including giving me the opportunity to finish the study. I cannot thank them enough.

9 Statement of Authorship

This Ph.D. thesis is the result of my own work. Published or unpublished work of others is credited to the author in the text. Except where references are made, the thesis contains no material published elsewhere or extracted in whole or in part from a thesis presented by me for another degree or diploma.

.....

.....

(Stuttgart, date)

(Signature, Hui Wan)

10 Bibliography

- [1] W. R. Zipfel, R. M. Williams, and W. W. Webb. Nonlinear magic: multiphoton microscopy in the biosciences. *Nature Biotechnology*, 21(11):1369–1377, 2003.
- [2] U. Keller. Ultrafast solid-state lasers. *Progress in Optics*, 46:1–115, 2004.
- [3] A. Chong, L. Wright, and F. Wise. Ultrafast fiber lasers based on self-similar pulse evolution: a review of current progress. *Reports on Progress in Physics*, 78(11):113901, 2015.
- [4] M. B. Raschke, S. Berweger, and J. M. Atkin. Chapter 7: Ultrafast and nonlinear plasmon dynamics. In *Plasmonics: Theory and Applications*. Eds. Shahbazyan, T. V. and Stockman, M. I., 3rd edition, Springer, Netherlands, 2013.
- [5] M. Pawłowska, S. Goetz, C. Dreher, M. Wurdack, E. Krauss, G. Razinskas, P. Geisler, B. Hecht, and T. Brixner. Shaping and spatiotemporal characterization of sub-10-fs pulses focused by a high- NA objective. *Optics Express*, 22(25):31496–31510, 2014.
- [6] M. I. Stockman. Chapter 1: Nanoplasmonics: From present into future. In *Plasmonics: Theory and Applications*. Eds. Shahbazyan, T. V. and Stockman, M. I., 3rd edition, Springer, Netherlands, 2013.
- [7] B. Lamprecht, A. Leitner, and F. R. Aussenegg. SHG studies of plasmon dephasing in nanoparticles. *Applied Physics B*, 68(3):419–423, 1999.
- [8] Y. H. Liao, A. N. Unterreiner, Q. Chang, and N. F. Scherer. Ultrafast dephasing of single nanoparticles studied by two-pulse second-order interferometry. *The Journal of Physical Chemistry B*, 105(11):2135–2142, 2001.
- [9] P. Schön, N. Bonod, E. Devaux, J. Wenger, H. Rigneault, T. W. Ebbesen, and S. Brasselet. Enhanced second-harmonic generation from individual metallic nanoapertures. *Optics Letters*, 35(23):4063–4065, 2010.

- [10] A. Salomon, M. Zielinski, R. Kolkowski, J. Zyss, and Y. Prior. Size and shape resonances in second harmonic generation from silver nanocavities. *The Journal of Physical Chemistry C*, 117(43):22377–22382, 2013.
- [11] T. A. Baker, A. Grubisic, and D. J. Nesbitt. Plasmon mediated multiphoton photoemission microscopy of au nanoholes and nanohole dimers. *The Journal of Physical Chemistry C*, 118(13):6959–6971, 2014.
- [12] J. D. Jackson. *Classical electrodynamics*. 3rd edition, John Wiley and Sons, New York, London, Sydney, 1999.
- [13] F. Falcone, T. Lopetegui, M. Laso, J. Baena, J. Bonache, M. Beruete, R. Marqués, F. Martin, and M. Sorolla. Babinet principle applied to the design of metasurfaces and metamaterials. *Physical Review Letters*, 93(19):197401, 2004.
- [14] T. Zentgraf, T. P. Meyrath, A. Seidel, S. Kaiser, H. Giessen, C. Rockstuhl, and F. Lederer. Babinet’s principle for optical frequency metamaterials and nanoantennas. *Physical Review B*, 76(3):033407, 2007.
- [15] M. Wollenhaupt, A. Assion, and T. Baumert. Chapter 12: Femtosecond laser pulses: Linear properties, manipulation, generation and measurement. In *Springer Handbook of Lasers and Optics*. Ed. Träger, F., Springer, New York, 2007.
- [16] J. M. Diels and W. Rudolph. *Ultrashort laser pulse phenomena*. 2nd edition, Academic Press, Oxford, 2006.
- [17] P. J. Wrzesinski, D. Pestov, V. V. Lozovoy, J. R. Gord, M. Dantus, and S. Roy. Group-velocity-dispersion measurements of atmospheric and combustion-related gases using an ultrabroadband-laser source. *Optics Express*, 19(6):5163–5170, 2011.
- [18] A. G. Van Engen, S. A. Diddams, and T. S. Clement. Dispersion measurements of water with white-light interferometry. *Applied Optics*, 37(24):5679–5686, 1998.
- [19] D. Strickland and G. Mourou. Compression of amplified chirped optical pulses. *Optics Communications*, 56(3):219–221, 1985.
- [20] R. L. Fork, O. E. Martinez, and J. P. Gordon. Negative dispersion using pairs of prisms. *Optics Letters*, 9(5):150–152, 1984.
- [21] A. Stingl, R. Szipöcs, C. Spielmann, and F. Krausz. Generation of 11-fs pulses from a Ti:sapphire laser without the use of prisms. *Optics Letters*, 19(3):204–206, 1994.
- [22] *FemtoOptics catalog*. Femtolasers Produktions GmbH, Vienna, 2015.

- [23] R. W. Boyd. *Nonlinear optics*. 3rd edition, Academic Press, Burlington, 2003.
- [24] C. Xu and W. W. Webb. Measurement of two-photon excitation cross sections of molecular fluorophores with data from 690 to 1050 nm. *Journal of the Optical Society of America B*, 13(3):481–491, 1996.
- [25] B. Richards and E. Wolf. Electromagnetic diffraction in optical systems. ii. structure of the image field in an aplanatic system. In *Proceedings of the Royal Society of London A: Mathematical, Physical and Engineering Sciences*. The Royal Society, 1959.
- [26] F. Helmchen and W. Denk. Deep tissue two-photon microscopy. *Nature Methods*, 2(12):932–940, 2005.
- [27] B. Broers, L. D. Noordam, and H. B. van Linden van den Heuvell. Diffraction and focusing of spectral energy in multiphoton processes. *Physical Review A*, 46(5):2749, 1992.
- [28] J. M. Diels, J. J. Fontaine, I. C. McMichael, and F. Simoni. Control and measurement of ultrashort pulse shapes (in amplitude and phase) with femtosecond accuracy. *Applied Optics*, 24(9):1270–1282, 1985.
- [29] C. Sönnichsen, T. Franzl, T. Wilk, Gero von Plessen, J. Feldmann, O. Wilson, and P. Mulvaney. Drastic reduction of plasmon damping in gold nanorods. *Physical Review Letters*, 88(7):077402–077402, 2002.
- [30] J. Duboisset, D. Aït-Belkacem, M. Roche, H. Rigneault, and S. Brasselet. Generic model of the molecular orientational distribution probed by polarization-resolved second-harmonic generation. *Physical Review A*, 85(4):043829, 2012.
- [31] M. Faraday. The Bakerian lecture: experimental relations of gold (and other metals) to light. *Philosophical Transactions of the Royal Society of London*, 147:145–181, 1857.
- [32] G. Mie. Beiträge zur Optik trüber Medien, speziell kolloidaler Metallösungen. *Annalen der Physik*, 330(3):377–445, 1908.
- [33] E. Hutter and J. H. Fendler. Exploitation of localized surface plasmon resonance. *Advanced Materials*, 16(19):1685–1706, 2004.
- [34] K. A. Willets and R. P. Van Duyne. Localized surface plasmon resonance spectroscopy and sensing. *Annual Review of Physical Chemistry*, 58:267–297, 2007.
- [35] P. Drude. Zur Elektronentheorie der Metalle. *Annalen der Physik*, 306(3):566–613, 1900.
- [36] M. Dressel and G. Grüner. *Electrodynamics of solids*. Cambridge University Press, New York, 2005.

- [37] C. Sönnichsen. *Plasmons in metal nanostructures*. PhD thesis, Ludwig-Maximilians-Universität München, 2001.
- [38] P. B. Johnson and R. W. Christy. Optical constants of the noble metals. *Physical Review B*, 6(12):4370, 1972.
- [39] U. Kreibig and M. Vollmer. *Optical properties of metal clusters*. Springer Berlin, 1995.
- [40] C. F. Bohren and D. R. Huffman. *Absorption and scattering of light by small particles*. John Wiley and Sons, New York, 2008.
- [41] B. T. Draine and P. J. Flatau. Discrete-dipole approximation for scattering calculations. *Journal of the Optical Society of America A*, 11(4):1491–1499, 1994.
- [42] V. Myroshnychenko, E. Carbó-Argibay, I. Pastoriza-Santos, J. Pérez-Juste, L. M. Liz-Marzán, and F. Javier García de Abajo. Modeling the optical response of highly faceted metal nanoparticles with a fully 3d boundary element method. *Advanced Materials*, 20(22):4288–4293, 2008.
- [43] U. Hohenester and A. Trügler. MNPBEM—A Matlab toolbox for the simulation of plasmonic nanoparticles. *Computer Physics Communications*, 183(2):370–381, 2012.
- [44] H. Volz. *Einführung in die theoretische Mechanik*. Akademische Verlagsgesellschaft, Frankfurt am Main, 1971.
- [45] A. Wokaun, J. P. Gordon, and P. F. Liao. Radiation damping in surface-enhanced Raman scattering. *Physical Review Letters*, 48(14):957, 1982.
- [46] B. Lamprecht, J. R. Krenn, A. Leitner, and F. R. Aussenegg. Resonant and off-resonant light-driven plasmons in metal nanoparticles studied by femtosecond-resolution third-harmonic generation. *Physical Review Letters*, 83(21):4421, 1999.
- [47] T. W. Ebbesen, H. J. Lezec, H. F. Ghaemi, T. Thio, and P. A. Wolff. Extraordinary optical transmission through sub-wavelength hole arrays. *Nature*, 391(6668):667–669, 1998.
- [48] A. Degiron, H. J. Lezec, N. Yamamoto, and T. W. Ebbesen. Optical transmission properties of a single subwavelength aperture in a real metal. *Optics Communications*, 239(1):61–66, 2004.
- [49] T. Rindzevicius, Y. Alaverdyan, B. Sepulveda, T. Pakizeh, M. Käll, R. Hillenbrand, J. Aizpurua, and F. J. García de Abajo. Nanohole plasmons in optically thin gold films. *The Journal of Physical Chemistry C*, 111(3):1207–1212, 2007.

- [50] B. Sepúlveda, Y. Alaverdyan, J. Alegret, M. Käll, and P. Johansson. Shape effects in the localized surface plasmon resonance of single nanoholes in thin metal films. *Optics Express*, 16(8):5609–5616, 2008.
- [51] M. Schwind, B. Kasemo, and I. Zoric. Localized and propagating plasmons in metal films with nanoholes. *Nano Letters*, 13(4):1743–1750, 2013.
- [52] A. Bitzer, A. Ortner, H. Merbold, T. Feurer, and M. Walther. Terahertz near-field microscopy of complementary planar metamaterials: Babinet’s principle. *Optics Express*, 19(3):2537–2545, 2011.
- [53] W. C. Chen, N. I. Landy, K. Kempa, and W. J. Padilla. A subwavelength extraordinary-optical-transmission channel in Babinet metamaterials. *Advanced Optical Materials*, 1(3):221–226, 2013.
- [54] C. Rockstuhl, T. S Zentgraf, T. P. Meyrath, H. Giessen, and F. Lederer. Resonances in complementary metamaterials and nanoapertures. *Optics Express*, 16(3):2080–2090, 2008.
- [55] H. U. Yang, R. L. Olmon, K. S. Deryckx, X. G. Xu, H. A. Bechtel, Y. Xu, B. A. Lail, and M. B. Raschke. Accessing the optical magnetic near-field through Babinet’s principle. *ACS Photonics*, 1(9):894–899, 2014.
- [56] Roper Scientific WinSpec/32 Version: 2.5.20.2, Copyright 1996-1999.
- [57] J. Jasapara and W. Rudolph. Characterization of sub-10-fs pulse focusing with high-numerical-aperture microscope objectives. *Optics Letters*, 24(11):777–779, 1999.
- [58] M. Kempe, U. Stamm, B. Wilhelmi, and W. Rudolph. Spatial and temporal transformation of femtosecond laser pulses by lenses and lens systems. *Journal of the Optical Society of America B*, 9(7):1158–1165, 1992.
- [59] M. Kempe and W. Rudolph. Femtosecond pulses in the focal region of lenses. *Physical Review A*, 48(6):4721, 1993.
- [60] Olympus. *UIS2 system*. Optical Co. Ltd. Tokyo Japan.
- [61] Z. Bor, Z. Gogolak, and G. Szabo. Femtosecond-resolution pulse-front distortion measurement by time-of-flight interferometry. *Optics Letters*, 14(16):862–864, 1989.
- [62] R. Netz, T. Feurer, R. Wolleschensky, and R. Sauerbrey. Measurement of the pulse-front distortion in high-numerical-aperture optics. *Applied Physics B*, 70(6):833–837, 2000.

- [63] W. Amir, T. A. Planchon, C. G. Durfee, J. A. Squier, P. Gabolde, R. Trebino, and M. Müller. Simultaneous visualization of spatial and chromatic aberrations by two-dimensional fourier transform spectral interferometry. *Optics Letters*, 31(19):2927–2929, 2006.
- [64] S. Tang, T. B. Krasieva, Z. P. Chen, G. Tempea, and B. J. Tromberg. Effect of pulse duration on two-photon excited fluorescence and second harmonic generation in nonlinear optical microscopy. *Journal of Biomedical Optics*, 11(2):020501–020501, 2006.
- [65] M. D. Shoulders and R. T. Raines. Collagen structure and stability. *Annual Review of Biochemistry*, 78:929–958, 2009.
- [66] D. J. Prockop and A. Fertala. The collagen fibril: the almost crystalline structure. *Journal of Structural Biology*, 122(1):111–118, 1998.
- [67] K. Beck and B. Brodsky. Supercoiled protein motifs: the collagen triple-helix and the α -helical coiled coil. *Journal of Structural Biology*, 122(1):17–29, 1998.
- [68] J. Konrad. Polarisations- und orts aufgelöste CARS-spektroskopie. *Diplomarbeit*, 3. Physikalischen Institut, Universität Stuttgart, 2012.
- [69] K. Kadler, D. Holmes, J. Trotter, and J. Chapman. Collagen fibril formation. *Biochemical Journal*, 316(1):1–11, 1996.
- [70] S. W. Chu, S. P. Tai, M. C. Chan, C. K. Sun, I. C. Hsiao, C. H. Lin, Y. C. Chen, and B. L. Lin. Thickness dependence of optical second harmonic generation in collagen fibrils. *Optics Express*, 15(19):12005–12010, 2007.
- [71] J. C. Bosbach, F. Stietz, T. Vartanyan, and F. Träger. Ultrafast dephasing of surface plasmon excitation in silver nanoparticles: influence of particle size, shape, and chemical surrounding. *Physical Review Letters*, 89(25):257404, 2002.
- [72] C. Sönnichsen, T. Franzl, T. Wilk, G. Von Plessen, and J. Feldmann. Plasmon resonances in large noble-metal clusters. *New Journal of Physics*, 4(1):93, 2002.
- [73] T. Zentgraf, A. Christ, J. Kuhl, and H. Giessen. Tailoring the ultrafast dephasing of quasi-particles in metallic photonic crystals. *Physical Review Letters*, 93(24):243901, 2004.
- [74] T. Ziegler, C. Hendrich, F. Hubenthal, T. Vartanyan, and F. Träger. Dephasing times of surface plasmon excitation in au nanoparticles determined by persistent spectral hole burning. *Chemical Physics Letters*, 386(4):319–324, 2004.

- [75] M.W. Klein, T. Tritschler, M. Wegener, and S. Linden. Lineshape of harmonic generation by metallic nanoparticles and metallic photonic crystal slabs. *Physical Review B*, 72(11):115113, 2005.
- [76] M. Hu, C. Novo, A. Funston, H. Wang, H. Staleva, S. Zou, P. Mulvaney, Y. Xia, and G. V. Hartland. Dark-field microscopy studies of single metal nanoparticles: understanding the factors that influence the linewidth of the localized surface plasmon resonance. *Journal of Materials Chemistry*, 18(17):1949–1960, 2008.
- [77] O. Muskens, G. Bachelier, N. D. Fatti, F. Vallee, A. Brioude, X. Jiang, and M. Pileni. Quantitative absorption spectroscopy of a single gold nanorod. *The Journal of Physical Chemistry C*, 112(24):8917–8921, 2008.
- [78] B. Metzger, T. Schumacher, M. Hentschel, M. Lippitz, and H. Giessen. Third harmonic mechanism in complex plasmonic fano structures. *ACS Photonics*, 1(6):471–476, 2014.
- [79] B. Metzger, L. Gui, J. Fuchs, D. Floess, M. Hentschel, and H. Giessen. Strong enhancement of second harmonic emission by plasmonic resonances at the second harmonic wavelength. *Nano Letters*, 15(6):3917–3922, 2015.
- [80] T. Zhao, J. W. Jarrett, J. S. Johnson, K. Park, R. A. Vaia, and Kenneth L. Knappenberger J. Plasmon dephasing in gold nanorods studied using single-nanoparticle interferometric nonlinear optical microscopy. *The Journal of Physical Chemistry C*, 120(7):4071–4079, 2016.
- [81] H. J. Lezec, A. Degiron, E. Devaux, R. A. Linke, L. Martin-Moreno, F. J. Garcia-Vidal, and T. W. Ebbesen. Beaming light from a subwavelength aperture. *Science*, 297(5582):820–822, 2002.
- [82] J. Prikulis, P. Hanarp, L. Olofsson, D. Sutherland, and M. Käll. Optical spectroscopy of nanometric holes in thin gold films. *Nano Letters*, 4(6):1003–1007, 2004.
- [83] L. Yin, V. K. Vlasko-Vlasov, A. Rydh, J. Pearson, U. Welp, S. H. Chang, S. K. Gray, G. C. Schatz, D. B. Brown, and C. W. Kimball. Surface plasmons at single nanoholes in Au films. *Applied Physics Letters*, 85(3):467–469, 2004.
- [84] C. Genet and T.W. Ebbesen. Light in tiny holes. *Nature*, 445(7123):39–46, 2007.
- [85] P. N. Melentiev, A. E. Afanasiev, A. A. Kuzin, A. V. Zablotskiy, A. S. Baturin, and V. I. Balykin. Single nanohole and photonic crystal: wavelength selective enhanced transmission of light. *Optics Express*, 19(23):22743–22754, 2011.

- [86] E. D. Palik. *Handbook of optical constants of solids*, volume 3. Academic Press, San Diego, 1998.
- [87] D. Krause, C. W. Teplin, and C. T. Rogers. Optical surface second harmonic measurements of isotropic thin-film metals: Gold, silver, copper, aluminum, and tantalum. *Journal of Applied Physics*, 96(7):3626–3634, 2004.
- [88] F. X. Wang, F. J. Rodríguez, W. M. Albers, R. Ahorinta, J. E. Sipe, and M. Kauranen. Surface and bulk contributions to the second-order nonlinear optical response of a gold film. *Physical Review B*, 80(23):233402, 2009.
- [89] G. Bachelier, J. Butet, I. Russier-Antoine, C. Jonin, E. Benichou, and P. F. Brevet. Origin of optical second-harmonic generation in spherical gold nanoparticles: Local surface and nonlocal bulk contributions. *Physical Review B*, 82(23):235403, 2010.

11 List of figures

3.1	Schematic illustration of a single dispersive mirror, where negative GDD and TOD are introduced by interferences at multilayer-coatings resulting in wavelength-dependent penetration depth. The figure is taken from reference [22].	13
3.2	Energy diagram describing the quantum mechanic process of second-harmonic generation (SHG). See the text for details.	14
3.3	The real part (a) and imaginary part (b) of the dielectric function of bulk gold plotted as function of photon energy. The black dots and blue curves represent the experimental data reported by Johnson and Christy [38] and their best fit to eq. 3.44 within the interval [1.4, 1.75] eV [37], respectively.	20
3.4	(a) A Lorentzian line shape describing LSPR plasmon electric field with $\hbar\omega_{res}=1550$ meV and $T_2=10$ fs in the frequency-domain. (b) The corresponding real part of the plasmon induced electric field with $T_2 = 10$ fs in the time-domain.	24
3.5	(a) Rectangular metallic nanoparticle with the distribution of surface charge when excited with linearly polarized electromagnetic field, \mathbf{E}_0 and \mathbf{B}_0 , propagating along \mathbf{k}_z . When the electric field \mathbf{E}_0 is parallel to the x-axis, the LSPR induced electric dipole field \mathbf{E}_{ind} is also oriented along the x-axis. (b) The complementary structure of (a), which is a rectangular nanohole in metal film, with the distribution of the surface charge excited with a complementary electromagnetic field, \mathbf{E}_0^c and \mathbf{B}_0^c . Here, the magnetic field \mathbf{B}_0^c is parallel to the x-axis, and the induced electric dipole field \mathbf{E}_{ind}^c is oriented along the y-axis. A frequency below resonance frequency is assumed.	28
4.1	Layout of the optical setup of the home-built NLO microscope system, consisting of a few-cycle laser source, an interferometric autocorrelator, a dispersion management unit, a beam management unit, a microscope, and a dark-field and transmission microspectroscopy. See text for details about each component. . .	31

4.2	The characterization of the oscillator output pulse. (a) Measured oscillator pulse spectrum exhibiting FWHM = 173 nm, FWTM = 307 nm, and centered at 820 nm. (b) The measured (black dot) and the simulated (red line) SHG IAC traces of the pulse, which is best fit to a duration of 6.4 fs (<i>sech</i> ²) and residual values of GDD = 0 <i>fs</i> ² and TOD = 120 <i>fs</i> ³	32
4.3	Simulated spectral properties of the custom-made dichroic beamsplitter (BS3) for NLO microscopy. (a) The GDD spectrum exhibits low values over the entire pulse spectral bandwidth range from 600 to 1000 nm. (b) The reflectance spectrum simulated under 45° incidence for un-polarized and s-polarized light. Simulations were provided by Dr. G. Tempea from Femtolasers Produktion GmbH.	33
4.4	Schematic illustration of the dark field (DF) illumination (blue) and the collection microscope objective optical pathways (green) in the home built DF condenser and microscope objective, respectively.	35
4.5	Flowchart of control and data acquisition software for the SHG IAC trace measurements.	37
5.1	An SHG image in the x-y plane of a single 125 nm spherical gold nanoparticle with a measured lateral SHG intensity profile of FWHM = (310 ± 10) nm, which indicates the diffraction-limited focusing of the few-cycle pulses with an Olympus UPLSAPO 60× N.A. 1.2W IR microscope objective.	46
5.2	(a) z-profile of the measured TPF intensity when focusing the few-cycle pulses through the glass-dye solution interface (z = 0) with the Olympus UPLSAPO 60× N.A. 1.2W IR microscope objective. (b) Derivative of the profile shown in (a) with a measured FWHM = (1.3 ± 0.1) μm.	46
5.3	(a) Log-log plot of SHG intensity versus the average excitation laser power when 7.3 fs pulses are focused into a thick KDP crystal with an Olympus UPLSAPO 60× N.A. 1.2W IR microscope objective and the best dispersion compensation. The linear fit to the experimental data (squares) has a slope of (1.93 ± 0.08) mV / mW. (b) Corresponding SHG spectrum (black curve) recorded with an average excitation power of 900 μW. Simulated spectra for residual dispersion values of GDD = 0 <i>fs</i> ² and TOD= 170 <i>fs</i> ³ (blue curve) and for GDD = 0 <i>fs</i> ² and TOD= 0 <i>fs</i> ³ (red curve) according to eq. 3.31.	47
5.4	Example of measured (black dots) and simulated (red line) SHG IAC traces of in-focus pulses with a duration of 36.8 fs (<i>sech</i> ²) that result from incomplete dispersion pre-compensation. Best agreement with the experiment is obtained for the simulation that uses the in-focus pulse spectrum and residual values of GDD = 90 <i>fs</i> ² and TOD = 185 <i>fs</i> ³	49

5.5	The experimental (black dots) and simulated (red lines) SHG IAC traces of in-focus pulses with durations of (6.6 ± 0.3) fs ($sech^2$) and (7.3 ± 0.3) fs ($sech^2$) and residual dispersion of $GDD = 0$ fs^2 and $TOD = 110$ fs^3 and of $GDD = 0$ fs^2 and $TOD = 170$ fs^3 for (a) an Olympus UMPLFL 20× N.A. 0.5W objective and (b) an Olympus UPLSAPO 60 × N.A. 1.2W IR objective, respectively.	50
5.6	Experiments for testing the radially varying GD effect of the in-focus few-cycle pulses. (a) Schematic illustration of the microscope objective (Obj) with an additional iris for adjusting the diameter of its back-aperture. (b) Retrieved pulse duration dependence on the aperture diameter for the Zeiss ACHROPLAN 40× N.A. 0.8W (black squares) and the Olympus UPlanSApo 60× N.A. 1.2W IR (blue squares).	52
5.7	Experimental confirmation of the inverse linear dependence of SHG intensity on pulse duration down to 7.1 fs. (a) Measured SHG intensity (blue dots) when focused into a KDP crystal with an Olympus UPLSAPO 60× N.A. 1.2W IR microscope objective and in-focus pulse duration (black empty circles) extracted from SHG IAC traces versus GDD values controlled by the insertion of the thin wedges. (b) Log-log plot of the SHG intensity as a function of pulse duration (black dots). The linear fit (red curve) has a slope of $-(1.05 \pm 0.03)$ fs^{-1}	54
5.8	(a) AFM phase image of self-assembled collagen (type-I) fibrils on a glass coverslip. (b) The topographical height profile across the fibril (along the red line shown in (a)) with a measured FWHM = (320 ± 5) nm and a peak height of (78 ± 1) nm. (c) The phase profile parallel to the long axis of the fibril (along the blue line shown in (a)) reveals the characteristic D-striation of collagen (type-I) with a period length of (67 ± 2) nm.	55
5.9	Forward-detected SHG images of collagen fibrils obtained with excitation pulse durations of (a) 18.2 fs ($sech^2$) and (b) 7.3 fs ($sech^2$) at an average power of 900 μ W and a pixel dwell time of 2.0 ms. (c) SHG intensity profiles along the lines marked by the arrows in (a) (red curve) and (b) (blue curve). The FWHM of the SHG intensity profile across the fibril located at $y = 9.3$ μ m amounts to (320 ± 10) nm. (d) Log-log plot of the measured (∇) and theoretical (red line) SHG intensity as a function of pulse duration.	56

5.10	(a) SHG spectra of a single collagen fibril recorded in both the forward- (blue curve) and epi- (green curve) detection geometries using excitation with a pulse duration of 7.3 fs ($sech^2$) and an average power of 900 μ W at the sample. The in-focus excitation pulse spectrum (black curve) is shown for reference. (b) The corresponding epi-detected (empty circles) and forward-detected (solid circles) SHG IAC traces of a single collagen fibril together with the simulated SHG IAC traces (red curve) by assuming the in-focus pulse spectrum shown in (a) and residual dispersion values of GDD = 0 fs^2 and TOD = 170 fs^3 , which resembles the SHG IAC trace of KDP (see fig. 5.5 (b)). (c) Measured forward-detected SHG IAC trace (black dots) of the same fibril when excited by pulses with a duration of 18.2 fs ($sech^2$) together with a simulated SHG IAC trace by assuming the in-focus pulse spectrum and residual dispersion values of GDD = 55 fs^2 and TOD = 230 fs^3	57
6.1	Schematic layout showing the arrangement of the gold nanodisks (upper row) with diameters of 20, 40, 60, 80, 100, 120, 140, and 160 nm and of nanorectangles (lower row) with $L_y \times L_x$ dimensions of 25 \times 100 , 33 \times 100 , 50 \times 100, 100 \times 100, 100 \times 50, 100 \times 33, and 100 \times 25 nm^2 as manufactured by EBL. The center to center distance between two neighboring nanoparticles is 2.0 μ m. For all these nanoparticles, the height is 25 nm.	63
6.2	SEM image of individual nanosphere 125 particles. The scale bar is 2.00 μ m. The insert image shows a high magnification of nanoparticle 3 with a = 73.5 nm and b = 63.5 nm.	65
6.3	Measured ensemble extinction spectra of aqueous suspensions of nanosphere 50, nanosphere 80, and nanosphere 125.	66
6.4	Measured DF scattering spectra of individual spherical nanoparticles with specified diameters of 50 nm (black curve), 80 nm (green curve), 125 nm (blue curve) immersed in oil with a refractive index of 1.518. The simulated scattering spectrum (red curve) of a spherical nanoparticle with a designed diameter of 50 nm placed in oil based on Mie theory is also shown for reference.	67

6.5	(a)	Measured DF scattering spectrum (green curve) and the corresponding fit to Lorentzian line-shape (purple curve) are shown together with the SHG spectrum of the same single nanosphere 80 nanoparticle (black curve) in oil. The SHG spectrum of the KDP crystal (blue curve) and the in-focus laser spectrum (red curve) are also shown for reference. (b) Normalized polar plots of the DF scattering intensity (red line symbols) and the SHG intensity (black line symbols) for the same individual nanoparticle. (c) Measured SHG IAC trace (black squares) of the same nanoparticle and the simulated SHG IAC traces for the instantaneous response of KDP (blue curve) and for a plasmon resonance enhanced SHG for a nanosphere with $T_2 = 4.2$ fs and $\lambda_{res} = 581$ nm (green curve) using an in-focus pulse with a pulse duration of (7.3 ± 0.3) fs ($sech^2$) and residual dispersion values of $GDD = 0$ fs^2 and $TOD = 170$ fs^3 . The upper envelope (red curve) for the simulated SHG IAC trace of the instantaneous response is shown. The average powers used in the SHG experiments shown in (a), (b), and (c) are 210 μW , 370 μW , and 380 μW , respectively.	69
6.6	(a)	Measured DF scattering spectrum (green curve) and the corresponding fit to Lorentzian line-shape (purple curve) are shown together with the SHG spectrum of the same single nanosphere 125 nanoparticle (black curve) in oil. The SHG spectrum of the KDP crystal (blue curve) and the in-focus laser spectrum (red curve) are also shown for reference. (b) Normalized polar plots of the DF scattering intensity (red symbols) and the SHG intensity for the same nanoparticle. (c) Measured SHG IAC trace (black squares) of the same nanoparticle and the simulated SHG IAC traces (blue curve) for the instantaneous response of KDP (blue curve) and for the plasmon resonance enhanced SHG for a nanoparticle with $T_2 = 2.5$ fs and $\lambda_{res} = 670$ nm (green curve) using an in-focus pulse with a pulse duration of (7.3 ± 0.3) fs ($sech^2$) and residual dispersion values of $GDD = 0$ fs^2 and $TOD = 170$ fs^3 . The upper envelope (red curve) of a simulated SHG IAC trace for an instantaneous response is shown. The average powers used in the SHG experiments shown in (a), (b), and (c) are 210 μW	71
6.7		Measured ensemble extinction spectra of aqueous suspensions of nanorod 600 (40×69 nm^2 , black curve), nanorod 800 (39×155 nm^2 , blue curve), and nanorod 808 (10×40 nm^2 , green curve).	73

- 6.8 DF scattering spectroscopy of a single nanorod with specified dimensions of $39 \times 155 \text{ nm}^2$, which is immersed in refractive index matching oil. (a) DF scattering spectra recorded with an angle α between the linear excitation polarization and the long axis of the nanorod at 80° , 120° , and 160° . (b) Polar plot of the integrated DF scattering intensity of the long-axis plasmon resonance mode as a function of α . The corresponding fit to the $\cos^2(\alpha - \alpha_0)$ dependence is also shown. 74
- 6.9 (a) Measured DF scattering spectrum (green curve) and the corresponding fit to a Lorentzian line shape (purple curve) are shown together with the SHG spectrum of the same single nanorod 800 (black curve) in oil. The SHG spectrum of a KDP crystal (blue curve) and the in-focus laser spectrum (red curve) are also shown for reference. (b) Normalized DF scattering (red symbols) and SHG intensity (black symbols) polar plots for the same nanoparticle together with fits to eq. 3.42 (red curve) and eq. 3.43 (black curve), respectively. (c) Measured SHG IAC trace (black squares) of the same nanoparticle and the simulated SHG IAC traces for the instantaneous response of a KDP crystal (blue curve) and for the plasmon resonance enhanced SHG of a nanoparticle with $T_2 = (9.0 \pm 0.5) \text{ fs}$ and $\lambda_{res} = (880 \pm 10) \text{ nm}$ (black curve) using an in-focus pulse with a duration of $(7.3 \pm 0.3) \text{ fs}$ (sech^2) and residual dispersion values of $\text{GDD} = 0 \text{ fs}^2$ and $\text{TOD} = 170 \text{ fs}^3$. The upper envelopes for the simulated SHG IAC traces of the KDP (red dash curve) and for the nanorod (black dash curve) are shown. The inset shows the log-log plot of SHG intensity (black squares) as a function of average excitation laser power at the sample. The red line shows the best fit to the experimental data with a slope of $(1.9 \pm 0.1) \text{ counts}/(\text{s } \mu\text{W})$. The average powers used in the SHG experiments shown in (a), (b), and (c) are $30 \mu\text{W}$, $25 \mu\text{W}$, and $25 \mu\text{W}$, respectively. 76

6.10	(A) Measured DF scattering spectrum (green curve) and the corresponding fit to a Lorentzian line-shape (purple curve) are shown together with the SHG spectrum of the same single nanorod 808 (black curve) in oil. The SHG spectrum of a KDP crystal (blue curve) and the in-focus laser spectrum (red curve) are also shown for reference. (b) Normalized SHG intensity (black symbols) polar plot for the same nanoparticle together with a fit to eq. 3.43 (red curve). (c) Measured SHG IAC trace (black squares) of the same nanorod and the simulated SHG IAC traces for the instantaneous response of a KDP crystal (blue curve) and for the plasmon resonance enhanced SHG of the nanorod with $T_2 = (13.0 \pm 0.5)$ fs and $\lambda_{res} = (830 \pm 10)$ nm (black curve) using an in-focus pulse with a duration of (7.3 ± 0.3) fs (<i>sech</i> ²) and residual dispersion values of $GDD = 0$ fs ² and $TOD = 170$ fs ³ . The upper envelopes for the simulated SHG IAC traces of KDP (red dashed curve) and of the nanorod (black dashed curve) are shown. The average powers used in the SHG experiments shown in (a), (b), and (c) are $42 \mu\text{W}$, $50 \mu\text{W}$, and $56 \mu\text{W}$, respectively.	78
6.11	(a) Experimental extinction spectra (dashed curves) of ensembles of nanodisks and simulated extinction spectra (black curves) of single nanodisks with diameters of 80 nm, 100 nm, 120 nm, 140 nm, and 160 nm. (b) The corresponding simulated scattering spectra of single nanodisks in oil and the in-focus laser spectrum (black curve) are shown for comparison.	82
6.12	(a) Schematic layout of the nanodisk array consisting of single nanodisks arranged in rows of same diameters and columns with diameters ranging from 20 to 160 nm. The height of the nanodisk is fixed to be 25 nm. (b) SHG image of the nanodisk array which corresponds to (a). (c) The SHG intensity profile along the white line shown in (b). Insert: the normalized polarization-resolved SHG intensity for a single nanodisk with a diameter of 160 nm as a function of the incident angle of the linearly polarized excitation field. The average excitation laser powers used in the SHG experiments shown in (b) and the polar plot in (c) are $40 \mu\text{W}$ and $130 \mu\text{W}$, respectively.	84

6.13	Measured SHG spectra (black curves) (a), (c), (e), (g), (i) and SHG IAC traces (black squares) (b), (d), (f), (h), (j) of single nanodisks with diameters of 80 nm, 100 nm, 120 nm, 140 nm, and 160 nm, respectively. The measured SHG spectrum of a KDP crystal (red curves) is shown for reference. For each nanodisk size, the simulated SHG IAC traces for both the plasmon resonance enhanced SHG with a dephasing time and a resonance wavelength that best fit the experimental data, as indicated in the figures and for the KDP reference using in-focus laser pulses of (7.3 ± 0.3) fs (<i>sech</i> ²) and residual dispersion values of $GDD = 0$ fs ² and $TOD = 170$ fs ³ are also shown. The upper envelopes of both the simulated SHG IAC traces of the nanodisks (black dash curves) and for instantaneous KDP response (red dash curves) are also shown. The average excitation laser powers used for SHG spectra measurements is $35 \mu\text{W}$ and for the SHG IAC trace measurements range from 20 to $40 \mu\text{W}$	85
6.14	SHG intensities retrieved from the integration of SHG spectra (black circles) and from measured SHG IAC traces (red circles) at fixed time delay of ± 40 fs for single nanodisks with diameters of 80 nm, 100 nm, 120 nm, 140 nm, and 160 nm. The error bars represent the standard deviation obtained from 60 independent SHG spectra and from 10 to 20 independent SHG IAC traces.	86
6.15	Dependence of the plasmon resonance frequency (a) and of the dephasing time (b) retrieved from experimental SHG IAC traces (red dots) and from simulated linear scattering spectra (black curves) for the single nanodisk on their nanodisk diameter. The error bars represent the range of values used for those simulated SHG IAC traces, for which the residuals are indistinguishable within our experimental noise levels.	87
6.16	(a) Experimental extinction spectra (solid curves) of ensembles of nanorectangles and simulated extinction spectra for single nanorectangles (black line scatters) with dimensions of $100 \times 100 \text{ nm}^2$, $50 \times 100 \text{ nm}^2$, and $33 \times 100 \text{ nm}^2$ in air. (b) The corresponding simulated scattering spectra of single nanorectangles in oil and the in-focus excitation laser spectrum (black curve) are shown. The linear polarization of the excitation field for both the experimental and the simulated spectra is oriented along the long axis of the nanorectangles.	89

- 6.17 Schematic of the orientation of a single nanorectangle 50×100 (a) and of a nanorectangle 100×50 (e) in the x-y sample plane. SHG images of a row of three identical nanorectangles 50×100 recorded with a linearly polarized excitation field (E) parallel (b) and perpendicular (c) to the x-axis. SHG images of a row of three identical nanorectangles 100×50 recorded with a linearly polarized excitation field parallel (f) and perpendicular (g) to the x-axis. SHG intensity profiles along the red and blue dashed lines shown in the images for a single nanorectangle 50×100 (d) and for a nanorectangle 100×50 (h). The average excitation power used for this SHG experiment is $40 \mu\text{W}$ 90
- 6.18 Normalized SHG intensity polar plots for the single nanorectangle 25×100 (black squares) and for the nanorectangle 100×25 (red squares) together with the respective simulations according to eq. 3.43 (black and red lines). The error bars represent the standard deviation of the fluctuation of the SHG intensity time trace. The excitation average power used for the SHG imaging is $40 \mu\text{W}$. . 91
- 6.19 Normalized SHG spectra for single rectangles (a) 25×100 , 100×25 , (b) 33×100 , 100×33 , (c) 50×100 , 100×50 , and for square (d) 100×100 measured in oil with linearly x-polarized (black curves) and y-polarized (blue curves) excitation fields. The measured SHG spectrum of a KDP crystal (red curves) is shown here for reference. The SHG IAC traces (black dots) of single rectangles (b) 25×100 , (e) 33×100 , and (h) 50×100 , (k) 100×100 measured with an x-polarized excitation field. (c), (f), (i), (l): The SHG IAC traces measurements for the corresponding orthogonally orientated nanorectangles. For each single nanorectangle, the simulated SHG IAC traces for the KDP reference (blue curves) and for the plasmon resonance enhanced SHG with dephasing times and resonance wavelengths that best fit the experimental curves (black curves), using in-focus laser pulses of $(7.3 \pm 0.3) \text{ fs}$ (sech^2) with residual dispersion values of $\text{GDD}=0 \text{ fs}^2$ and $\text{TOD} = 170 \text{ fs}^3$ are shown. The upper envelopes for both simulated SHG IAC traces for the nanorectangles (black dashed curves) and for the instantaneous KDP response (red dashed curves) are also shown. The excitation average laser powers for the SHG spectrum measurements is $35 \mu\text{W}$ and used for the SHG IAC trace measurements range from 20 to $40 \mu\text{W}$. . 92

6.20	Dependence of the plasmon resonance frequency (a) and the dephasing time (b) retrieved from simulations of the linear scattering spectra (black lines) and from the experimental SHG IAC traces of single nanorectangles on their short-axis dimension when $L_x = 100$ nm (red squares) or $L_y = 100$ nm (black circles) are fixed. In all cases, linearly polarized excitation fields parallel to the long axis of the nanorectangles are used. The error bars represent the range of values used for those simulated SHG IAC traces, for which the residuals are indistinguishable within our experimental noise levels.	94
7.1	Schematic layout showing the arrangement of the rectangular nanohole array in the gold film consisting of nanoholes with $L_y \times L_x$ dimensions of 50×50 , 50×100 , 50×150 , 50×200 , 50×250 , 50×300 , 50×350 , 50×400 , 50×450 , and 50×500 nm^2 manufactured by FIB. The nearest edge-to-edge distance between two neighboring nanoholes is $15.0 \mu m$. The thickness of the gold film is designed to be 300 or 350 nm.	100
7.2	SEM image of the rectangular nanohole array made in a gold film (thickness = 300 nm). A high magnification image of one nanohole is shown in the inset with $L_x = 156.2$ nm and $L_y = 53.2$ nm. The nearest edge-to-edge distance between two neighboring nanoholes is $14.96 \mu m$	101
7.3	(a) Simulated transmission spectra of single rectangular nanoholes in air with $L_y \times L_x$ dimensions of 50×100 , 50×150 , 50×200 , 50×250 , and 50×300 nm^2 in the 300-nm (solid curves) and 350-nm (dashed curves) thick gold films. The in-focus laser spectrum (red curve) is also shown for reference. (b) The simulated transmission spectra of nanohole 50×150 in oil (black curve), air (red curve), and of a bare gold film with a thickness of 350 nm (green curve) in oil are shown. The linear excitation polarization of the excitation field in all simulated spectra is along the short-axis of the rectangular nanohole.	102
7.4	(a) Epi-detected SHG image of an array consisting of single rectangular nanoholes in rows of varying L_x from 100 to 400 nm and constant width of $L_y = 50$ nm in air. The gold film thickness is 300 nm. (b) The SHG intensity profile along the blue arrows shown in (a). SHG features marked by the blue star (*) account for SHG-activated imperfection of the film. The linearly polarized excitation field is parallel to the long-axis of the rectangular nanohole. The average excitation laser power used here is $750 \mu W$	104

- 7.5 (a) SHG intensities retrieved from measured SHG intensity time traces when focused on 300-nm thick film (red squares) and on the single rectangular nanoholes (black squares) with $L_y \times L_x$ dimensions of 50×50 , 50×100 , 50×150 , 50×200 , 50×250 , 50×300 , 50×350 , 50×400 , 50×450 , and $50 \times 500 \text{ nm}^2$. The error bars for the film and nanohole measurements represent standard deviations of fluctuations of SHG intensity time traces and average SHG intensities of two different individual nanoholes, respectively. The average powers used here are $260 \mu\text{W}$. (b) The log-log plot of SHG intensity of the single nanohole 50×200 (blue squares) and of the film (black squares) as a function of the average excitation laser power. The theoretical curves with a slope of two (solid curves) are shown for references. 106
- 7.6 (a) Schematic layout showing the arrangement of a single rectangular nanohole in the x-y sample plane and defining the angle α between the linearly polarized excitation field (double arrow) and the x-axis. (b) Experimental SHG intensity polar plot (black squares) recorded on the bare film. (c) Difference SHG intensity polar plot (black squares) together with a fit to eq. 3.43 (red line), obtained by subtracting the SHG intensity recorded on the individual rectangular nanohole 50×200 with the SHG background of the film shown in (b). The average excitation laser power in these SHG experiments is $750 \mu\text{W}$ 107
- 7.7 (a) The epi-detected SHG spectra measured for a single rectangular nanohole 50×250 (black curve) and for the 300-nm thick gold film (blue curve). (b) Normalized SHG spectra of single rectangular nanoholes with different dimensions and of the film. The linear polarization of the excitation field is parallel to the long-axis of the rectangular nanohole. The average excitation laser power is $520 \mu\text{W}$ 107
- 7.8 Measured SHG IAC traces (a), (b), (c), (d), (e), (f), (g), (h), and (i) of single rectangular nanoholes (black squares) with $L_y \times L_x$ dimensions of 50×50 , 50×100 , 50×150 , 50×200 , 50×250 , 50×350 , 50×400 , 50×450 , and $50 \times 500 \text{ nm}^2$, respectively, together with the measured SHG IAC trace of 300-nm thick gold film (blue curves). The experimental SHG IAC trace of the KDP crystal (black squares) measured under the identical experimental conditions and of the simulated SHG IAC trace (red curve) with shortest in-focus excitation laser pulses of $(7.3 \pm 0.3) \text{ fs}$ (sech^2) and residual dispersion values of $\text{GDD} = 0 \text{ fs}^2$ and $\text{TOD} = 170 \text{ fs}^3$ are also shown in (j). The average excitation laser power in all experiments is $260 \mu\text{W}$, and the excitation polarization field is linearly polarized parallel to the long-axis of the rectangular nanoholes. 108

7.9	Comparison between the experimental SHG IAC trace recorded on the bare 300-nm thick gold film (black curve) and the simulated SHG IAC traces of single rectangular nanoholes with dimensions 50×100 , 50×150 , 50×200 , 50×250 , and $50 \times 300 \text{ nm}^2$ when assuming the plasmon resonance parameters as listed in table 7.2 and our shortest in-focus excitation laser pulses of (7.3 ± 0.3) fs (<i>sech</i> ²) with residual dispersion values of $\text{GDD} = 0 \text{ fs}^2$ and $\text{TOD} = 170 \text{ fs}^3$.	110
7.10	Forward-detected SHG images of an individual rectangular nanohole with $L_y \times L_x$ dimensions of $50 \times 300 \text{ nm}^2$ in a 350-nm thick gold film oriented in the x-y sample plane according to fig. 7.11 (c) and recorded with linearly polarized excitation perpendicular (a) and parallel (b) to the x-axis. (c), (d) SHG intensity profiles along the white dashed lines shown in the images (a) and (b), respectively. The average excitation laser power is $1500 \mu\text{W}$.	112
7.11	(a) The log-log plot of forward-detected SHG intensity of a single nanohole 50×200 in a 350-nm thick gold film as a function of average excitation powers (black squares). The theoretically expected quadratic power dependence with slope of two (red curve) is shown for reference. (b) SHG polar plot of the individual nanohole 50×200 detected in the forward direction together with a fit to eq. 3.43 (red curve). The average excitation laser power is $580 \mu\text{W}$. (c) Schematic layout showing the arrangement of a single rectangular nanohole in the x-y sample plane and defining the angle α between the linearly polarized excitation field (double arrow) and the x-axis.	113
7.12	(a) The measured SHG IAC traces of the single rectangular nanohole 50×200 (black squares) in 350-nm thick gold film in oil and of the KDP reference (red curve) together with simulated SHG for a plasmon resonance enhanced SHG with parameters $T_2 = (5.1 \pm 0.5) \text{ fs}$ and $\lambda_{res} = (808 \pm 10) \text{ nm}$ using our in-focus laser pulses of 7.3 fs (<i>sech</i> ²) with residual dispersion $\text{GDD} = 0 \text{ fs}^2$ and $\text{TOD} = 170 \text{ fs}^3$ (blue curve). (b) The corresponding SHG IAC traces measured for a single nanohole 50×350 (black squares) and for the KDP reference (red curve) together with the corresponding SHG IAC simulation for plasmon resonance enhanced SHG with parameters $T_2 = (5.0 \pm 0.5) \text{ fs}$ and $\lambda_{res} = (1242 \pm 10) \text{ nm}$ (blue curve). The average excitation laser power in all experiments is $1200 \mu\text{W}$ and the excitation field is linearly polarized parallel to the short-axis of the rectangular nanohole.	114

12 List of tables

5.1	The NLO microscope configurations for the detection geometry, filters, and detectors used for the different experiments discussed in this chapter.	44
5.2	Retrieved in-focus pulse durations with pre-compensated GDD and TOD values for a series of microscope objectives with increasing N.A.	50
6.1	The DF scattering and NLO microscope configurations for the detection geometry, filters, and detectors used for the different experiments discussed in this chapter.	62
6.2	Statistical analysis for the five individual nanosphere 125 nanoparticles shown in fig. 6.2.	65
6.3	The ensemble characteristics of aqueous nanosphere suspensions used in this work.	66
6.4	The ensemble characteristics of aqueous nanorod suspensions used in this work.	73
6.5	Summary of the plasmon information retrieved from single gold nanoparticles using linear DF scattering and SHG spectroscopies and from ensemble extinction spectroscopy of nanoparticles suspensions.	80
6.6	The plasmon resonance parameters for nanodisks of different diameters extracted from experimental ensemble extinction spectra and from simulated extinction spectra for single nanodisks in air.	83
6.7	Summary of the plasmon resonance parameters retrieved from full MNPBEM simulations of linear scattering spectra and from the measured SHG IAC traces for the single nanodisks in oil. The center wavelengths retrieved from corresponding SHG spectra are also shown.	87
6.8	The plasmon resonance parameters extracted from the experimental extinction spectra of ensembles of nanorectangles and from the simulated extinction spectra of single nanorectangles of different aspect ratios in air.	89

6.9	Summary of the plasmon resonance parameters retrieved from full MNPBEM simulations of the linear scattering spectra and from the SHG IAC traces measured for the investigated single nanorectangles of a varying aspect ratio and of orthogonal orientations in oil. The center wavelengths extracted from the corresponding SHG spectra are also listed.	93
7.1	The NLO microscope configurations for the detection geometry, filters, and detectors used for different experiments discussed in this chapter.	99
7.2	The plasmon resonance parameters extracted from simulated transmission spectra of individual rectangular nanoholes ($L_y = 50$ nm, $L_x = 100$ – 350 nm) in the gold film with thicknesses of 300 nm and 350 nm in air, respectively.	103
A.1	The values of total optical path lengths in the different media and the number of reflection bounces on the DMCs to achieve minimum in-focus pulse durations for a series of microscope objectives with our setup.	142
A.2	Dispersion values for each reflection on the different optical components and materials in the optical paths of our setup (see section 3.2 for reference).	143

Appendices

A.1 Estimation of material dispersion for common microscope objectives

For the estimation of the total values of compensated GDD, TOD, and in-focus pulse duration obtained under conditions of best dispersion compensation for common microscope objectives listed in table 5.2 in chapter 5, the specified GDD and TOD values for the number of reflection bounces on the DMCs, the reflection on the steering mirrors, the dichroic beamsplitter, and the optical path lengths in air, fused silica glass wedge, immersion water (the working distance of the microscope objectives), and the BK7 glass coverslip, as summarized in table A.1, have been taken into account.

Table A.1: The values of total optical path lengths in the different media and the number of reflection bounces on the DMCs to achieve minimum in-focus pulse durations for a series of microscope objectives with our setup.

Microscope Objective	Working distance / mm	Total optical path in air / mm	Total optical path in wedge / mm	Number of bounces on DMCs
Olympus UMPlanFL N 20X NA 0.5W	3.5	2020 \pm 4	1.50 \pm 0.04	40
Zeiss ACHROPLAN 40X NA 0.8W	3.6	2020 \pm 4	1.50 \pm 0.04	40
Olympus LUMPlanFI 60X NA 0.9 W IR	2.0	2138 \pm 4	3.00 \pm 0.04	50
Olympus UPlanSApo 60X NA 1.2W IR	0.28	2117 \pm 4	0	48

In order to estimate the compensated GDD and TOD values for each objective listed in table 5.2 in chapter 5, we added up the dispersion introduced by each optical component in our setup, using the material constants, path length parameters, and numbers of reflection bounces on the

DMCs, as listed in tables A.2 and A.1. The accumulated uncertainties for GDD values listed in table 5.2 for each objective were estimated using error propagation.

Table A.2: Dispersion values for each reflection on the different optical components and materials in the optical paths of our setup (see section 3.2 for reference).

Material / optical component	GDD / fs ² @ 800 nm	TOD / fs ³ @ 800 nm
air per 1 mm	$(20.05 \pm 0.06) \cdot 10^{-3}$	$(11.8 \pm 0.4) \cdot 10^{-3}$
water per 1 mm	24.8 ± 0.5	27.0 ± 3.0
BK7 glass per 1 mm	43.96	31.90
fused silica glass per 1 mm	40.00	28.43
single reflection on a beam steering mirror	0 ± 5	—
single reflection on the dichroic beamsplitter (BS3)	0 ± 25	—
single reflection on the DMC	-45 ± 10	-25

Curriculum vitae

Personal information

- Full Name: Hui Wan
- Date of Birth: 19/03/1985 in Nanchang, Jiangxi
- Nationality: Chinese

Education

- Ph.D. student at University Stuttgart, 3rd Institute of Physics (since 07/2011)
- M.Sc. degree in Physics Electronics, Institute of Optoelectronics, Shenzhen University, China (9/2008 - 06/2011)
- B.A degree in Physics, Jiangxi Science and Technology, Normal University, China (9/2004 - 7/2008)